Phase Space Characterization of an Internal Ion Source For Cyclotrons

By

Edward Russell Forringer

A DISSERTATION

Submitted to
Michigan State University
in partial fulfillment of the requirements
for the Degree of

DOCTOR OF PHILOSOPHY

Department of Physics and Astronomy

2004

ABSTRACT

Phase Space Characterization of an Internal Ion Source For Cyclotrons

By

Edward Russell Forringer

Orbit tracking codes are used to predict the behavior of the beam in a cyclotron before the cyclotron is constructed by tracking many orbits which collectively are intended to represent the beam. Cyclotrons with internal ion sources (such as the series of 250 MeV proton beam cancer therapy cyclotrons being manufactured by ACCEL Instruments GmbH of Bergisch-Gladbach Germany) present difficulty for these orbit tracking calculations in that there are several parameters which can be adjusted in the calculation that have a large effect on the phase space characteristics of the calculated beam (both the emittance of the beam and the shape of the beam in phase space). The primary goals of the research presented in this dissertation then are to experimentally measure the axial and radial emittance and luminosity of the beam produced by a cold cathode PIG (Penning Ion Gage) internal ion source under dc extraction and to develop a "recipe" for initial conditions of calculated orbits starting from the ion source that match the experimentally measured beam.

The experimental results presented in this dissertation, to the best of our knowledge, represent the first published emittance and luminosity measurement of a cold cathode PIG internal ion source. By taking measurements in several different configurations, it was determined that the shape and size of the source aperture has a large effect on the characteristics of the extracted beam. We were also able to observe that increasing the plasma arc current in the ion source produces higher current and luminosity in the extracted beam. The maximum luminosity measured using a chimney

with a 5.0 mm (0.196") tall, 0.25 mm (0.010") wide slit, was 7.1 $\frac{A}{cm^2-sr}$. Two other chimneys with larger apertures were measured at lower arc currents being limited by the power handling capabilities of the Ion Source Test Stand.

The concepts of 'plasma boundary' (section 2.7.2) and 'plasma temperature' are developed as a useful set of parameters for describing the initial conditions used in orbit tracking. We observe that an approximately flat plasma boundary provides the best match to the experimental beams emerging from the 'slit' style chimneys in our study, while a concave plasma boundary (curving toward the source axis) provides a better match for the beam that emerges from the 'hole' style chimney. In all cases, the plasma temperature that provides the best match for experimental beams is approximately 35,000 K (resulting in a central starting energy of 4.5 eV).

Using the methods presented in this dissertation, the orbit tracking code Z3CYCLONE is able to predict the beam produced by a cold cathode PIG ion source with adequate accuracy such that construction of actual cyclotrons can proceed with reasonably prudent confidence that the cyclotron will perform as predicted.

ACKNOWLEDGEMENTS

First, to Dr. Henry Blosser, for suggesting a research topic, for spending many hours working on this project, for patiently waiting for me to finish, and for reading and suggesting changes to many revisions of this dissertation, I owe a humble "thank you." Thanks also goes to my guidance committee members Drs. Richard York, Felix Marti, Terry Grimm, Wayne Repko, and Julius Kovacs. Thanks to the staff at Harper Hospital (particularly Emanuel Blosser), and ACCEL Instruments who have shared their expertice and equipment during the construction of the Ion Source Test Stand and subsequent data collection. My deepest appreciation goes to the incredible NSCL staff including Jim Wagner, Phil Fighter and all the machine shop staff (particularly Jay Pline for work working with us during the holidays) for getting my parts made on time so many times, Guenter Stork and Jim Moskalik for designing many of those parts, Dave Sanderson and Andy Thulin for helping resolve vacuum issues, Bob Welton for his expert welding, Mark Davis and Kelly Davidson for help with data collection, and Barbara Pollack and the computer help-room staff for meeting all of my computer related needs. Thanks to the authors and maintainers of the Z3CYCLONE and associated codes (Dr. Morton Gordon, Dave Johnson, Dr. Marti, Dr. Steve Snyder, Dr. Dmitry Gorelov and many others over the years). I owe a debt to Malay Dey, who worked on the NSCL Ion Source Test Stand for a year while I was away teaching, and while none of the data he collected ended up in this dissertation, his help during that time is immeasurable. I need to thank my immediate family (Stephanie, Josiah and Amara) for understanding and patience during this process, my bosses and colleagues at LeTourneau University, and my parents and extended family for their support and encouragement.

CONTENTS

LIST OF TABLES

LIST OF FIGURES

Chapter 1

Introduction

An important overall figure of merit for the ion source of a cyclotron is the phase space density of the beam it produces. A cyclotron has a restricted phase space acceptance for acceleration and extraction of an ion beam. Improvements in the phase space density of the beam leaving the source are directly reflected in improved phase space density of the extracted beam and higher total extracted beam current. This dissertation describes measurements of the phase space density of the beam extracted from a particular cold cathode ion source used in several cyclotrons. The experimental measurements are also compared to predictions based on computational ray tracking.

1.1 Cyclotron Ion Sources

The National Superconducting Cyclotron Laboratory (NSCL) has, as a natural part of its on going research and development of advanced cyclotrons, developed and refined ion sources for use in its cyclotrons. Modern cyclotrons use several different types of ion sources. Examples of external ion sources are Electron Cyclotron Resonance (ECR) ion sources and multicusp ion sources; examples of internal ion sources are

cold cathode sources and hot filament sources.

ECR ion sources are typically used to produce high charge state heavy ions. ECR ion sources are external to the cyclotron, and the low energy ion beam must be transported and injected into the center of the cyclotron. The NSCL continues to develop ECR sources for its K500 $\otimes$ K1200 coupled cyclotrons [1] [2].

External multicusp ion sources have been used to produce H^- ions for the CYCLONE 30 series of cyclotrons developed by Ion Beam Applications Gmbh of Louvain-la-nueve, Belgum to produce a beam of negative ions. (Acceleration of negative hydrogen ions in these cyclotrons is advantageous in that extraction is straight forword by means of stripping of the H^- ions in a thin carbon foil, leading to extraction efficiencies close to 100% [3].)

Internal ion sources have the advantage of producing the ion at the center of the cyclotron, thus requiring no low energy beam transport. The class of internal ion sources studied in this dissertation uses a Penning Ion Gauge (PIG) Discharge [4] to produce the ion beam. These sources have the basic geometry shown in figure 1.1. Electrons from the cathode are accelerated by the potential difference between the cathodes and the hollow anode. The axial magnetic field constrains electrons to move along the magnetic field lines preventing them from readily moving to the anode. The electrons are then reflected by the opposite cathode and can make many oscillations through the source raising the probability that they will ionize whatever gas is present in the ion source. This discharge then produces a plasma from which positive ions can be extracted by a "puller" electrode through an opening in the anode. The complicated nature of this discharge is well expressed by Bennett [4]:

> "Although a considerable amount of work has been carried out on Penning discharges the theory is inadequate. In fact relatively little is known of the mechanism occurring in the ion sources which we will discuss.

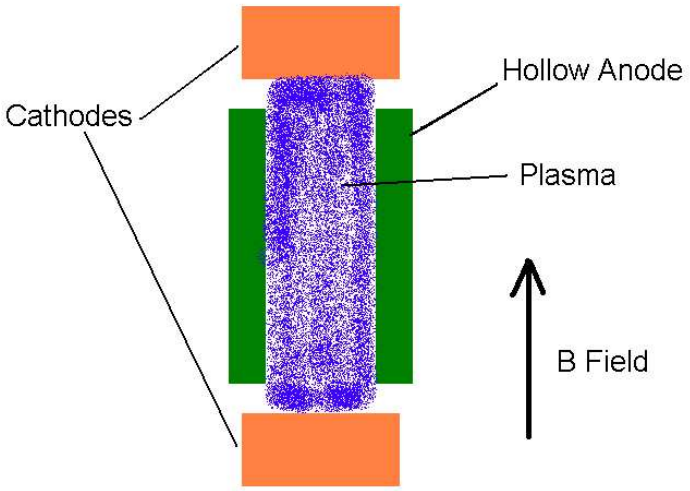

Figure 1.1: Geometry of a Penning Discharge as Used in Internal Ion Sources. (Images in this dissertation are presented in color.)

> The characteristics of the arc can vary widely and depend critically on the geometry and conditions of operation. Such is the complexity of the many processes occurring that reproduction of the same conditions even in the same equipment can sometimes be difficult."

Internal ion sources have evolved over time. In 1953 Livingston and Jones (LJ) [5] reported on their experience with a filament source used for high intensity protons (figure 1.2). Their cathode was a U-shaped tantalum filament, heated with about 400 amps of electric current. The arc current (the total current measured between the anode and cathode of the ion source) was between 2 and 6 amps. As seen in figure 1.2 a 0.2 in^2 (129 mm^2) area vertical slit provided the path for ions to exit the source. With this source Livingston and Jones were able to extract 150 mA using a puller voltage of 12kV and a source-puller gap of about 0.13" (3.3 mm). [5]

In 1966, Mallory presented the first phase space density studies on an internal ion source for cyclotrons [6]. The source he used in his studies was also a filament ion source for proton production. However, Mallory's source slit was 0.023 in^2 (15 mm^2)

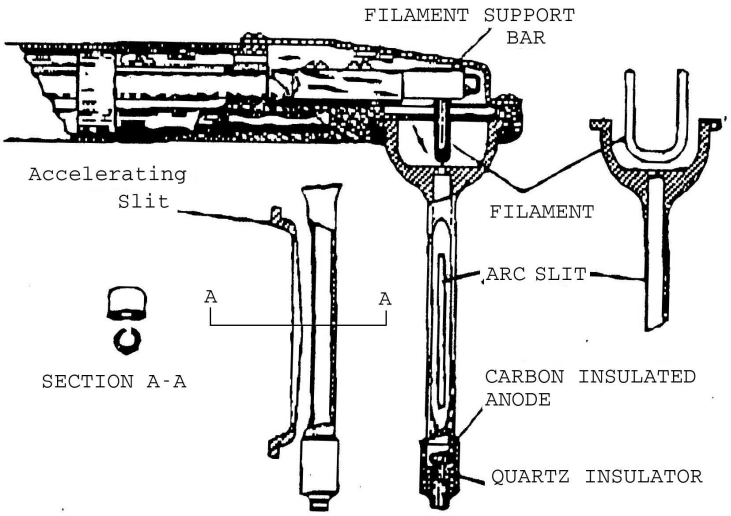

Figure 1.2: High Intensity Proton Ion Source (Fig. 2 from Livingston and Jones [5])

i.e. about a factor of 10 smaller than the slit in the LJ source. Using an extraction voltage of 30kV on the puller and with a source to puller gap varying between 0.2" (5 mm) and 0.4" (10 mm) for various data sets, Mallory's source produced proton beams in the 10 mA range.

In 1983 a team from the NSCL reported on their success in using a Penning Ion Gauge (PIG) ion source in the newly completed K500 superconducting cyclotron (figure 1.3) [7]. This source was quite different from the LJ and Mallory sources in that it used a cold cathode discharge. This K500 source was mainly intended to produce beams of heavy ions such as Nitrogen, Oxygen, and Argon among others with protons of only incidental interest. The K500 source, however, employed the same basic Penning discharge geometry as the LJ and Mallory sources.

More recently, versions of the K500 PIG ion source have been developed for the K100 neutron beam therapy cyclotron at Harper Hospital in Detroit Michigan [8] (hereafter referred to as the "Harper Medical Cyclotron") and for use in a series of 250 MeV cancer therapy cyclotrons being manufactured by ACCEL Instruments GmbH

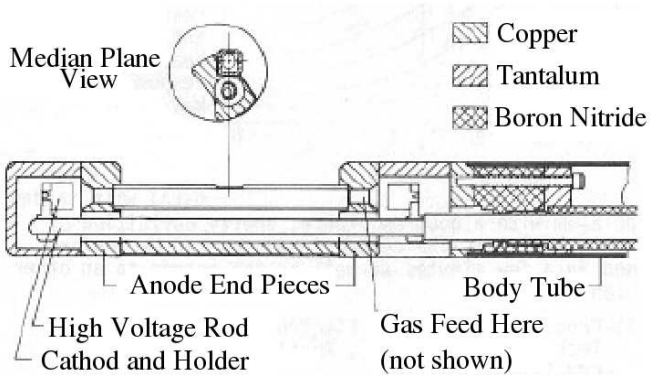

Figure 1.3: K500 Ion Source (Fig. 1 from Antaya [7])

of Bergisch-Gladbach Germany. The first of the ACCEL cyclotrons [9] is now (July 2004) being installed at the Paul Scherrer Institute (PSI) in Villigen, Switzerland (the PSI PROSCAN project [10]) and two more cyclotrons of this type are under contract.

The ion source used in the 250 MeV ACCEL cyclotrons is modeled very closely after the source used in the Harper Medical Cyclotron except for the detail of being optimized for protons rather than deuterons. A primary objective of this dissertation is to make reliable measurements of the phase space density of the beam produced by this type of ion source.

1.2 Ion Source Figures of Merit: Phase Space, Emittance and Luminosity

For readers not familiar with the characteristics of phase space density measurements, three beams of ions are shown in figure 1.4. The first beam (a) has all the ions moving in the same direction, but they are spread out. The second beam (b) has all the ions tightly bunched together, but they are moving in different directions. The last beam (c) has all the ions moving in the same direction and tightly bunched together. The

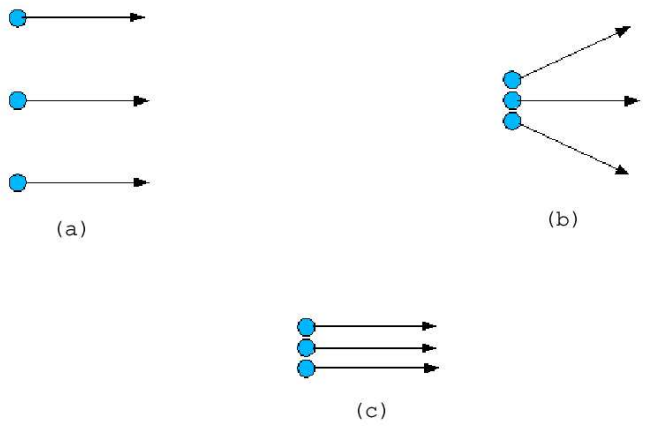

Figure 1.4: Ion Beams With Zero Phase Space Area.

last beam is preferred because it is tightly packed and, in the absence of any forces, will stay that way. However, in some aspects these beams are all equally good. This is because the first two beams (a and b) can be focused using magnetic or electrostatic lenses into a tightly packed beam. Figure 1.5 shows a set of lenses for the first two beams that will transform each into a tightly packed parallel beam.

There are some beams which cannot be focused into a tightly packed beam by using lenses. Figure 1.6 shows such a beam. Any lens that will focus the three rays that start out at the center will not focus the two rays that start out above and below. Any lens that focuses the three rays that start out parallel will not focus the two rays that start at an angle.

To understand the difference between beams that can be perfectly focused and beams that cannot, it is helpful to graph the beam in canonical coordinates ("phase space" [12, p335]) as in Fig 1.7. The horizontal axis gives the vertical displacements of a particular ray at the location where the plot is made, and the vertical axis is the z component of the particles momentum (p_z). Figure 1.7 then shows the phase space diagram of three previously discussed beams. The two beams (a and b) make a line in phase space, meaning both have a zero phase space area. In contrast, beam

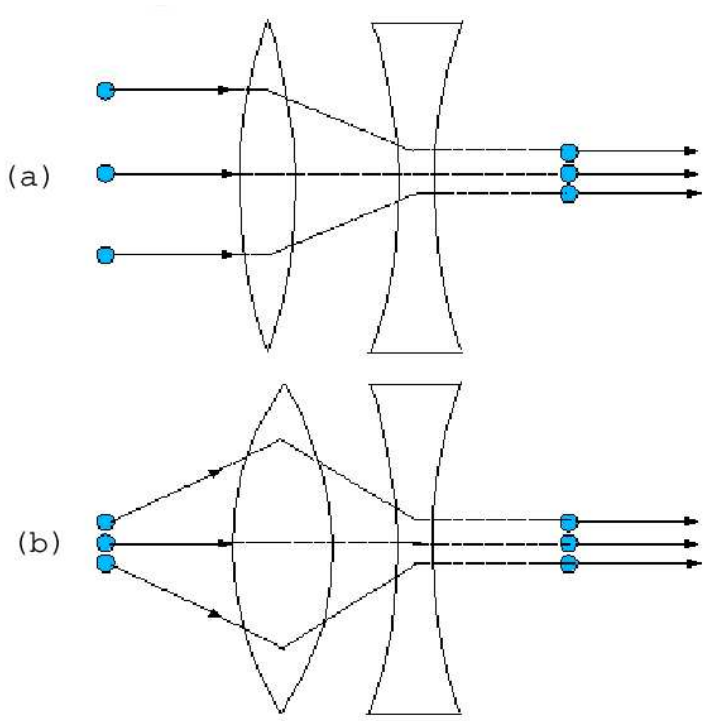

Figure 1.5: This figure shows how two beams which appear less than ideal can be focused by electric or magnetic elements (here represented as "thin lenses") into an ideal beam.

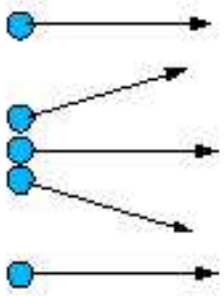

Figure 1.6: This beam, unlike the beams shown in figure 1.4 cannot be focused into an ideal beam by any set of focusing elements.

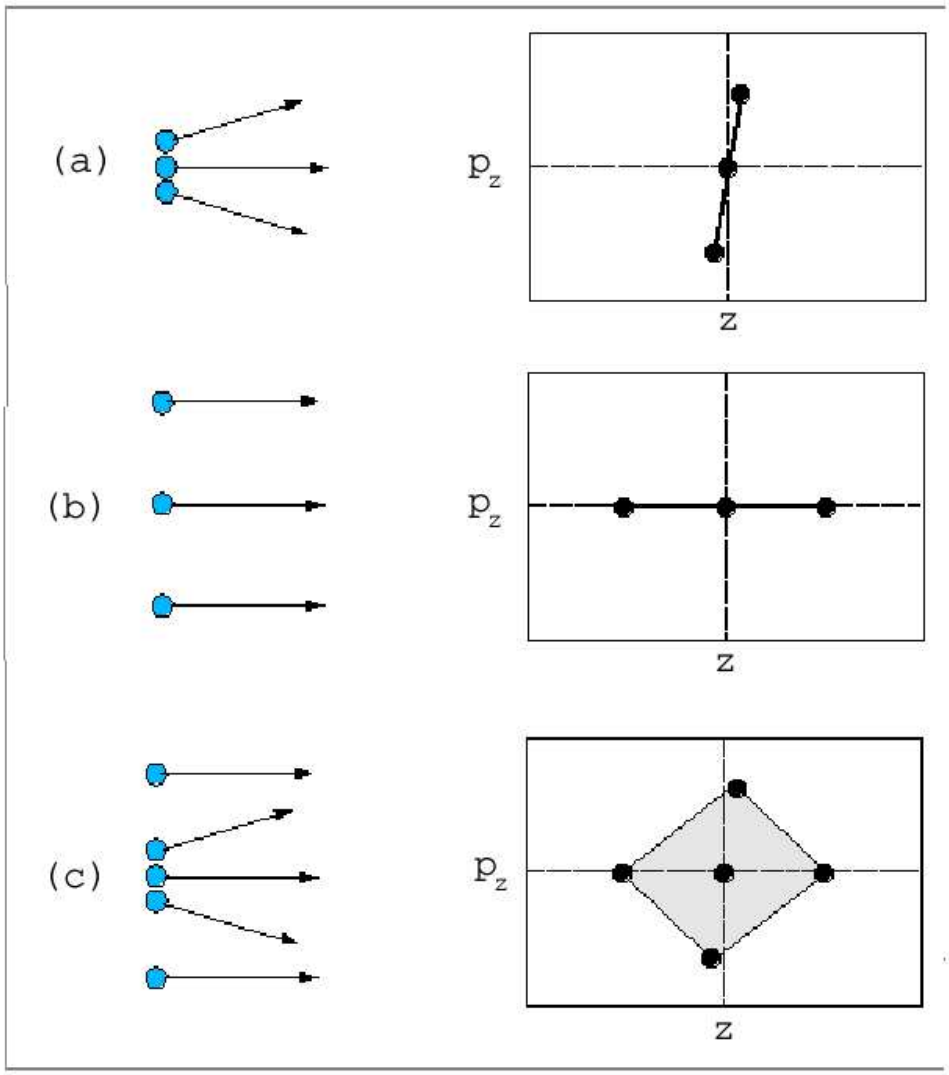

Figure 1.7: Phase space plot of three "beams" of ions. The top two beams have a zero phase space area. The third beam has a non-zero phase space area. Phase space area, is a common measure of the quality of an ion beam.

(c) makes a diamond with a non-zero phase space area. Liouville's Theorem [12, pp 419-421] requires the density of trajectories in a phase space volume to be constant so the (a) and (b) distributions in Fig. 1.7 will have zero current and distributions of type (c) are the ones of practical intrest.

The total volume that a beam covers in phase space (phase space volume), or more importantly, the phase space density (beam current divided by phase space volume) is a measure of the quality of a beam. (The basic character of orbits in a cyclotron leads to cylindrical coordinates to describe the trajectories with the axial (z, p_z) phase space describing the vertical area of the beam and the radial $(r,\ p_r)$ phase space describing the horizontal area of the beam.)

An alternative convenient measure of the compactness of a beam is its "emittance area" where emittance is defined as the product of beam width (usually expressed in mm) and beam divergence (usually expressed in milliradians). An axial emittance plot will then usually have z on the horizontal axis and α_z on the vertical axis. For a beam of particles where p_z for each ion is small compared with its total momentum p, the angle α_z is approximately proportional to the axial momentum i.e:

$$\alpha_z = \tan^{-1}(\frac{p_z}{p}) \approx \frac{p_z}{p}. \tag{1.1}$$

Likewise, a radial emittance plot will have r on the horizontal axis and α_r on the vertical axis where:

$$\alpha_r = \tan^{-1}(\frac{p_r}{p}) \approx \frac{p_r}{p}. \tag{1.2}$$

The emittance (ϵ) of a beam(usually expressed as mm-mrad) is the area that the beam occupies in an emittance plot.

In most situations beams will have vaguely defined edges due to fluctuations in parameters, non-linear effects, etc. so that the area required to contain 100% of the beam may be several times larger than the area required to contain 80% or 90% of

the beam. To avoid this confusion, emittance is usually reported as the area that contains 90% of the beam and this convention is adopted in the present study.

While phase space volume is invariant per Liouville's Theorem, emittance decreases when acceleration occurs, (since the vertical axis of the emittance plot has been scaled by the momentum of the particle.) Per Gruber [20] emittance can be normalized by multiplying by the relativistic factors $\beta\gamma$. In this dissertation ϵ will represent the experimentally measured 90% emittance whereas ϵ_N will give the normalized value of the experimental 90% emittance i.e.:

$$\epsilon_N = \beta\gamma\epsilon \tag{1.3}$$

Normalized emittance like phase space volume, is invariant with respect to acceleration of the beam.

The best beams will have small axial and radial emittance and a large number of particles (measured by the electrical current of the beam, I). This leads to luminosity (L) as a figure of merit for an ion beam:

$$L \equiv \frac{I}{\epsilon_r \epsilon_z} \tag{1.4}$$

For an accelerator with a fixed emittance aperture, the luminosity of the ion source determines the maximum extracted beam current. For this reason, luminosity is normally the most important figure of merit for an ion source intended for high intensity cyclotrons. In order to calculate luminosity both radial and axial emittance data for the same beam are needed. The NSCL ion source test stand however, can only measure one of these at a time, so that two runs with the same ion source parameters are required to determine the luminosity. (An apparatus to simultaneously measure both radial and axial emittance would be much more complicated and costly.)

1.3 Measuring Emittance.

The standard method for measuring the emittance of a beam is to use a movable slit and wire combination. This is the method used in the Mallory dissertation [6] and the same method is used in the collection of data for this dissertation.

The ion source test stand has a nearly uniform magnetic field pointing in the z direction (deviations from a flat field are discussed in section 2.2.2). Such a field causes each ion to travel in a circle in the horizontal plane (r, θ) and provides little focusing in the z direction i.e. the particles will move in a helical path.

Figure 1.8 shows the setup used for measuring z emittance. A movable horizontal slit is placed in the beam path. Since the slit aperture is small (0.010" or 0.25 mm) with respect to the size of the beam, it blocks the majority of the ions. The slit serves as a position selector. All of the particles coming through the slit have started at the vertical position determined by the slit position (z), but they are moving in different directions (α_z) and will diverge from each other.

The wire is placed downstream from the slit. It is scanned across the beam and measures the current of the beam at each location. The position of the wire indicates the angle (α_z) at which the ions were moving when they went through the slit. To obtain a complete data set, the slit position is varied and for each slit position the wire makes one complete scan. By measuring the current hitting the wire at each combination of slit and wire positions, we then determine the intensity of the beam at every point on an emittance plot.

Figure 1.9 shows the setup used for measuring r emittance. Due to the general radial focusing property of a nearly flat magnetic field, ions passing through the thin slit converge 180 degrees downstream from the slit. If the wire probe was placed at this position, it would not be useful in determining the angle the beam had when it passed through the slit. In contrast, 90 degrees downstream from the slit, the position

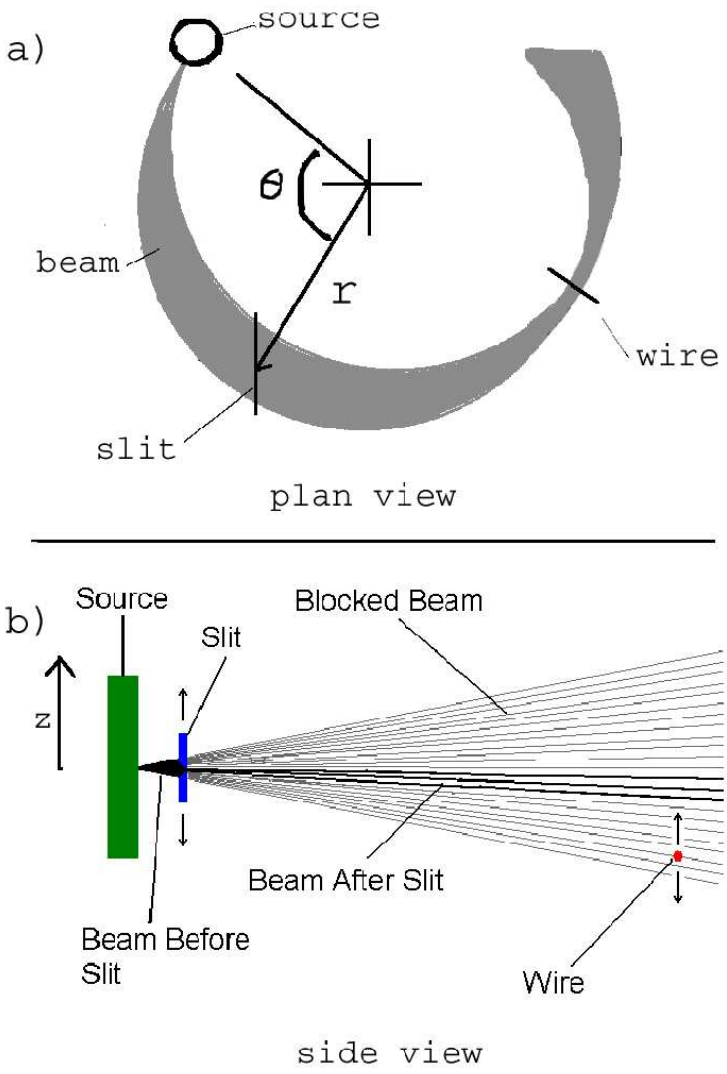

Figure 1.8: Simplified schematic of slit and wire probes for measuring axial emittance. The plan view (a) shows the relative location of the source, slit and wire. The side view (b) shows the motion of the slit and wire with respect to the beam. The diagram does not show the effect of the electric field between the source and the puller on the beam.

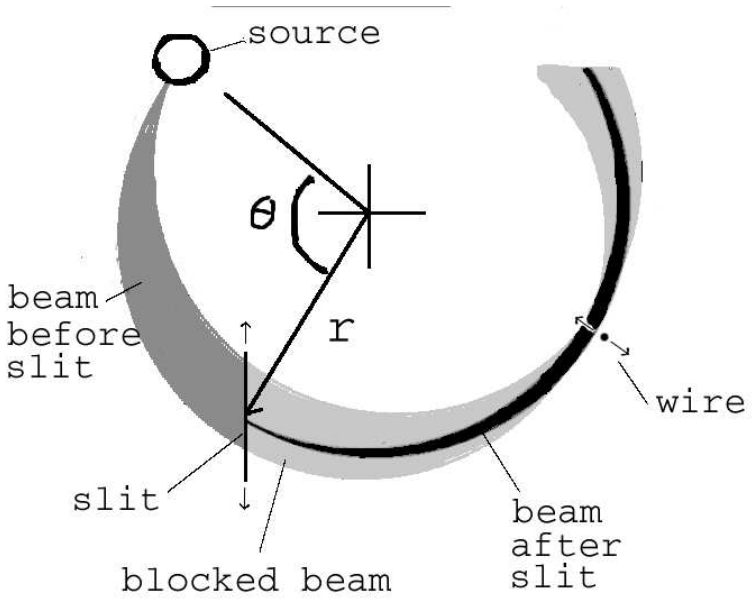

Figure 1.9: Simplified schematic of slit and wire probes for measuring radial emittance. Shown are the relative location of the source, slit and wire. (The diagram does not include focusing effects of the electric field between the source and the puller.)

of the ions is determined by the angle (α_r) each had as it passed through the slit. By placing the wire probe 90 degrees downstream from the slit probe, the radial position of the beam as it crosses the wire probe is correlated with the angle it had when it passed through the slit thus determining the divergence (spread in angles α_r).

1.4 Orbit Tracking

A cyclotron uses electric and magnetic fields to accelerate and direct an ion beam. The force on a charged particle moving in an electric and magnetic field is given by the Lorentz force:

$$\vec{F} = q(\vec{E} + \vec{v} \times \vec{B}) \tag{1.5}$$

If the electric and magnetic fields in the cyclotron are known, the force on a

particle and therefore the acceleration ($\vec{a} = \frac{\vec{F}}{m}$ for non-relativistic speeds) on that particle can be calculated. For example, if constant acceleration over a small time interval Δt is assumed:

$$\vec{v}(t + \Delta t) = \vec{v}(t) + \vec{a}(t)\Delta t \tag{1.6}$$

$$\vec{r}(t + \Delta t) = \vec{r}(t) + \vec{v}(t)\Delta t + \frac{1}{2}\vec{a}(t)(\Delta t)^2 \tag{1.7}$$

At any point in time, if the position and velocity of the ion and the electric and magnetic field acting on the ion are known, its position and velocity a short time later can be calculated. This process can be iterated many times to track particle trajectories from the ion source all the way to extraction. The orbit tracking codes used at the NSCL use fully relativistic equations of motion and a fourth-order Runge-Kutta numerical integration method rather than the simple constant acceleration approximation shown above (equations 1.6 and 1.7). (The numerical errors in fourth order Runge-Kutta calculations are of the order $(\Delta t)^5$ compaired to $(\Delta t)^2$ for constant acceleration.)

Orbit tracking is an important part of the process of designing cyclotrons. With an internal ion source, it is clear that all the ions that are being accelerated start in the slit of the ion source. What is not clear is the starting energy the ions have in the plasma and what direction the ions will move when they leave the source.

As Schubert points out in his doctoral dissertation [11], the direction with which the ions leave the ion source is strongly dependent on the details of the electric field near the ion source slit. The shape of the zero volt contour that crosses the slit (usually called the plasma boundary) is not known a priori and must be determined experimentally. Also the initial energy of the ions as they leave the source is not known.

Schubert attempted to determine these initial conditions by comparing computa-

tional orbit tracking to orbit paths observed experimentally in the Harper Medical Cyclotron. (He did these calculations and measurements with a radio frequency (rf) extraction voltage pulling the ions out of the ion source as happens in a real cyclotron versus the dc extraction voltage used in the present study.) Schubert found combinations of starting energy, starting rf phase, and plasma boundary shape which allowed his computed orbits to approximately match "foil burns" taken on the first four orbits in the Harper cyclotron. These solutions were however not unique i.e., it was possible to compensate for a change in the plasma boundary shape, by choosing different starting energies or starting rf phase (Schubert dissertation p37).

By using dc extraction in the ion source test stand, starting time is removed as a relevant variable. By comparing computed orbits to the measurements of the dc behavior, it is then possible to determine a shape of the plasma boundary and starting energy which matches the experimentally observed trajectories of the ions leaving the source.

1.5 Overview of Following Chapters

Chapter 2 describes the construction and operation of the ion source test stand that was built for the research described in this dissertation. The magnet, the vacuum system, the high voltage system, the probes, and the electronics used for data collection are described. A description of the cold cathode ion source used in these studies is given along with a description of the computer codes used for the comparison between experimentally measured results and orbit tracking results.

Chapter 3 presents results of experimental measurement of the phase space occupied by the beam from the cold cathode ion source in several configurations in each case including comparisons with orbit tracking predictions. The results include different chimney slit shapes and different source arc currents. This information then

provides a basis for fixing design features of a new cyclotron so that beam trajectories match the caracteristics of the beam from the ion source.

Chapter 4 summarizes the conclusions reached in this study.

Chapter 2

Experimental Setup

2.1 The Source

The ion source used in the present study is a cold cathode PIG ion source. The source is nearly identical to the source used in Harper Hospital's K100 neutron therapy cyclotron in Detroit, Michigan (Harper Medical Cyclotron). (Specifically, the PIG source used in taking the data herein presented was designed for use in the 250 MeV proton medical cyclotron being built by the company ACCEL Gmbh for for use in the PROSCAN project of the Paul Scherrer Institute (PSI) in Villigen, Switzerland; data taking took place at the NSCL source testing facility.) Figure 2.1 shows a crossection view of the cathode-anode region of the source.

Several things are required for the source to operate correctly:

- There must be a magnetic field that is parallel to the chimney. Sources like the one used in these studies have been used in magnetic fields as high as 4.5 Tesla in the Harper Medical Cyclotron (and as low as 0.5 Tesla during low magnetic field tests in the NSCL ion source test stand).

- The source requires a steady flow of gas into the anode-cathode area. For

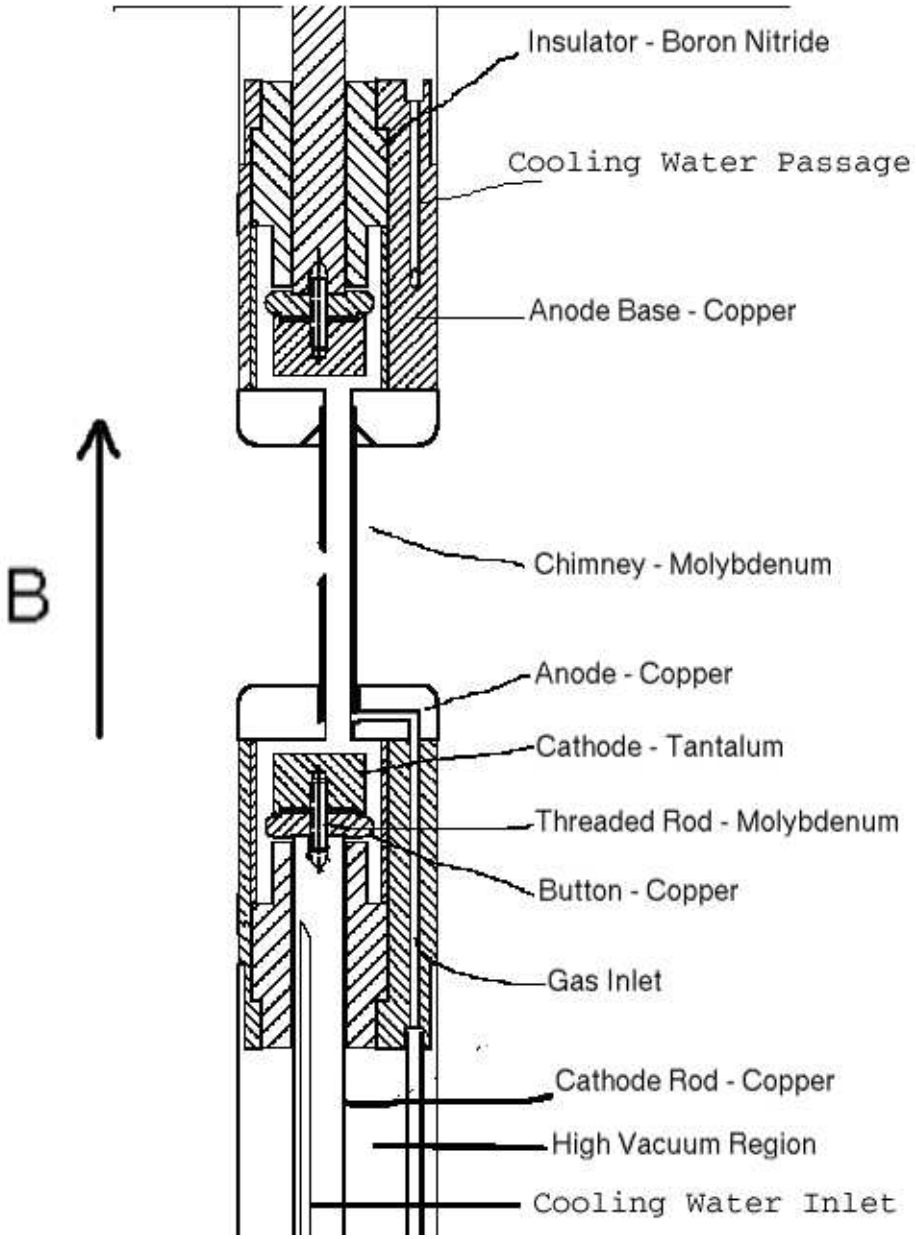

Figure 2.1: CAD (Computer Aided Design) drawing of the cathode-anode region of the ion source used for this study. (The cathode is off center corresponding to the position needed in the real cyclotron , whereas the chimney is on-center to match the position needed in the source teststand.)

the present study both hydrogen and deuterium gas were used. The gas was supplied to the source by a Sierra Instruments Series 810 Mass-Trak Flow Controller. Gas flow rates of 1.5 to 6.0 cubic centimeters (STP) per minute have been used at various times.

- There must be sufficient vacuum between the cathode rod and the outer shell of the source. The boron-nitride insulator, which is a tight fit, separates the high vacuum region behind the insulator (on the order of 10^{-5} Torr), from the lower vacuum region in the chimney and between the anodes and cathodes.

- There must be a sufficient potential difference between the anode and cathode to cause the arc to strike. For this source a Glassman High Voltage KL series high voltage supply rated at 3kV and 1A provided the necessary potential. When the plasma is established, the power supply shifts to current limited operation and the potential between the anode and cathode drops to the value required to sustain this current. The cathode anode gap was between 0.075" (1.9 mm) and 0.150" (3.8 mm) , and is not a critical parameter for the source's operation.

- The cathode surface must be prepared to facilitate the striking of the arc. The first step in preparing the cathodes was to sand them with 100 grit sand paper until the surface layer was removed and there was a uniformly rough surface. In the early studies the cathodes were then scratched with the end of a flat head screwdriver to further facilitate striking of the arc.[1] The result is shown in figure 2.2.

Figure 2.3 is a photograph of the lower half of the ion source. Water cooling for the cathode rod and the anode base are essential (some copper parts were melted when

[1] In later runs this was found to be unimportant and was omitted.

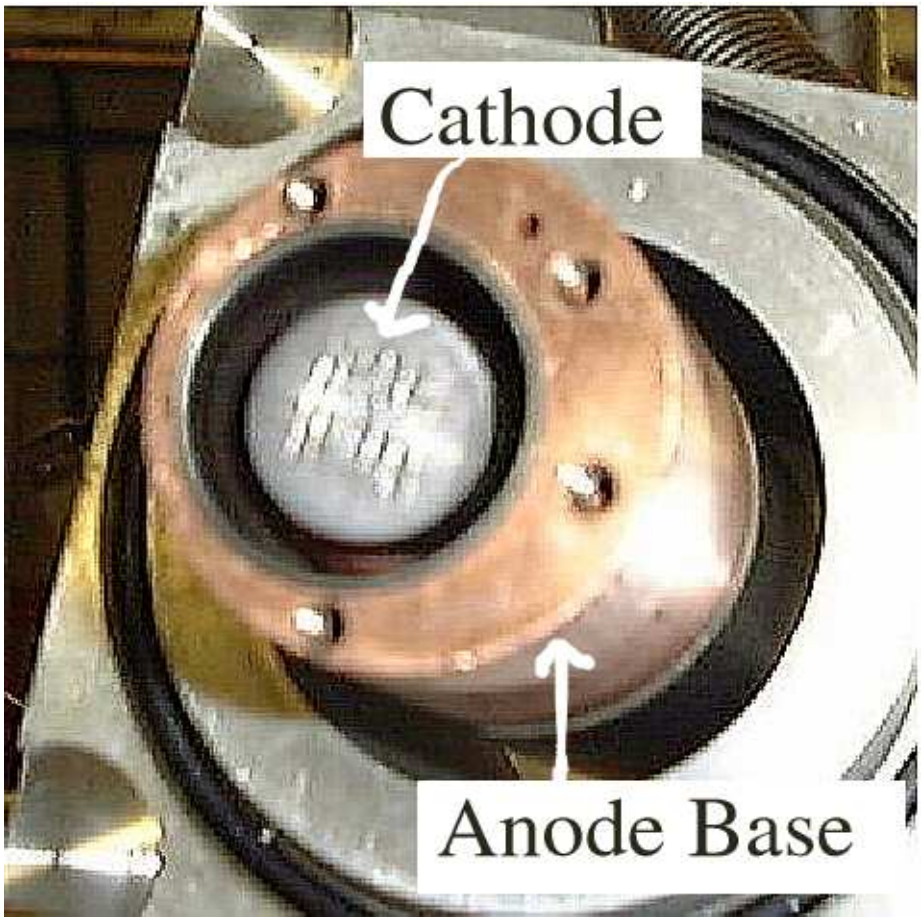

Figure 2.2: The anode has been removed from the end of the ion source to show the cathode. This cathode has been prepared by sanding the surface with 100 grit sandpaper and scratching the cathode with a screw driver.

the ion source was run without proper cooling). Further instructions on running this source in the ion source test stand are found in appendix A.

2.2 The Magnet

The magnet which was used for the ion source test stand was originally (circa 1967) a bending magnet in the beam line at the NSCL. Since being taken out of service as a bending magnet it has been the starting point for several cyclotron design studies [11]. The magnet is a room temperature electro-magnet with a pole radius of 13.875"

Figure 2.3: A photograph of the lower ion source half. (The upper half is a mirror image of the lower but without a gas inlet.)

(.352 m). This magnet was modified (circa 1996) for use as a cyclotron (the "High Intensity Test Cyclotron") including installation of a sectored pole tip with four hills, four valleys, and holes in the valleys for dee stems. A coil current of 100 A producing a central magnetic field of approximately 10 kilogauss was normally used for the ion source measurements described in this dissertation.

2.2.1 Modeling the Magnet with TOSCA

During the design of the High Intensity Test Cyclotron, the magnet was mapped in preparation for modifications suitable for a fixed energy cyclotron. Fieldmaps were taken at 51 A, 101 A, and 152 A. Figure 2.4 shows a map of the magnetic field at the 101 amp current setting. After these fieldmaps were taken, the magnet was modified for use as the Ion Source Test Stand; these modifications changed the magnetic field as will be shown in section 2.2.2.

After the magnet had been mapped, it was modeled with the three dimensional relaxation code TOSCA [19]. (TOSCA is part of the Opera 3-d software package produced by Vector Fields Inc.) TOSCA is used for calculating electric and magnetic fields in non-linear materials. Since the magnet has three symmetry planes, only one eighth of the magnet needed to be modeled. The shape of the steel (Figure 2.5) and coils was entered into TOSCA along with a B-H curve for standard steel. Differences between measured and calculated magnetic fields are shown in figure 2.6 and are generally smaller than 3%. These differences are believed to be due to the unavailability of a precise B-H curve for the steel in the magnet and are inconsequential relative to the goals of this dissertation. The TOSCA results were especially accurate for the 101 amp case.

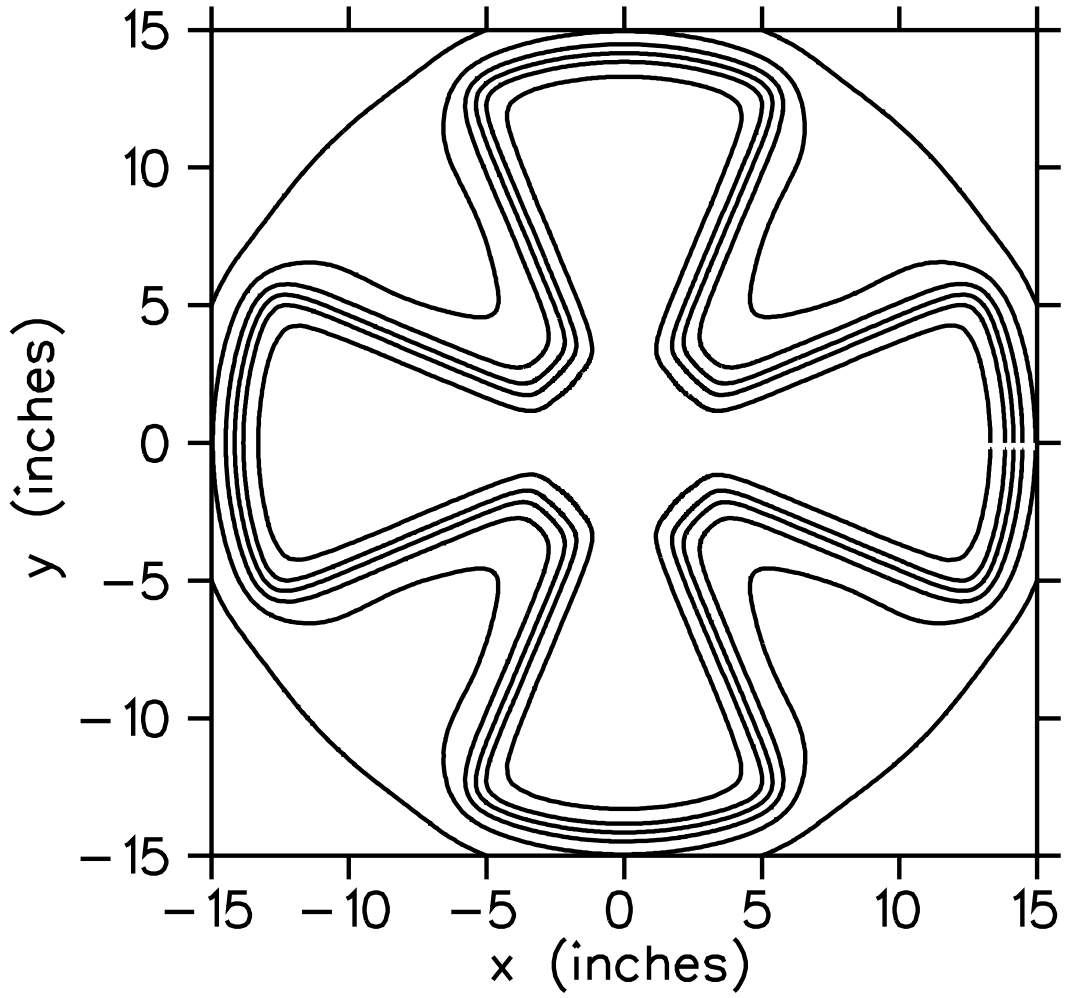

Figure 2.4: Shown is a measured magnetic field of the "High Intensity Test Cyclotron" version of the magnet i.e. before the "Ion Source Test Stand" modifications were made. The coil current for this measurement was 101 A. Magnetic field contours 3, 5, 7, 9, 11 and 13 kG from the outside working in; the maximum field being 13.6 kG.

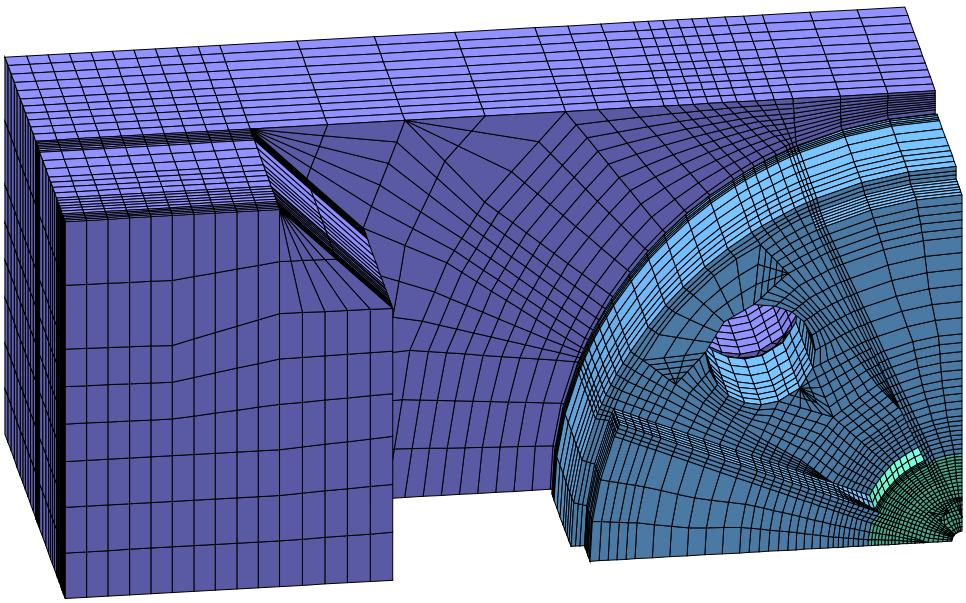

Figure 2.5: This figure shows a three dimensional model of the magnet steel shape used in TOSCA to calculate the fields of the ion source test stand magnet. Due to the symmetry, only $\frac{1}{8}$ of the magnet needed to be modeled.

2.2.2 Modifications to the Magnet and the Final TOSCA Model

Since the original field mapping and modeling of the High Intensity Test Cyclotron version of the magnet, changes have been made to the magnet to match the needs of using it as an ion source test stand. These changes involved:

- Removing spacers between the pole tips and the upper and lower yokes so that the pole tips would be in direct contact with the magnet yoke which increased the pole tip hill-hill gap from 1.5" (3.8 cm) to 2.25" (5.7 cm) without changing the exterior dimensions of the poles.

- Enlarging the hole through the center of the magnet to 1.375" (3.49 cm) to fit the ion source.

- Drilling and tapping various holes to allow vacuum feed-through fittings to be

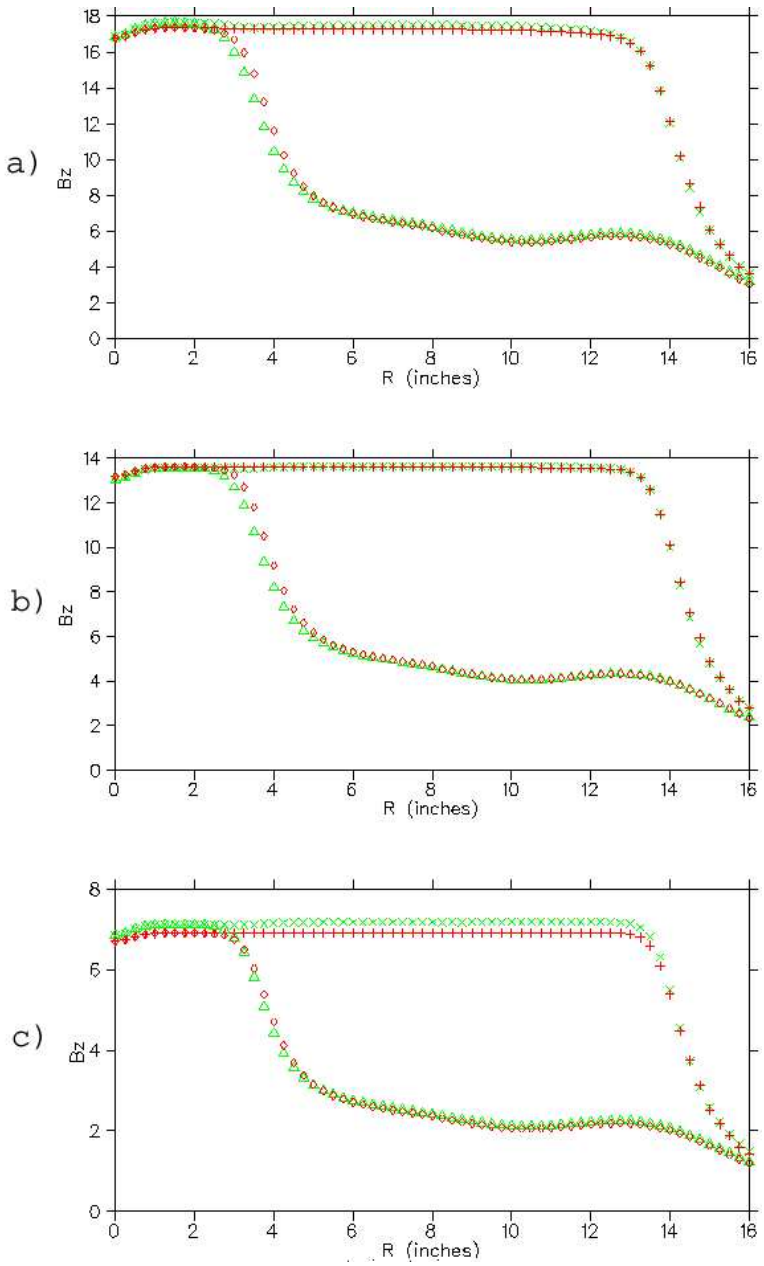

Figure 2.6: The measured magnetic field (×) of the High Intensity Test Cyclotron magnet, and the calculated magnetic field (+) from TOSCA along two azimuths,one along a hill and another along a valley, for coil currents of (a) 152 amps, (b) 101 amps, and (c) 51 amps.

bolted to the pole tips and yoke, etc.

- Modifying the coils by removing the central 4 pancakes of the original 16 double pancakes, in order to make more room between the coils (leaving 12 x 24 = 228 turns in the upper and lower coils combined).

In a cyclotron the beam makes many hundreds of turns in the magnet and a very precise knowledge of the magnetic field is necessary. In contrast, the beam travels through less than one turn in the Ion Source Test Stand, so a precise map of the magnetic field is not critical. Because TOSCA had proved reliable for predicting magnetic fields in our magnet to within a few percent, we decided not to re-map the magnetic field after the above modifications were made. Instead, the appropriate changes were made to the TOSCA model, and new calculations were run. The result was a calculated magnetic field that should accurately reflect the magnetic field in the ion source test stand to within 1 or 2 %, an accuracy which is quite sufficient for the goals of this dissertation study.

In his 1966 dissertation Mallory went to considerable lengths (a series of 15 machining operations on the pole tips of his magnet) to ensure that the magnetic field in his test stand was uniform. This was done to facilitate radial emittance calculations. Similar efforts were not taken for the ion source test stand used in the present study. Calculations showed that radial emittance of the beam could be accurately calculated even in the presence of small deviations from a flat field. Figure 2.7 is the magnetic field in the magnet as calculated by TOSCA. The field through which the beam passes varies by as much as five percent.

Finally, the magnetic field of the magnet was measured with a calibrated Hall effect probe. This was done to verify the absolute value of the magnetic field in the magnet. Figure 2.8 shows the location where the magnetic field was measured and a graph of field versus magnet current.

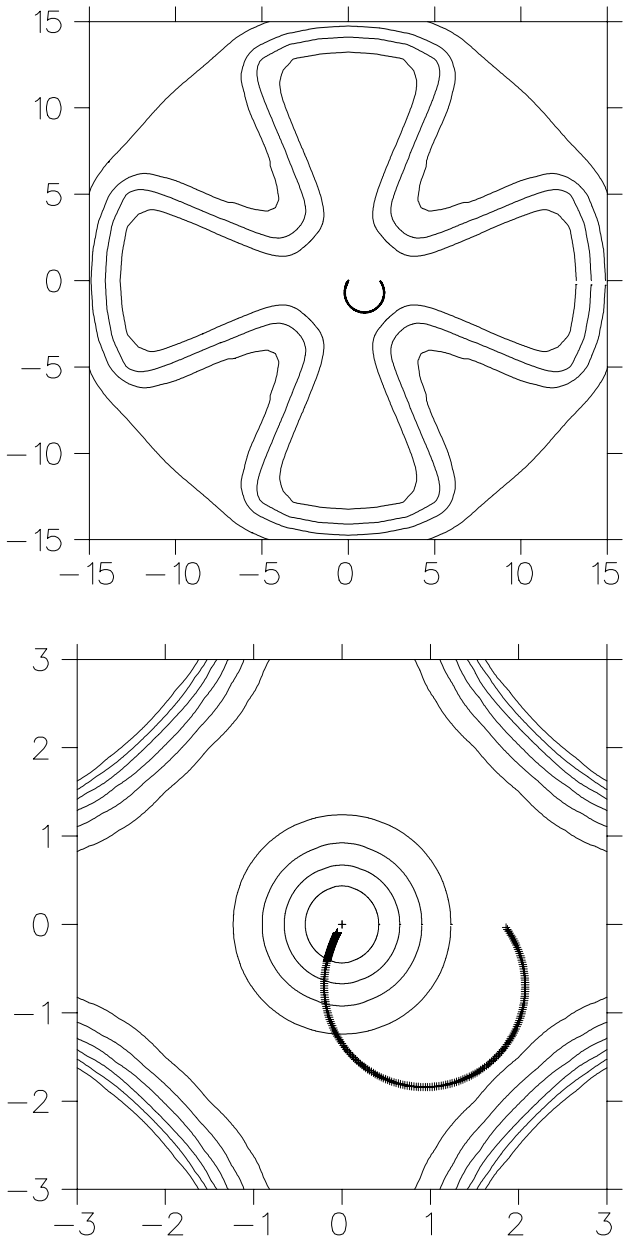

Figure 2.7: The magnetic field of the ion source test stand. The axes are labeled in inches. The top figure shows the magnetic field of the whole magnet. The effects of the hills and valleys are clearly visible. The contours are in 2 kGauss intervals (3, 5, 7, and 9 kG). The bottom figure shows just the central region. The contours are in 100 Gauss intervals (9.0, 9.1, 9.2, 9.3, 9.4, 9.5, and 9.6 kG),and represent a 1% change in the magnetic field. A typical orbit is shown on both graphs. The magnetic field through which typical orbits travel varies by approximately 5%.

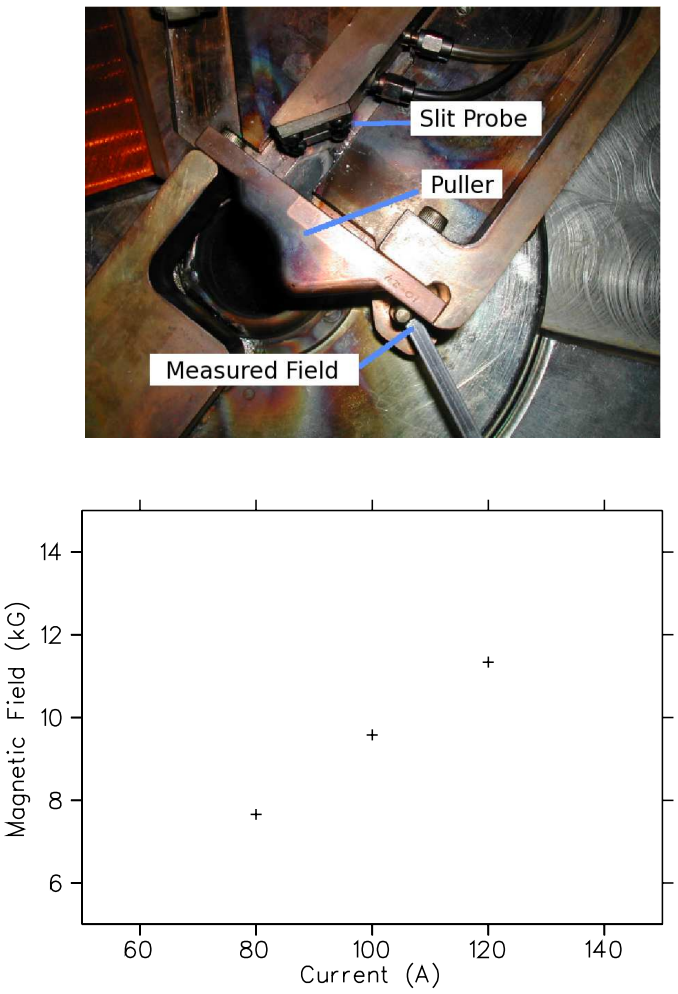

Figure 2.8: The photo shows the location where the magnetic field was measured. This location is the same distance from the center of the magnet as much of the beam's path. The magnetic field is graphed as a function of coil current in the magnet. A coil current of 100 amperes was used for the measurements presented in this dissertation.

2.3 The Vacuum System

The limiting factor for the required vacuum in the ion source test stand was the ion source itself. Experience with similar ion sources in the Harper Medical Cyclotron showed that for the ion sources to run consistently, there needs to be a base vacuum (with the ion source gas supply turned off) in the 10^{-6} Torr range.

The vacuum system for the ion source test stand makes use of the pole tips as the primary vacuum wall. Six "plugs" were manufactured to seal six of the eight dee stem holes. Two stainless steel tubes were inserted into the remaining two dee stem holes which served as the mounts for two turbo pumps. Various turbo pumps ranging from 600 to 800 liters/second were used, and these turbo-pumps were backed by a mechanical roughing pump.

Two thermo-couple gauges and one ion gauge were used to monitor the vacuum. The thermo-couple gauges were capable of measuring pressures of 1 to 1000 mTorr. The ion gauge had pressure scales of 10^{-4}, 10^{-5}, 10^{-6}, 10^{-7}, and 10^{-8} Torr.

The best vacuum achieved in the ion source test stand (with source gas supply turned off) was 8×10^{-7} Torr. With a gas flow rate of 2.5 cc/min of hydrogen, the pressure in the main vacuum chamber is around 4×10^{-5} Torr.

2.4 DC Extraction and Measurement

High voltage is supplied to the dee by a Spellman High Voltage power supply which is rated at 100 kV and 2 mA. Figures 2.9, 2.10, 2.11 and 2.12 show the high voltage dee. The puller provides the electric field that extracts the beam from the ion source. The part of the beam that hits the slit probe or the beam shield is blocked. The part of the beam that passes through the 0.010" (.25 mm) slit continues in its orbit around to the wireprobe.

Three currents are of interest. The total current drawn from the dee power supply (as read from the front panel of the power supply) tells us the total beam that is being extracted from the ion source including beam that is blocked by the puller (plus a possible "dark current" emitted from the surface of the dee). The second current is the so called "slit current." This current is the total current that hits the slit probe and the beam shield. Except for the small portion of the beam that passes through the slit, this current represents the total beam that passes through the puller. The third current is the current hitting the wire. This current is related to the phase space density of the beam at the location in phase space determined by the location of the slit and the wire.

The two parameters s and w are also recorded. These parameters are related to the position of the two probes as shown in figure 2.12. Sections 2.4.1 and 2.4.2 describe how s and w relate to the actual positions of the slit and wire in the magnet.

2.4.1 Relating Radial Emittance Probe Parameters (s and w) to the Position of the Probes

In order for the current measured on the wire to be meaningful, the locations of the slit and wire must be known. The ion source test stand does not simply record the x and y coordinates of the slit and the wire. Instead, it records two parameters s and w, which specify the location of the slit and wire probes in their respective tracks (figure 2.12).

The coordinate system for the ion source test stand is defined such that the center of the magnet is at (0,0). The center of the chimney is also located at this point (0, 0). The slit probe travels on a line that is parallel to the y-axis such that the slit stays 0.247" (6.27 mm) to the right of the origin, i.e.

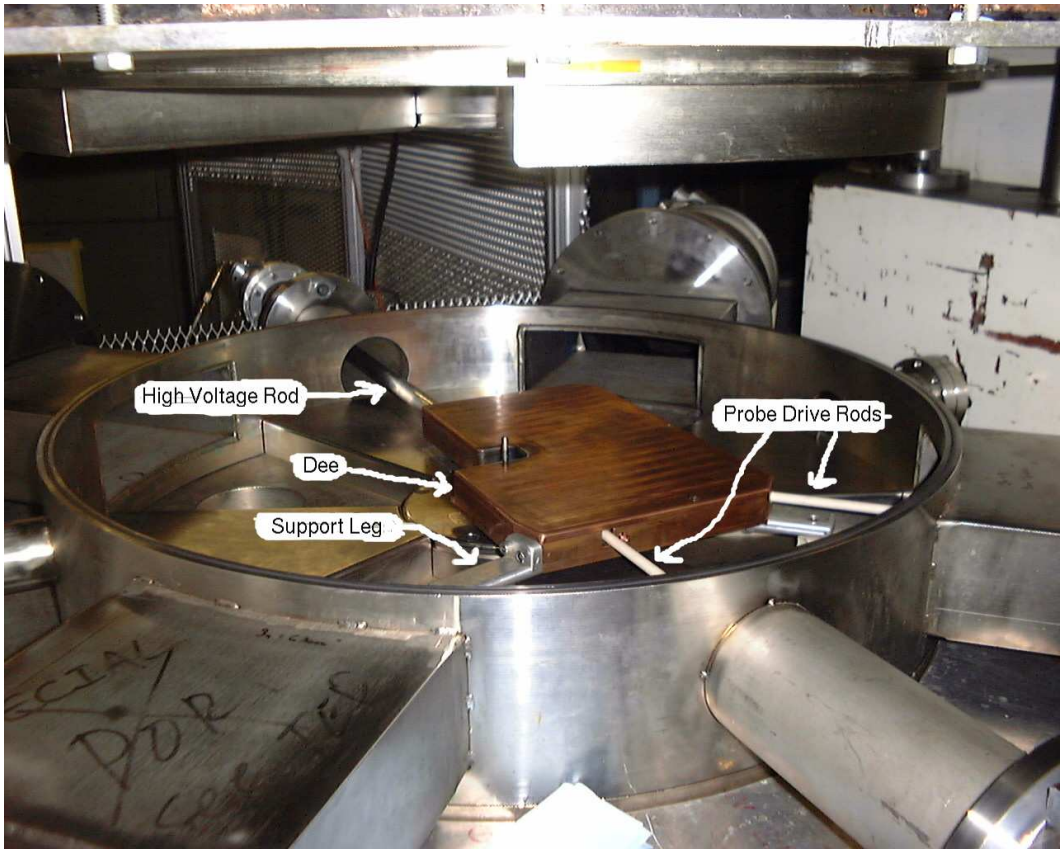

Figure 2.9: The high voltage dee is supported by three aluminum support legs which each are supported by insulators. The probe drive rods are also insulating. The high voltage rod contains all the electrical and water cooling lines. It passes through a feed-through insulator into the high voltage cage on the back of the magnet.

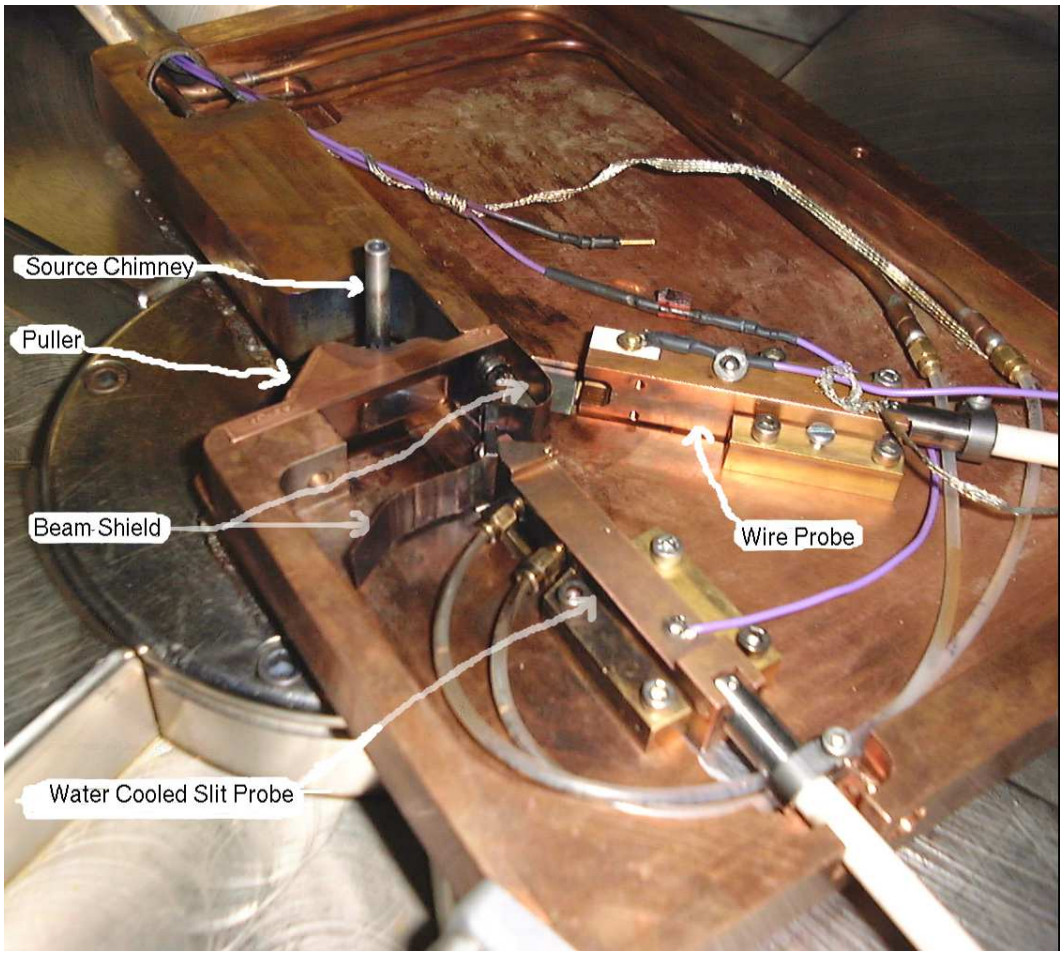

Figure 2.10: Visible are the slit and wire probes used for radial profile measurements along with water cooling lines. The beam shield prevents any beam from hitting the water cooling lines or passing in front of the slit probe and hitting the wire.

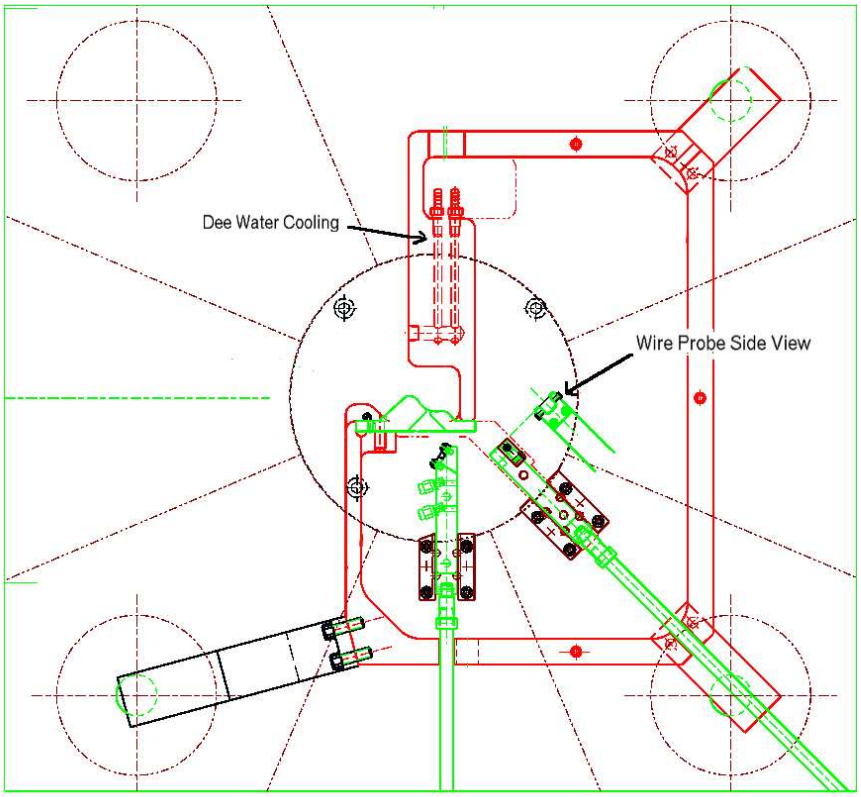

Figure 2.11: Drawing of High Voltage Dee.

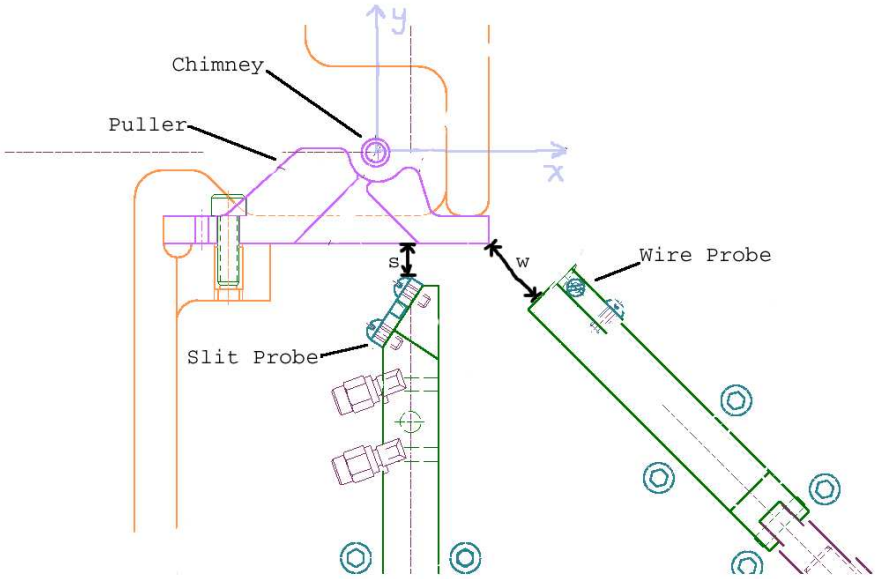

Figure 2.12: A CAD drawing of the central part of the ion source test stand. Visible are the chimney, puller and the slit and wire probes. Parameters s and w are recorded along with the current on the slit probe and the current on the wire for each data point. Parameter s is defined as the distance from the back edge of the puller to the front tip of the slit probe. Parameter w is defined as the distance from the corner of the puller to the front edge of the wire probe.

$$x_{slit} = 0.247\text{”} \tag{2.1}$$

$$y_{slit} = -1.113\text{”} - s \tag{2.2}$$

The wire probe travels such that the wire stays on the line $y_{wire} = -x_{wire} + 0.650$”. When parameter w is equal to zero the wire is at (x =1.196”,y =-0.626”). For other values of w:

$$y_{wire} = -0.586\text{”} - w \sin 45^\circ \tag{2.3}$$

$$x_{wire} = 1.236\text{”} + w \cos 45^\circ \tag{2.4}$$

2.4.2 Relating Axial Emittance Probe Parameters (s and w) to the Position of the Probes

For the axial emittance experiments, the slit and wire probes were attached to an axle. When the probe drive shaft moved in and out, the probe would rotate around the axle moving the slit or wire up and down in z (figure 2.13). Parameters s and w were recorded for each current measurement. These numbers represent the linear position of the slit and wire probe drive shafts respectively. The probes have a maximum angular displacement of 3 degrees. Using small angle approximations, the change in z for the probes is calculated from the change in the probe drive position:

$$\begin{aligned} \Delta z_{slit} &= \frac{A}{B} \Delta s \\ \Delta z_{wire} &= \frac{A}{B} \Delta w \end{aligned} \tag{2.5}$$

Where A and B are defined as shown in figure 2.13.

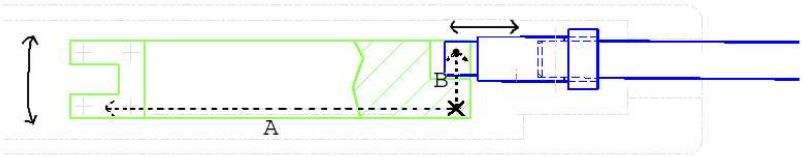

Figure 2.13: A CAD drawing of the z slit probe. The slit (not shown) is mounted on the left side of the probe. As the probe drive shaft moves in and out, the probe rotates on the axis (marked with an X). The ratio of the lever arms A and B is 6.5:1 for the slit probe and 5.3:1 for the wire probe. The recorded value s is the linear position of the probe drive.

2.5 Data Collection

Data collection on the ion source test stand is computer controlled. The positions of the probes are set with servo motors and read from a potentiometer (figure 2.14). The current on the slit probe and the current on the wire are read by standard NSCL beam current monitors "BCMs." The BCMs have amplifiers and a one-board computer that makes the current readings available over Ethernet.

The BCM must float at high voltage in order to read the currents on the slit and wire. Power is provided to the BCM through an isolation transformer, and fiber optic cables are used to connect the BCM to the labs local area network. All of the high voltage components that are outside of the magnet are located in a high voltage cage (figure 2.15). The cage is interlocked such that the high voltage power supply will not turn on until the high voltage cage door is closed.

A program written by Mark Davis of the NSCL runs the data collection process. The program (sequencer.exe) takes an inputfile like the following.

```
MIN:2.2 MAX:3.2 SET:N1PRBW SET:N1PRBE READ:N1BCMW READ:N1BCME
N1PRBW:0.1300 N1PRBE:0.6400 MIN:10 MAX:10
N1PRBW:0.1300 N1PRBE:0.6500
```

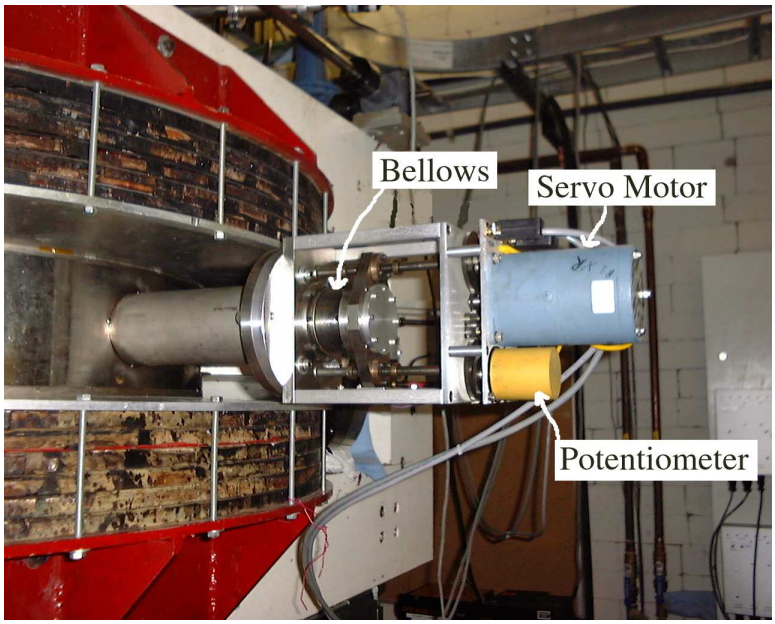

Figure 2.14: Probe Control Servo.

```
N1PRBW:0.1300 N1PRBE:0.6600
N1PRBW:0.1300 N1PRBE:0.6700
...
```

The first line sets some global behavior for the data collection run. MIN and MAX are the minimum and maximum time the program will wait between data points. This time is to allow the probes to get to their new positions. SET tells the program which variables it will be setting and READ tells the program which variables it will be reading. In this case the position of the two probes N1PRBW (the slit probe parameter s) and N1PRBE (the wire probe parameter w) are being set and the two BCM channels N1BCMW (the slit current i_s) and N1BCME (the wire current i_w) are being read. Subsequent lines in the input file are "set" values of parameters s and w for each measurement and (optionally) how long to wait before moving the probe to the next setting. The output from sequencer.exe appears as follows:

```
0.131684377789497  0.646714597940445  0.000280803549685515  -3.04795241845568E-6
0.131684377789497  0.656622079014778  0.000280850820126943  -3.21202242048457E-6
0.131684377789497  0.666515201330185  0.000276029750239104  -6.82156206721629E-6
```

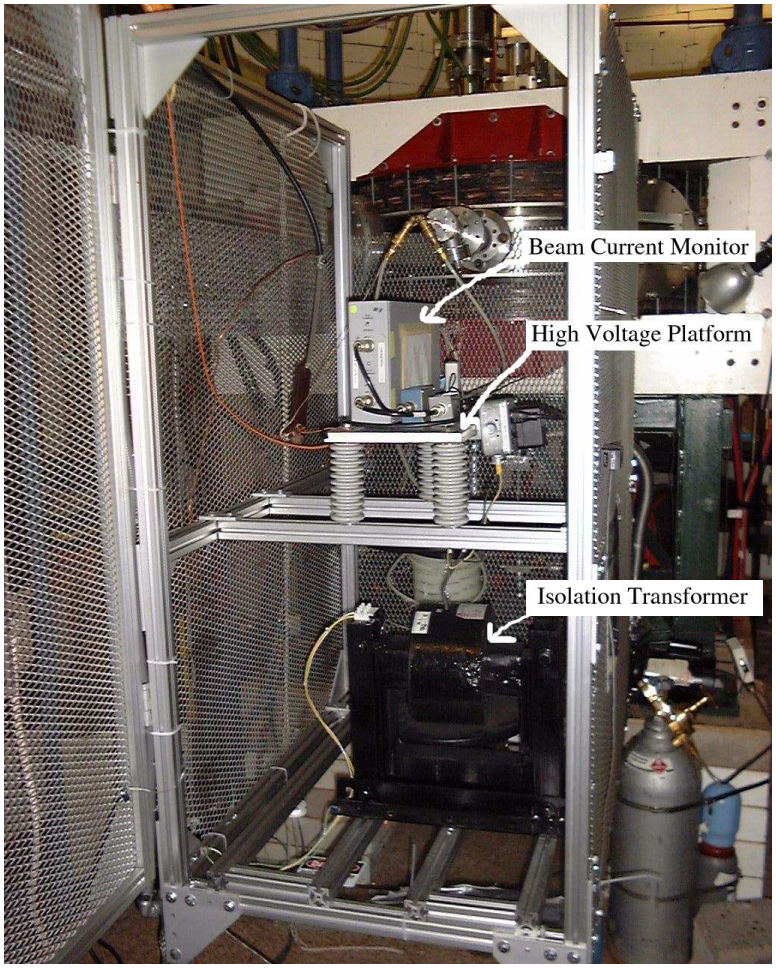

Figure 2.15: A photograph of the high voltage cage. The isolation transformer provides A/C power to the components on the high voltage platform. The Beam Current Monitor was custom built by the NSCL staff for our project. It amplifies and reads the current on the slit and wire probes and makes the values available over the local area network.

```
0.131684377789497  0.676966148614883  0.000275840690301266  -5.80432842980372E-6...
```

The four columns of numbers are the slit probe parameter s, the wire probe parameter w, the current on the slit probe (i_s) and the current on the wire (i_w) respectively. The actual position of the probes (as measured by the potentiometer) rather than the set values are recorded. The slit current is recorded in amps. The wire current is recorded in hundredths of an amp. The wire current for the points recorded above are in the noise (10^{-8} amp range). For a typical beam, peak wire currents will reach as high as 10 microamps. A typical data run will have 1000 to 3000 data points.

2.6 The Orbit Tracking Code

The NSCL code Z3CYCLONE was designed for tracking orbits from the ion source slit all the way to extraction in a cyclotron neglecting forces generated by other particles i.e. a "single particle" calculation. Numerical maps of the electric field (in a rectangular grid) and of the magnetic field (in a polar grid) are required as input. From the Z3CYCLONE Instruction Manual Version 4.0:

> The Z3CYCLONE program actually consists of three separate parts which have been woven together so as to make possible the calculation of an ion orbit starting from the source slit (or [spiral] inflector) all the way out to the extraction system.
>
> - Part I tracks the ion from the [ion] source [or from the inflector] to just beyond the puller, the integration is done in Cartesian coordinates with time as the independent variable. ...
> - Part II [tracking] continues [from Part I to] the edge of the electric field or until the wanted turn number is reached. This part uses θ

as [the] independent variable and the integration is done in polar coordinates. ...

- Part II and Part III differ mainly in the way they treat the rf electric field. ...

The default behavior of Z3CYCLONE is to use an electric field on the dees (and puller electrodes) that alternates with a given rf frequency. Part I (and only Part I) has an option to use a constant voltage electric field. This feature, along with the ability to use a small time step make Part I uniquely useful for calculating the path of the beam in the dc ion source test stand. Part I was modified in two ways for use in the calculations presented here.

As section 2.7.2 will show, an electric field grid with small node spacing (0.00125" or 0.032 mm in x and y and 0.004" or 0.10 mm in z) is required to accurately model the shape of the chimney slit. If this small spacing was used to calculate the electric field for the entire ion source test stand (a region 2.5" x 2.5" x .75" or 63mm x 63mm x 19mm) the electric field grid would have over 750 million nodes. To facilitate faster relaxation times the electric field grid was therefore divided into a field with small grid spacing covering the region between the chimney and the puller, and a second electric field with coarser grid spacing covering the region inside the high voltage dee. This allowed each field to have less than 20 million nodes resulting in much faster electric field calculations. (Normally Part I only allows one electric field so the code was modified to allow the use of the two electric fields.)

The code was also modified to output only the slit and wire crossings of each calculated orbit (this behavior mirrors the experimental data collected by the ion source test stand). In its original form, Part I saves the location of the ion at each time step in the integration (time steps of 22 ns in the small field and 89 ns in the larger field were used) to a file. This file can then be used to plot the orbits. For some

calculations, over 500,000 orbits were tracked, each of which had several hundred time steps. The output files produced by these runs would be too large to be useful (over 15 GB). (A version of Part I with the full orbit output was retained for use when detailed knowledge of the calculated orbit was needed.)

2.7 Initial Conditions

Given a set of initial conditions (position and velocity), and the magnetic and electric fields as a function of time, the orbit code Z3CYCLONE will calculate the position and velocity of a charged particle at each subsequent time. While Z3CYCLONE has proved to be a reliable orbit tracking program, orbit calculation is only as accurate as the initial conditions it is given and the selection of accurate initial conditions can be complicated in a cyclotron with an internal ion source. To obtain the initial conditions used for the orbit calculations presented in this dissertation we have used a technique taken from the doctoral dissertation [11] of J. R. Schubert "Extending the Feasibility Boundary of the Isochronous Cyclotron." Schubert's work showed that changes as small as several thousandths of an inch (hundredths of a mm) in the shape of the plasma boundary (the surface with electric potential equal to that of the chimney of the ion source) can have a large effect on beam trajectories under rf extraction. Accurate ray tracking then requires accurate knowledge of the plasma boundary, the initial direction of the ions as they exit the ion source, and the initial energy of the ions.

An ion source is of course a multi-particle system of very large dimensionality while Z3CYCLONE is a single particle code. "Plasma boundary," "initial direction," and "initial energy" are then approximate concepts which we adjust and compare with experiment in order to identify rules which will cause the orbit trajectories given by Z3CYCLONE to concur with observed trajectories to the most accurate degree

achievable with single particle computations.

The interior of the ion source houses a hot plasma of high dimensionality whereas the exterior is a high vacuum region where single particle calculations are known to be accurate predictors of beam behavior. We therefore guess that the equipotential surface which goes across the exit slit of the chimney (at the same electric potential as the chimney) will be a likely place for a single particle calculation to begin. Schubert's work then introduced a fictitious central electode in the interior of the ion source (called the "image electrode") with an adjustable potential. Changing the potential of this electrode provides a way of changing the shape of the equipotential surface across the source exit opening (the assumed "plasma boundary") from convex to flat to concave. Searching on this parameter and on the initial energy then allows us to achieve an optimized match between experimental beam properties and single particle computations.

2.7.1 Generating The Ensemble of Rays for Tracking

To approximate a real beam of particles with an orbit code, it is necessary to track many rays. The tracked rays should represent the full range of reasonable orbits for ions in the beam. As a starting point, a grid of "primary rays" are evenly spaced in the source opening. For example, in the chimney with an opening 0.020" (0.50 mm) wide and 0.196" (5.0 mm) tall we choose to have 403 primary rays with 13 evenly spaced starting positions across the width of the opening and 31 starting positions evenly spaced vertically in the opening. All primary rays are started on the plasma boundary with an initial velocity perpendicular to the plasma boundary (figure 2.16).

For each primary ray, a collection of rays, each of which have a different initial direction of motion, is tracked.

The starting angles in r and z are centered around the primary ray's starting

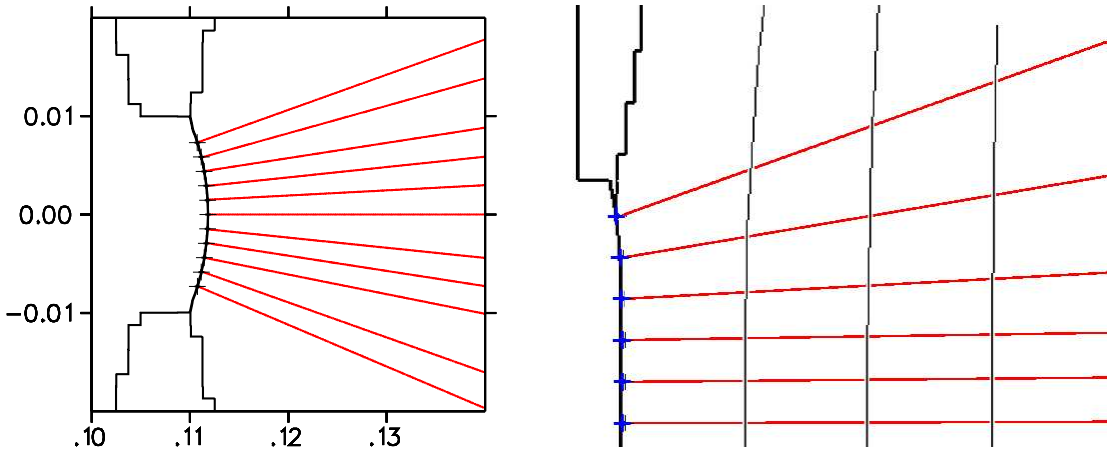

Figure 2.16: Shown are (left) 13 starting locations in the median plane and (right) the top 6 out of the 31 vertical starting locations along the center of the slit and each of these primary ray starts on the plasma boundary as shown. Each primary ray starts with a velocity vector pointing perpendicular to the plasma boundary. (The "v" shaped apparent double valued potential just above the highest ray is not allowed outside of a conductor and is believed to be a plotting artifact - its effect is negligible.)

velocity and are evenly spaced with steps of $\Delta\theta = \frac{1}{N} \times 120°$, where N is the number of different starting angles in the r or z direction. If we use a total of 49 starting directions ($N_z = N_r = 7$) we are then up to a total of 19,747 tracked orbits.

For each primary ray, and for each starting angle, rays are started with five different starting energies representing an approximation of the expected Maxwell-Boltzmann distribution of particle energies in a plasma at a given temperature. (See appendix B for a full description of how the energies are chosen.) The temperature of the plasma then is used in calculations is a parameter that is varied in order to best match experimental results.

Finally, to include the effect of variations in the dee voltage, rays are tracked with several different accelerating voltages ranging from the nominal accelerating voltage plus or minus a small variation in N_{dee} equal steps. (It was observed on an oscilloscope that the accelerating voltage fluctuated with time as seen in figure 2.17, namely a steady 60 Hz fluctuation along with apparently random fluctuations.) For a 40 kV

nominal accelerating potential, we used a variation of ±120 V.

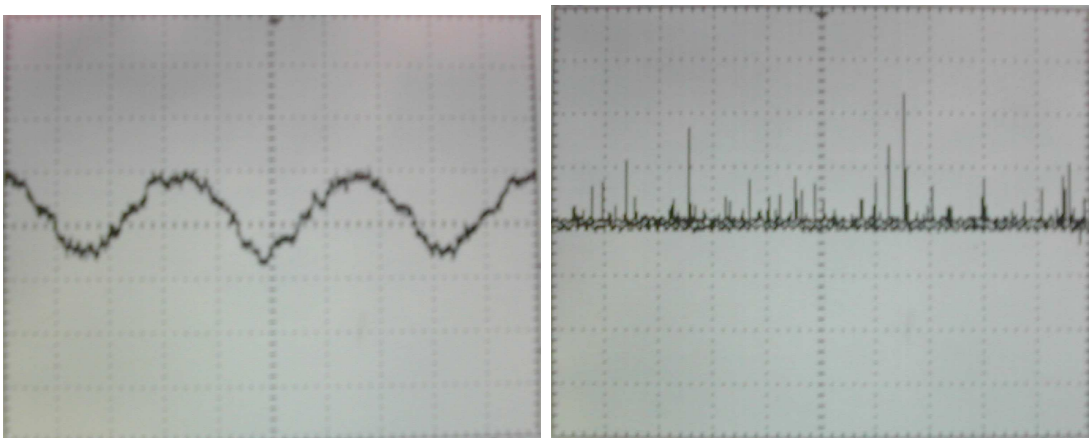

(a) The average of 64 traces (A/C coupling) on a 5 V/div scale shows an approximately 7 V (about 0.04%) 60 Hz ripple in the dee voltage.

(b) In "peak detect" mode at 100 V/div the oscilloscope shows several voltage spikes above 200 V and many voltage spikes in the 30 to 40 V range. These spikes represent about 0.2 % of the nominal dee voltage.

Figure 2.17: Dee Voltage Fluctuations (17 kV nominal dee voltage.)

If we choose $N_{dee} = 4$ then the total number of tracked orbits reaches 394,940. A computer code was developed to calculate the correct initial conditions for each ray and produce the input files used with Z3CYCLONE for the calculations presented in this dissertation.

Positioning the Primary Rays

The plasma boundary is a three dimensional curved surface and we want to test the hypothesis that each calculated ray starts on this surface. To accomplish this, each ray is initially placed 0.025" (0.64 mm) outside of the chimney opening, well outside of the plasma boundary. The starting point is moved back toward the chimney opening, if the potential is still negative (outside the plasma boundary) the point is moved back again. This repeats until the point is found to be greater than 0 V. An interpolation

is done between the last two points to find the exact location of the zero potential contour. Figure 2.16 shows with + signs the starting positions calculated with this technique.

The primary rays are started with initial velocity perpendicular to the plasma boundary i.e. in the direction of the local electric field. To calculate this direction, E_x, E_y, and E_z were determined from the six grid points closest to each starting position and the angles $\alpha_z = \arctan(\frac{E_z}{\sqrt{E_x^2+E_y^2}})$ and $\alpha_r = \arctan(\frac{E_y}{E_x})$ were determined. Figure 2.16 shows Z3CYCLONE tracked "orbits" with the electric and magnetic field turned off so that the initial direction of motion can be seen.

2.7.2 Plasma Boundary Calculations

The calculations of the electric field between the source chimney and the dc "puller" were made with the three dimensional Laplace equation solver Relax 3d [13]. To get an accurate representation of the opening in the chimney it is important that the width of the opening represent "many" gird points. The slit chimneys have slit widths of 0.010" (0.25 mm) and 0.020" (0.51 mm), and the hole chimney has a 0.047" (1.19 mm) diameter opening. For these calculations, a grid size of 0.00125" (0.032 mm) in the horizontal $(x-y)$ plane and 0.004" (0.10 mm) in the vertical (z) coordinate was used.

Of interest is the the 0 V equipotential surface in the chimney slit. As stated previously, for the calculations presented in this dissertation, all particles will be started on this surface, and since this surface represents the edge of the ion plasma in the chimney, we refer to it as the "plasma boundary." As also previously discussed (in section 1.4), Dr. Schubert introduced a cylindrical "image electrode" with an arbitrary positive voltage on the axis of the chimney [11, p29]. This image electrode does not represent any physical object, but is used to provide a constant electric field

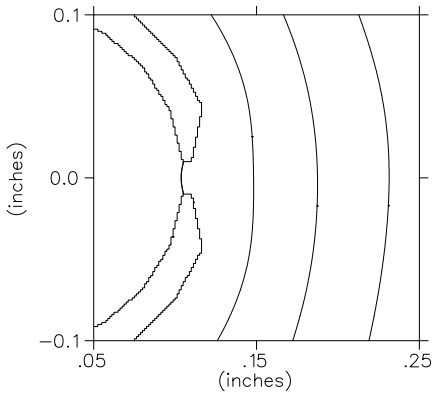

(a) Concave Plasma Boundary. Image Electrode: 4 kV

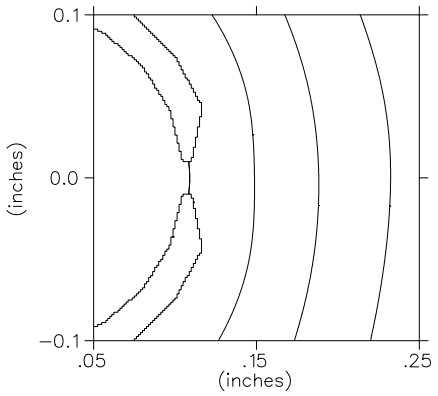

(b) Nearly Flat Plasma Boundary. Image Electrode: 16 kV

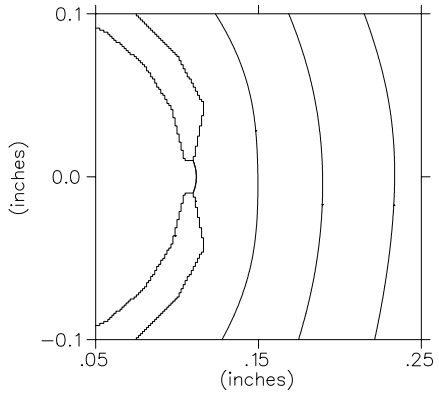

(c) Convex Plasma Boundary. Image Electrode: 32 kV

Figure 2.18: The graphs show electric equipotentials (-8, -16, and -24 kV) and the chimney (0 V). Of interest is the shape of the zero volt contour as is crosses the chimney slit (the assumed plasma boundary).

derivative at the plasma boundary. This is important for the electric field interpolation done in Z3CYCLONE. Putting voltages of varying levels on the image electrode has the additional effect of changing the shape of the plasma boundary thus exploring the effect of possible different plasma pressures.

Figure 2.18 shows three different plasma boundaries which are the result of different voltages for the image electrode. There is no a priori reason to choose one of these conditions over the others, since all represent valid solutions to Laplace's equation with the known boundary conditions (the voltage of the image electrode, chimney and puller).

The effect of the plasma boundary on the beam as it leaves the chimney is seen in figure 2.19. Lower image electrode voltages produce a concave plasma boundary which produces a focusing electric field. Looking carefully at figure 2.19a we see that ions which start away from the center of the chimney slit cross over the center of the beam and thereafter diverge in much the same fashion as the convex plasma boundary (produced by higher image electrode voltages) which produces a defocussing electric field from the beginning as seen in figure 2.19c. Intermediate image electrode choices produce a flat plasma boundary as seen in figure 2.19b. Since any of these beam profiles can reasonably be expected from the chimney-puller geometry, only an experiment can determine which best corresponds to the actual beam.

Changes in the shape of the plasma boundary of course also change the locations that the tracked rays cross the slit and wire probes in the ion source test stand for both radial and axial measurements. We therefore use this to directly compare calculated orbits with the experimental (s, w) data.

For the orbit tracking calculations presented in figures 2.19 and 2.20, 32,643 rays were traced for each plasma boundary. As noted previously, the rays started at 13 equally spaced positions horizontally across the opening of the source slit and 31

equally spaced positions vertically in the source slit. For each of these 403 starting positions, 81 rays were traced with nine equally spaced starting angles in the horizontal plane and nine equally spaced starting angles vertically with 3 eV as the starting energy for each ray. Unlike the final calculations presented in Chapter 3, no spread in starting energy or acceleration potential is used (since these spreads are not needed to see the effect of plasma shape).

Figure 2.20 shows graphs of radial wire probe parameter w as a function of the slit probe parameter s for six sets of rays. The shape of the beam in these radial plots changes when different image electrode potentials are used in the calculation. Similarly, figure 2.21 shows axial (s, w) graphs for the same sequence of image electrode potentials used in figure 2.20.

2.7.3 Initial Energy

In section 2.7.2 rays were started with different positions and different starting angles, but all rays were started with 3 eV of initial kinetic energy. In this section we investigate what happens to the beam when different starting energies are used in the calculation. In Chapter 3, when comparing calculations to experimental data, rays will be tracked with a range of energies with plasma temperature being an adjustable parameter (as discussed in appendix B). In this section (2.7.3), to emphasize the effect of starting energy on the calculations, only one starting energy is plotted at a time.

Figure 2.22 shows radial wire probe crossing versus slit probe crossing (s, w) plots for several different choices for the initial energy of the ions. Immediately we see that increasing the starting energy has the effect of increasing the width of the beam in the w coordinate. Figure 2.23 shows axial wire probe crossing versus slit probe crossing (s, w) plots for several different choices for the initial energy of the ions. The

width of the beam in w and s is affected by the choice of initial energy. Thus when compairing computed rays with various starting energies to experimental data, the size of the beam in (s, w) plots will determine which starting energy best represents the measured beam.

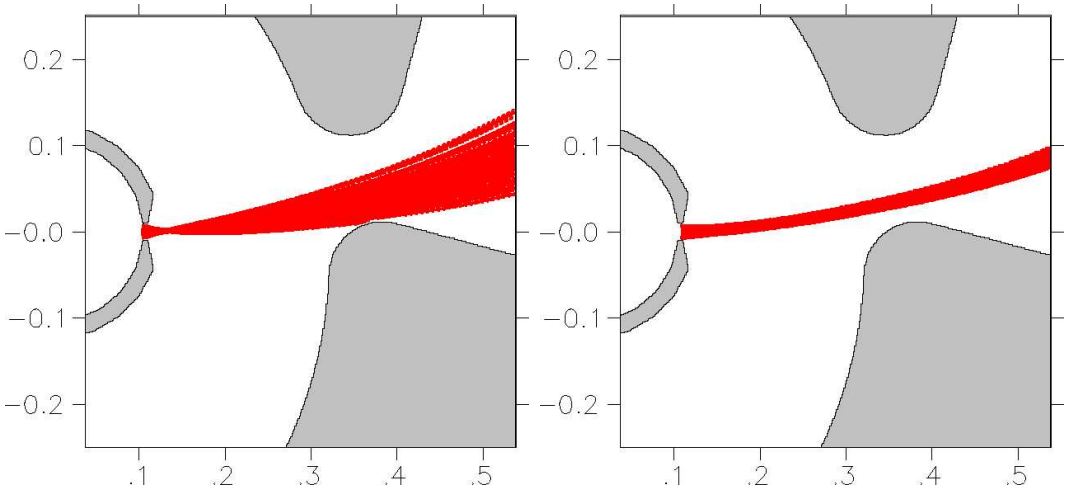

(a) 4 kV Image Electrode: Concave Plasma

(b) 16 kV Image Electrode: Nearly Flat Plasma

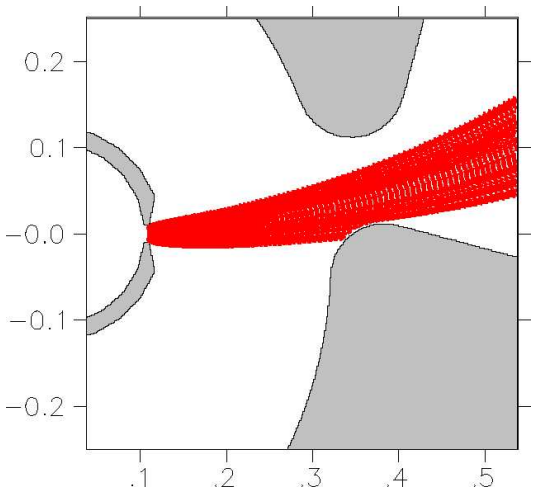

(c) 32 kV Image Electrode: Convex Plasma

Figure 2.19: Each orbit is started on the plasma boundary (zero equipotential surface) with an initial energy of 3 eV. Without knowing the shape of the plasma boundary, we do not know which of these beams will be produced by the ion source.

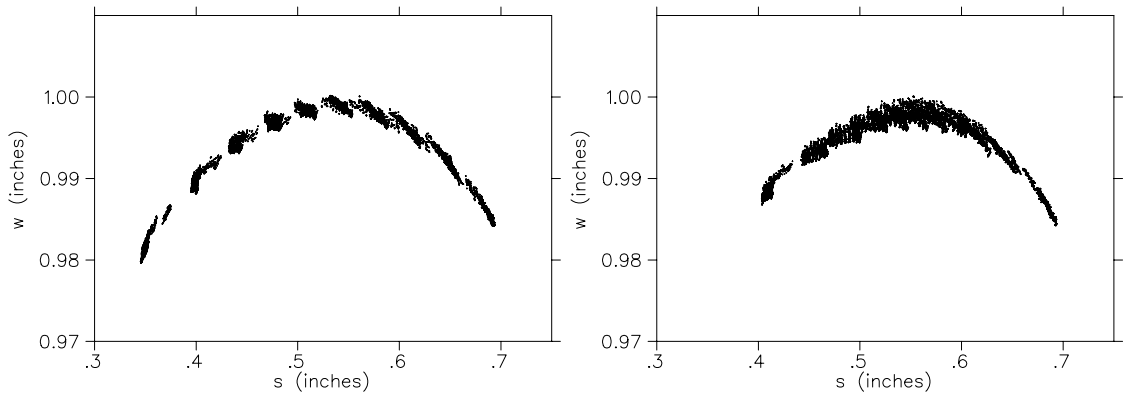

(a) 4 kV Image Electrode

(b) 8 kV Image Electrode

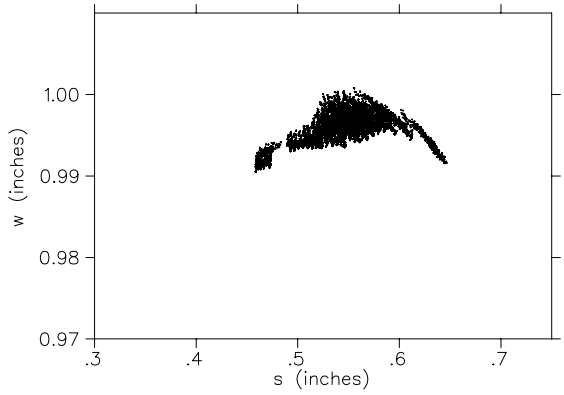

(c) 12 kV Image Electrode

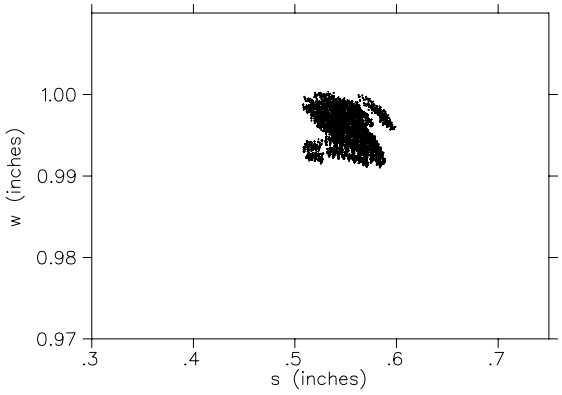

(d) 16 kV Image Electrode

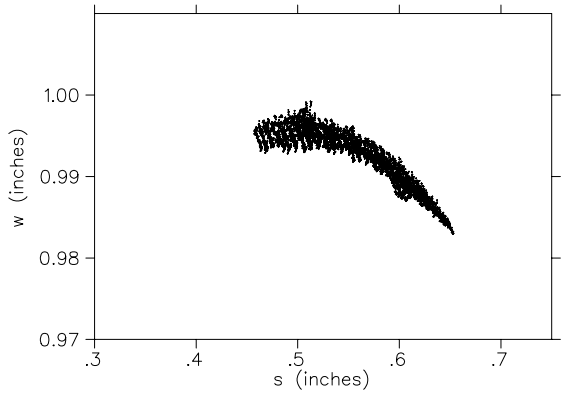

(e) 24 kV Image Electrode

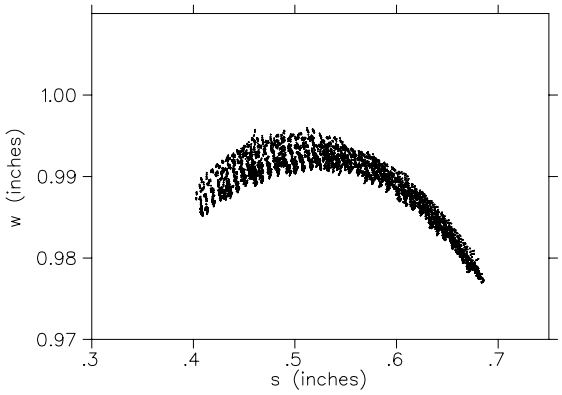

(f) 32 kV Image Electrode

Figure 2.20: Radial wire probe parameter w (inches) is plotted versus slit probe parameter s (inches) for calculated orbits started on the plasma boundary (zero equipotential surface).

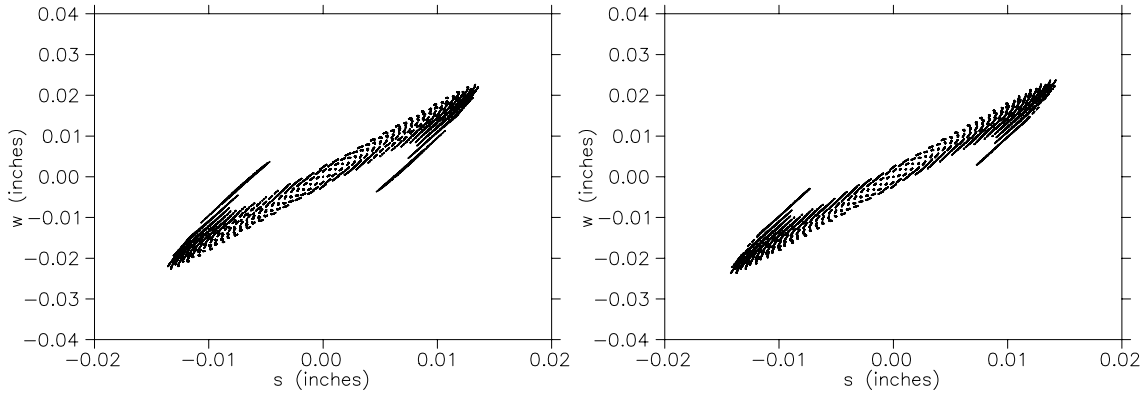

(a) 4 kV Image Electrode

(b) 8 kV Image Electrode

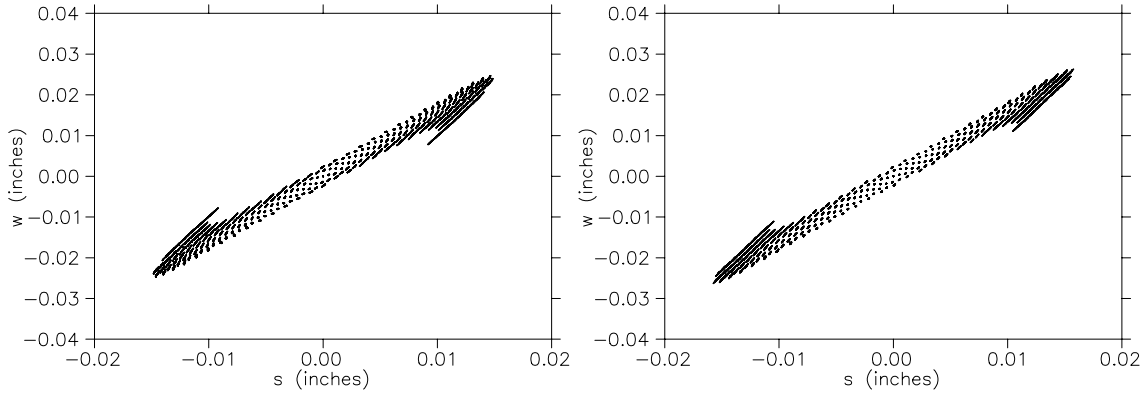

(c) 12 kV Image Electrode

(d) 16 kV Image Electrode

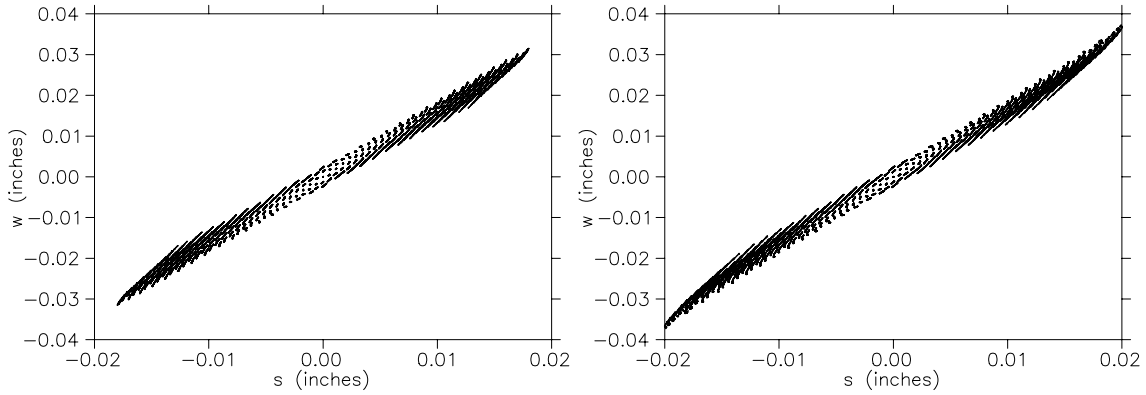

(e) 24 kV Image Electrode

(f) 32 kV Image Electrode

Figure 2.21: Axial wire probe parameter (w) is plotted versus slit probe parameter (s) for calculated orbits started on the plasma boundary (zero equipotential surface).

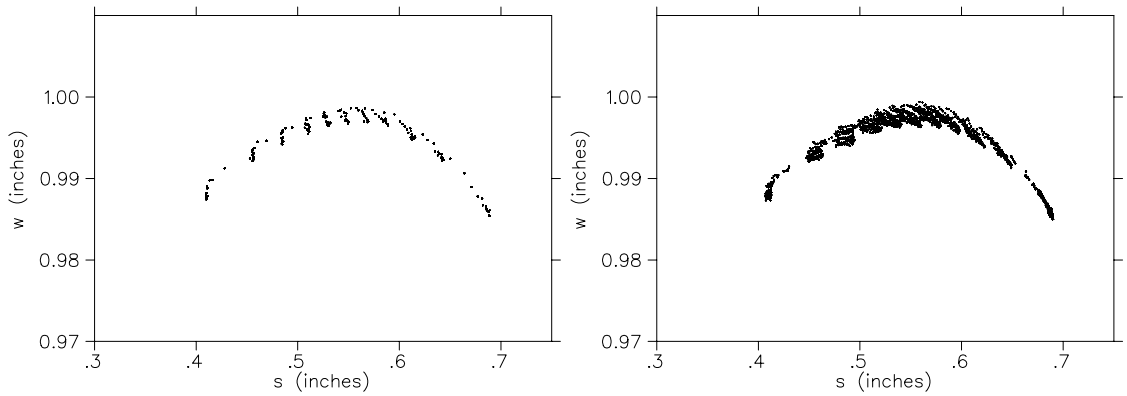

(a) 0.3 eV Starting Energy

(b) 1 eV Starting Energy

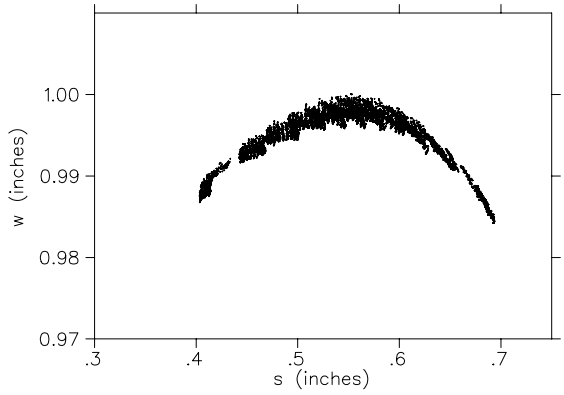

(c) 3 eV Starting Energy

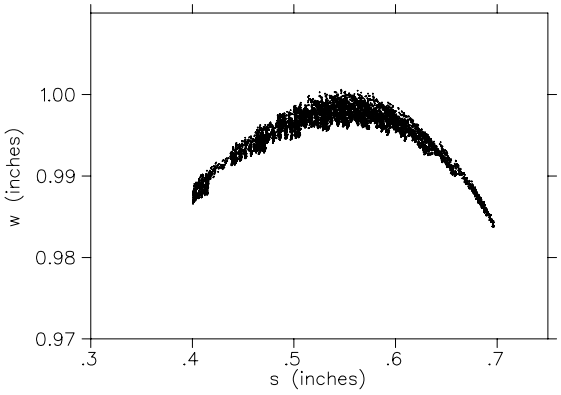

(d) 6 eV Starting Energy

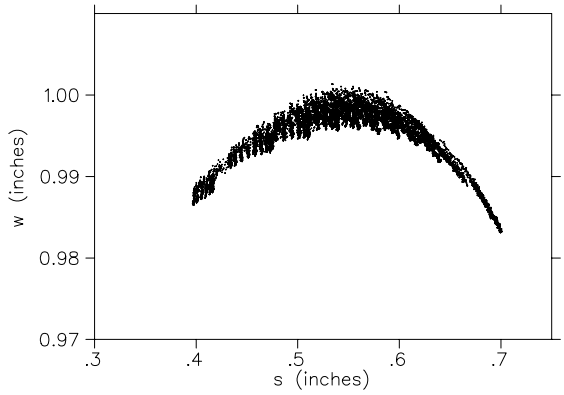

(e) 10 eV Starting Energy

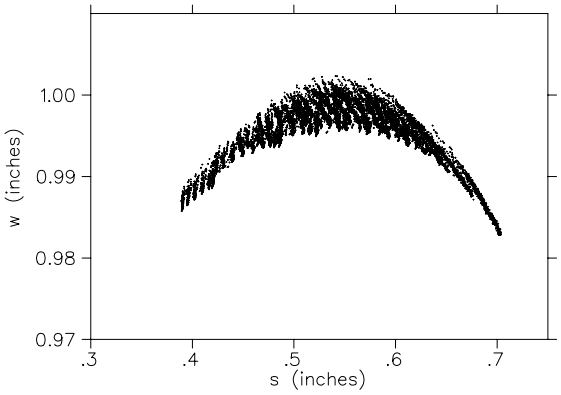

(f) 20 eV Starting Energy

Figure 2.22: Radial Wire probe parameter w (inches) is plotted versus slit probe parameter s (inches) for calculated orbits started on the plasma boundary (zero equipotential surface).

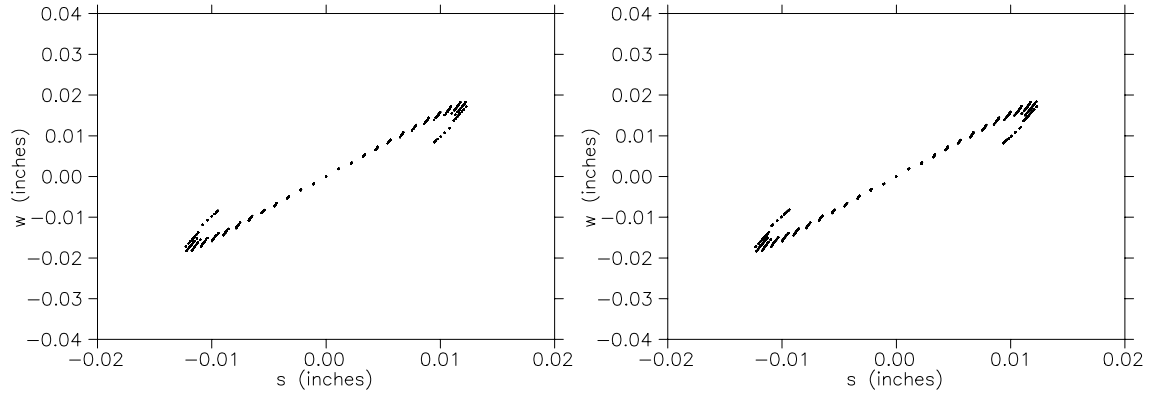

(a) 0.3 eV Starting Energy

(b) 1 eV Starting Energy

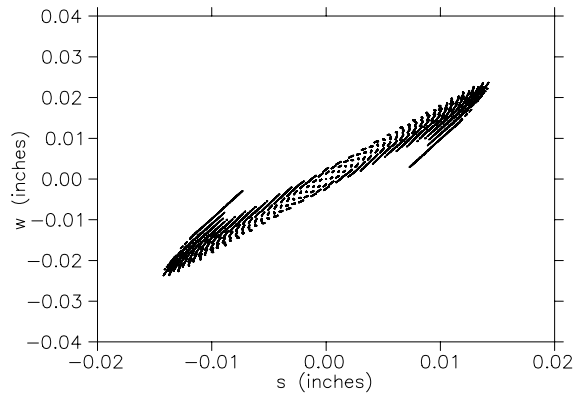

(c) 3 eV Starting Energy

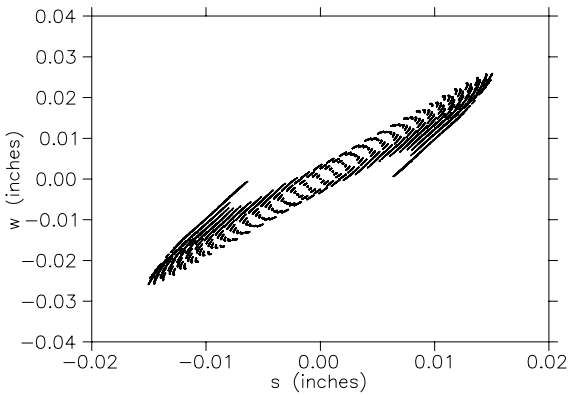

(d) 6 eV Starting Energy

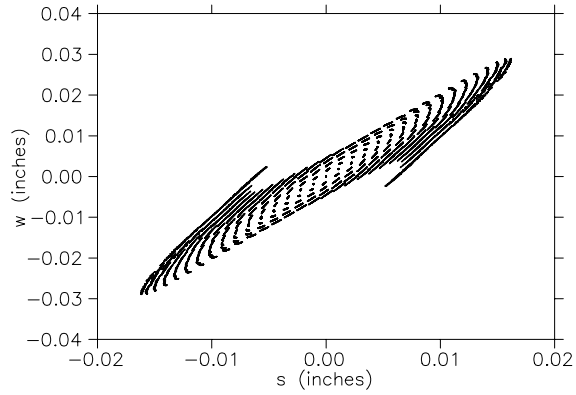

(e) 10 eV Starting Energy

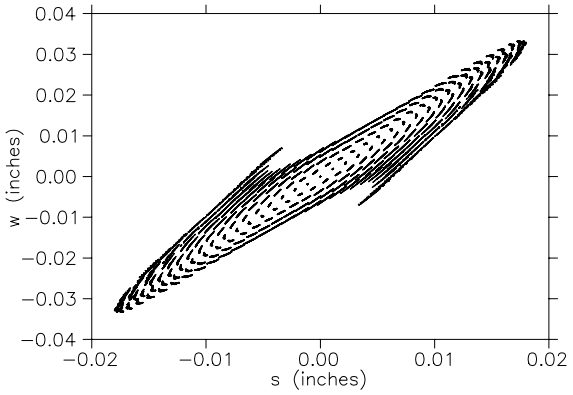

(f) 20 eV Starting Energy

Figure 2.23: Axial Wire probe parameter w (inches) is plotted versus slit probe parameter s (inches) for calculated orbits started on the plasma boundary (zero equipotential surface).

Chapter 3

Results

In this chapter the methods used to analyze the data from the ion source test stand are explained (section 3.1). The emittance and luminosity of the beams that were extracted from the ion source using three different chimneys and two different pullers are reported (section 3.2), and compared with calculated families of rays (section 3.3).

3.1 Experimental Methods

3.1.1 Understanding the Graphs

Figure 3.1a is a typical graph of radial emittance data from a measurement run in the ion source test stand. The parameter s which gives the location of the slit probe is plotted on the horizontal axis and the parameter w which gives the position of the wire probe is plotted on the vertical axis. (Geometrical descriptions of s and w were given in figure 2.12.) For radial measurements presented in this dissertation, the wire thickness is 0.005" (0.13 mm) and the slit width is 0.010" (0.25 mm). Axial measurements use a 0.015" (0.38 mm) wire and a 0.010" (0.25 mm) slit.

The s and w values at which current readings are taken show as a grid of + signs and the current measured at a point is represented by the size of the + symbol shown

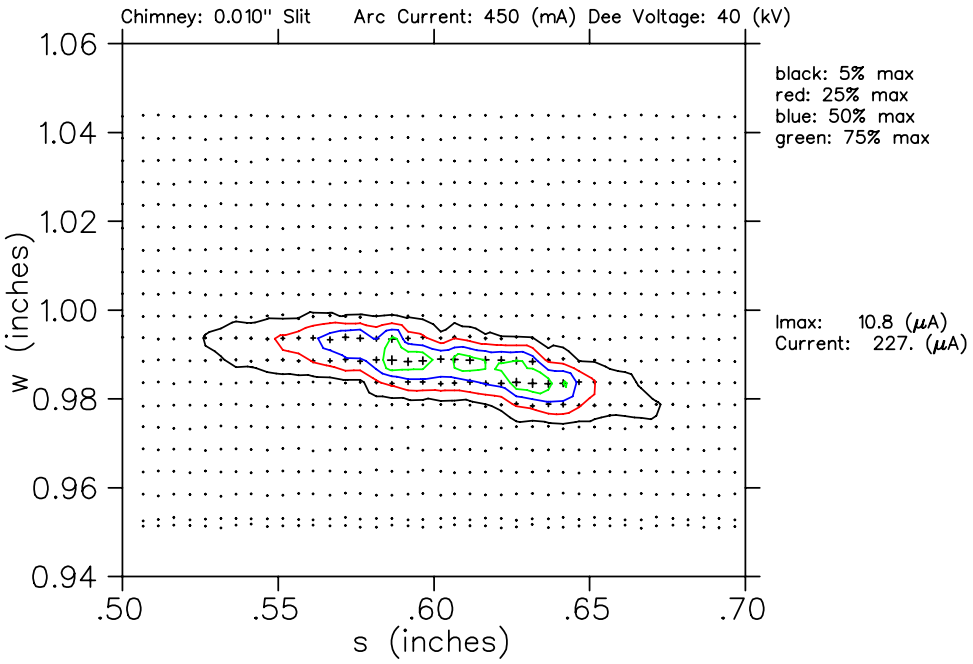

(a) Radial (s, w) Beam Contours

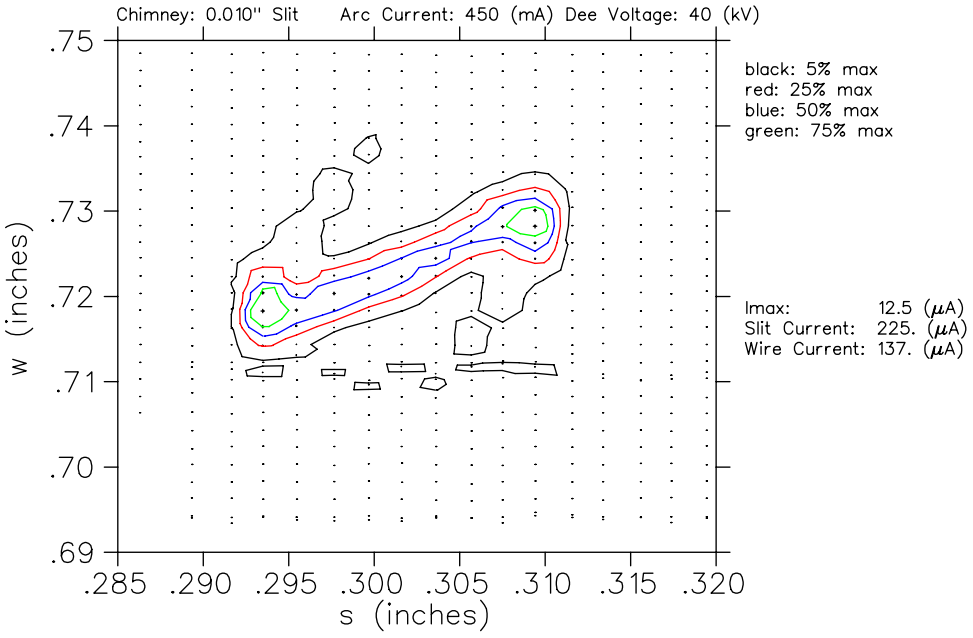

(b) Axial (s, w) Beam Contours

Figure 3.1: Typical graphs of the s and w data. (Parameters s and w give the position of the slit and wire probes respectively as described in sections 2.4.1 and 2.4.2.)

at that point. If the current was very small, the + appears as a dot. Overlaid on the grid are interpolated contours of constant wire current. They help in visualizing the size and shape of the beam in (s,w) parameter space. "I_{max}", the "slit current" and the "wire current" are recorded with each radial (s, w) plot. I_{max} refers to the maximum current read on the wire. The slit current refers to the total current measured on the slit probe when the probe is moved to a location where no beam is passing through the slit, thus it is a measure to the total beam current that passes through the puller.

Figure 3.1b is a typical graph of data from an axial emittance experiment in the ion source test stand. The parameters s and w are again plotted on the x and y axis respectively. (A geometrical description of s and w for axial measurements is given in section 2.4.2.) The grid and contours used in the axial data graphs have the same meaning as they do in the radial data graphs.

3.1.2 Repeatability of the Data

An important indication of the accuracy of a data set is the repeatability of the data. Figure 3.2 shows two consecutive runs on the ion source test stand. Qualitatively, the beams cover the same region of the graph. The total integrated current hitting the wire probe (the sum of the currents at every s and w point) differ by 10%. Other repeated measurement showed similar levels of consistency.

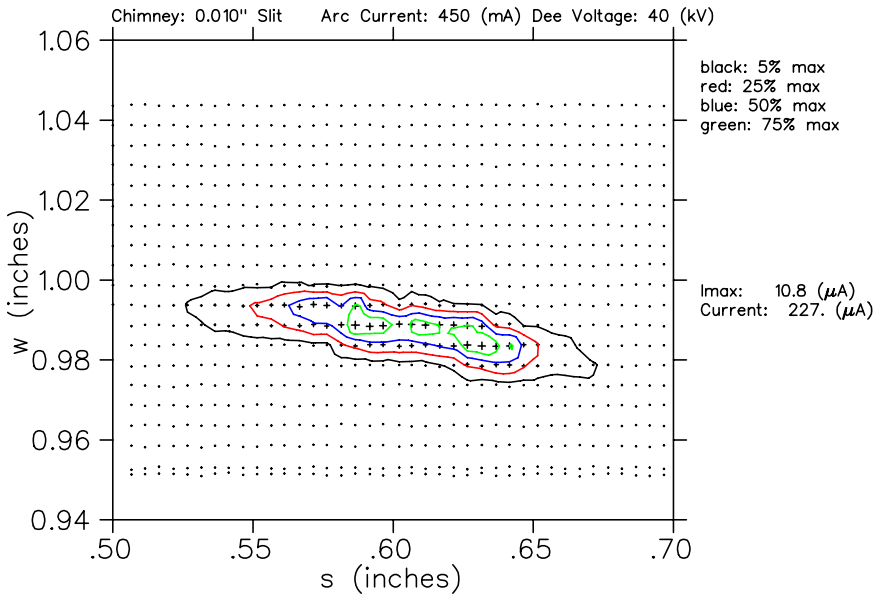

(a) Run number 18 from July 2003

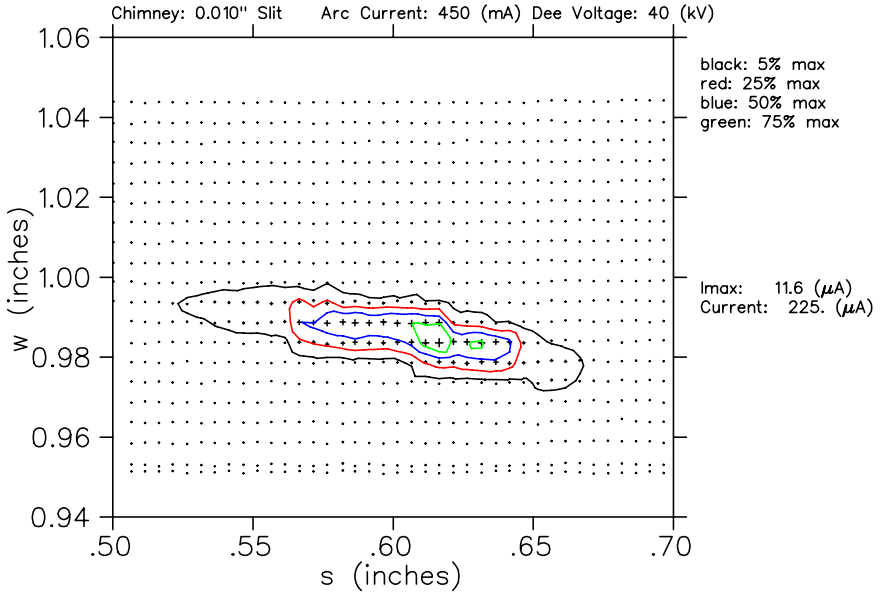

(b) Run number 19 from July 2003

Figure 3.2: The two graphs show two runs in the Ion Source Test Stand. The parameters for the ion source (arc current, puller voltage, gas flow, chimney geometry, etc) were held constant. The graphs have a qualitatively similar shape showing that the slit and wire probes measured current at the same locations in each measurement. The total current measured by the wire probe in the two measurements differ by 10%.

3.1.3 Converting Raw Data into Radial Emittance Plots

The raw data that are measured by the ion source test stand include: the slit probe parameter (s), the wire probe parameter (w), the current on the slit probe (i_s)[1] and the current on the wire (i_w). (See figure 2.12 for geometric descriptions of the parameters s and w.) To calculate the emittance of the beam we need to know the (perpendicular) radial width of the beam and the divergence (angular spread) of the beam.

Figure 3.3 shows a beam which has been mostly blocked by the slit probe. The origin of the polar coordinate system is chosen to be at the center of the beam i.e. it is equidistant from the center of the source opening, the central slit position and the central wire position. Each slit probe position s for which some beam passes through the slit has an associated radius r, the distance from the origin of the polar coordinate system to the slit. The range of r values then is the radial width of the beam.

For each slit position, current is read on the wire probe at a range of wire probe positions indicating that the beam diverges after the slit i.e. there is a range of angles (α_r) that the beam makes with the unit vector $\hat{\theta}$. Each wire probe location where a non-zero wire current, i_w, is measured has an associated angle α_r. The spread of α_r values then is the divergence of the beam.

To determine the range of angles α_r, we need to know the path that each ray takes from the slit location to the wire locations. Two methods (both approximate) present themselves. The first method is to use Z3CYCLONE (our orbit tracking code) to find orbits which start in the chimney opening, pass through the specified slit location and arrive at the various wire locations. To provide accurate results, these

[1]For data taken after June 10, 2004 the beam current measured on a beam stop downstream of the wire probe is recorded as i_s. After this date the current on the slit probe is measured with an analog gauge and recorded manually.

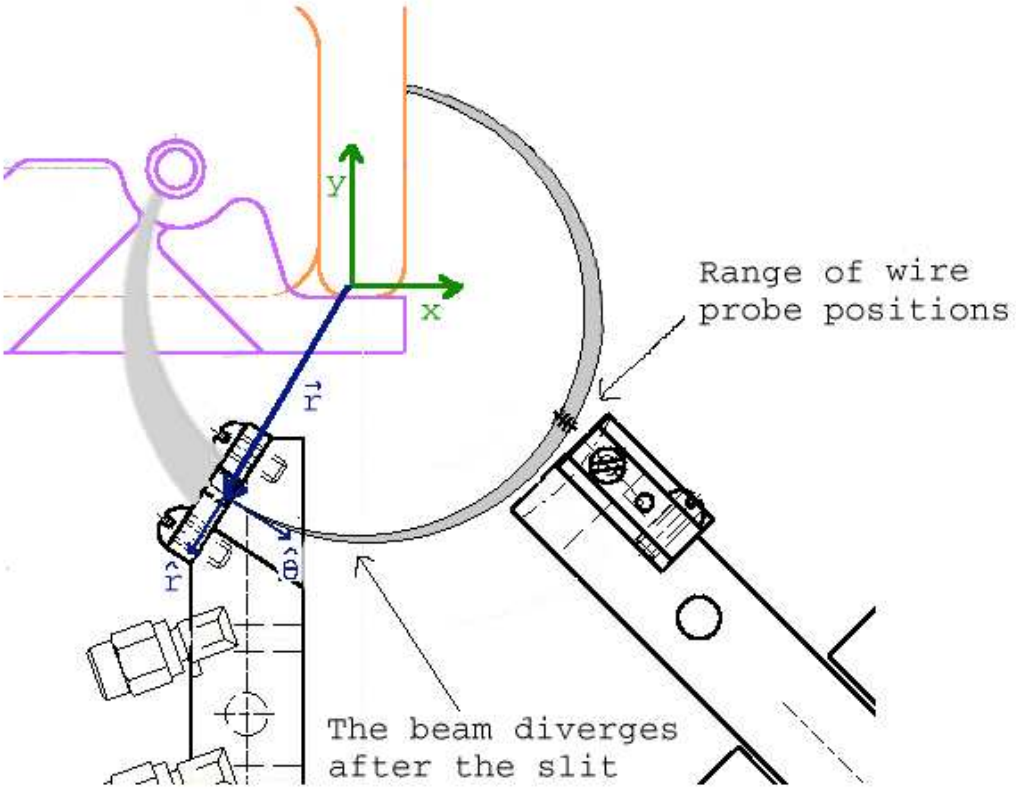

Figure 3.3: r is the distance from the origin to the point where the beam passes through the slit. α_r is the angle that the beam makes with the unit vector $\hat{\theta}$

orbits should have the same accelerating potential (dee voltage) as the experimental beam thus having the same curvature as the experimental beam. The second method is to find circular "orbits" which start at the specified slit location and arrive at the various wire locations. To provide accurate results, these circular orbits should closely approximate the curvature of the experimental beam. This is accomplished taking the circle which passes through the center of the chimney opening, the central slit position, and the central wire position as the reference location (r_0).

These methods were tested on a sample case to ensure that they give consistant results. The sample data points have the same slit parameter ($s = 0.5353$") and wire parameters differing by about 0.005" ($w = 0.9677$" and 0.9626" respectively). Figure 3.4 shows the tracked rays and the circles that pass through these two data points. The divergence, as determined by the tracked rays is 4.72 mrad. The circles give a divergence of 4.44 mrad; a difference of 6%.

Finding a tracked ray that starts in the chimney opening, goes through a specified slit location and ends at a specified wire location involves a multi-parameter search; namely finding the correct starting location in the chimney opening, the correct starting angle, the correct starting energy, and the correct puller voltage. In contrast, fitting a circle of given radius to two points (the slit location and the wire location) is trivial. Since the methods give very similar results and the difference in computing efficiency is enormous the circle technique is used to calculate the divergence of the experimental beam.

Figure 3.5a is a plot of the parameters s and w from a typical experimental radial emittance run. Figure 3.5b shows the same data plotted with α_r versus $r - r_0$ (deviations from the average radius are plotted to emphasize the width of the beam) i.e. an emittance plot. The r and α_r values at which current readings are taken show as a grid of (+) signs and dots. Overlaid on top of the data points are contours of

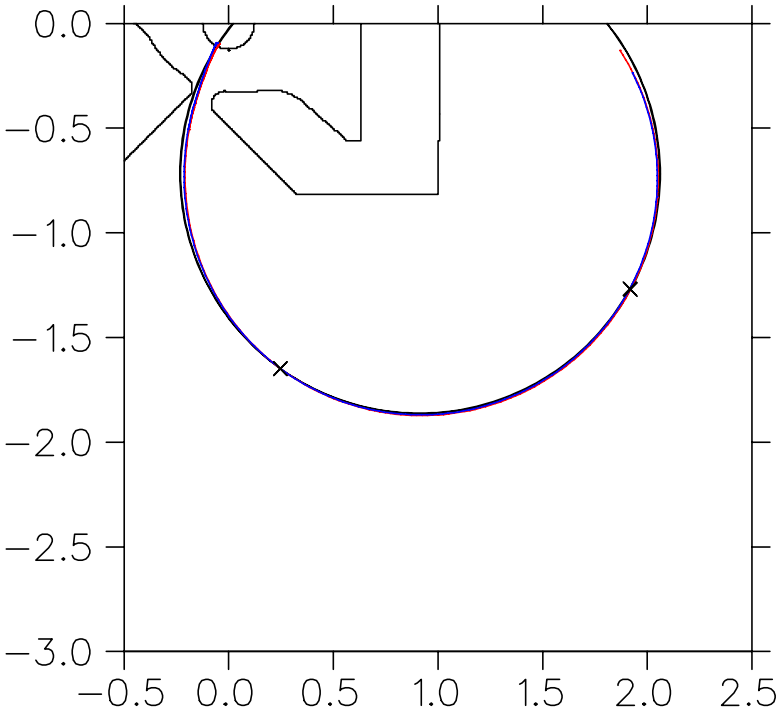

(a) Marked with "X's" are a single slit location and two wire locations separated by about 0.005" (0.13 mm). Two orbits were tracked with Z3CYCLONE (red and blue) both of which pass through the specified slit location and each of which end at their respective wire locations. Two circles (black) also pass through the specified slit location and end at the two specified wire locations.

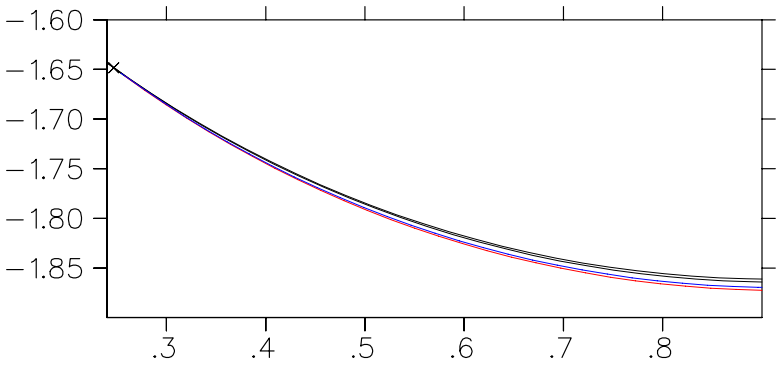

(b) A closeup of the region after the slit probe. It can be seen that while the circles (black) and the tracked orbits (blue and red) do not follow the exact same path from the slit to the wire, the divergence (angular spread) between the two circles is very close to the divergence between the two tracked rays.

Figure 3.4: Test Orbits for Calculating Divergence

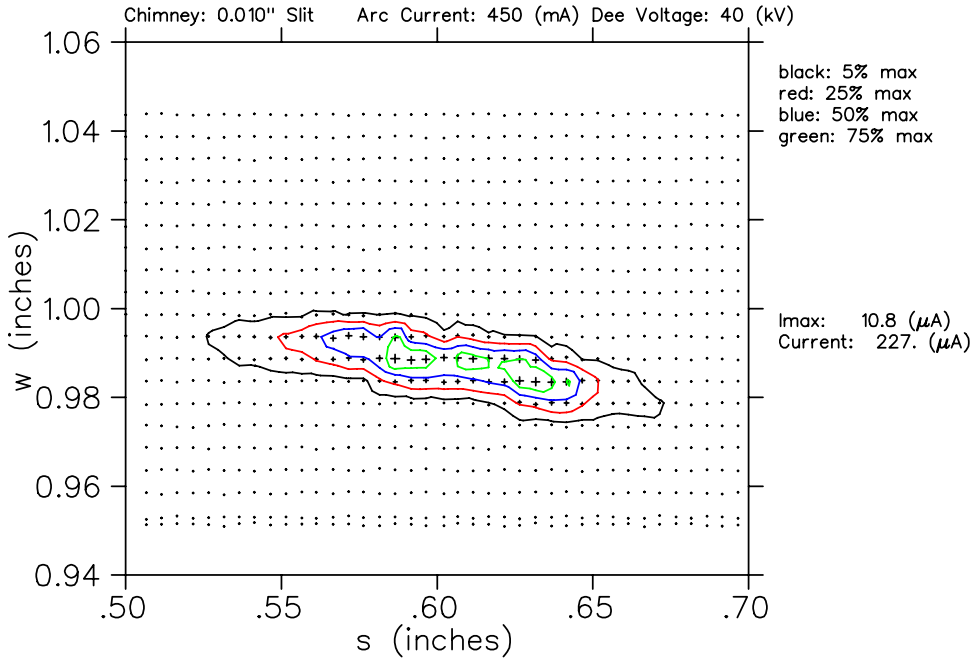

(a) (s, w) plot showing the slit and wire probe positions along with the current measured at each grid point.

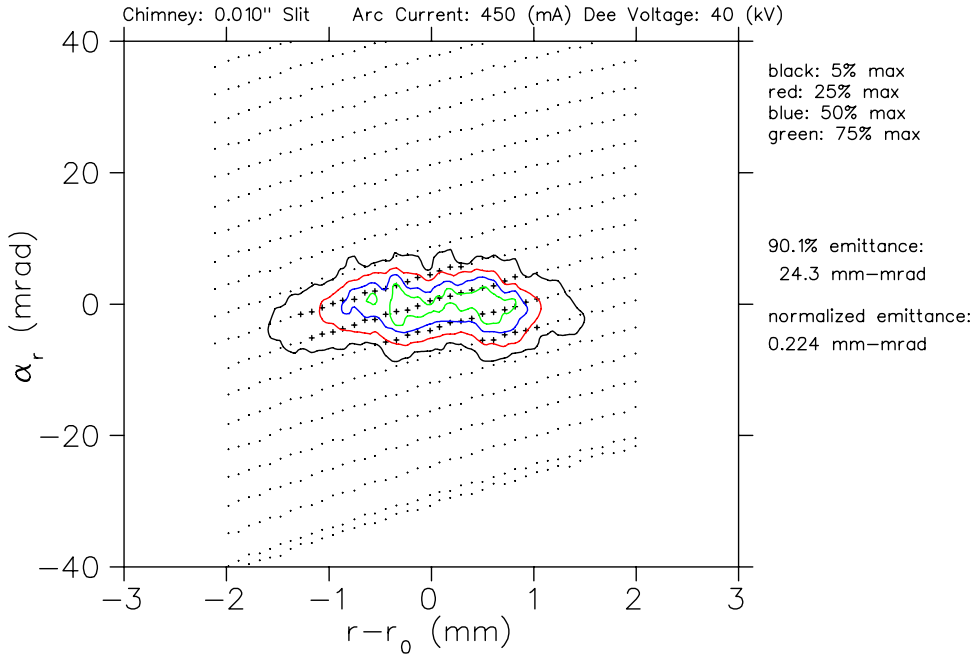

(b) The same data plotted in (r, α_r) space.

Figure 3.5: Converting Radial Slit and Wire Probe Position Data to r and α_r

constant wire current, these help to visualize the shape of the beam in emittance space. The points with the largest current density are plotted with + symbols; adding the current from each of these points gives approximately 90% of the total beam current. The rest of the data points are marked with dots. The area represented by the + symbols is the "90% emittance" of the beam and is recorded with each emittance plot. ("Normalized emittance," as discussed in section 1.2, is the emittance multiplied by the relatavistic factors β and γ.)

3.1.4 Converting Raw Data into Axial Emittance Plots

For axial emittance measurements, like radial measurements, the quantities measured by the equipment are the slit probe parameter (s), the wire probe parameter (w), the current on the slit probe (i_s) and the current on the wire (i_w). To extract the traditional axial emittance variables from the data, we make the assumption that the beam's z motion is not affected by the magnetic field. This is equivalent to assuming that the field has constant B_z over the entire orbit. (Tracked orbits in Z3CYCLONE show that this is a reasonable approximation for the region between the slit and wire probes.)

Calculating z and α_z is a two step process. First, determine z_{slit} and z_{wire} from the parameters s and w. (see Section 2.4.2). Second, calculate the divergence angle α_z as the arctangent of the change in z from the slit to the wire divided by the beam path length from the slit to the wire.

$$\alpha_z = \tan^{-1}\left(\frac{z_{wire} - z_{slit}}{pathlength}\right) \tag{3.1}$$

The z position variable is identified as the height of the beam as it crosses through the slit (z_{slit}). Figure 3.6 shows two graphs. The top graph is a plot of the parameters

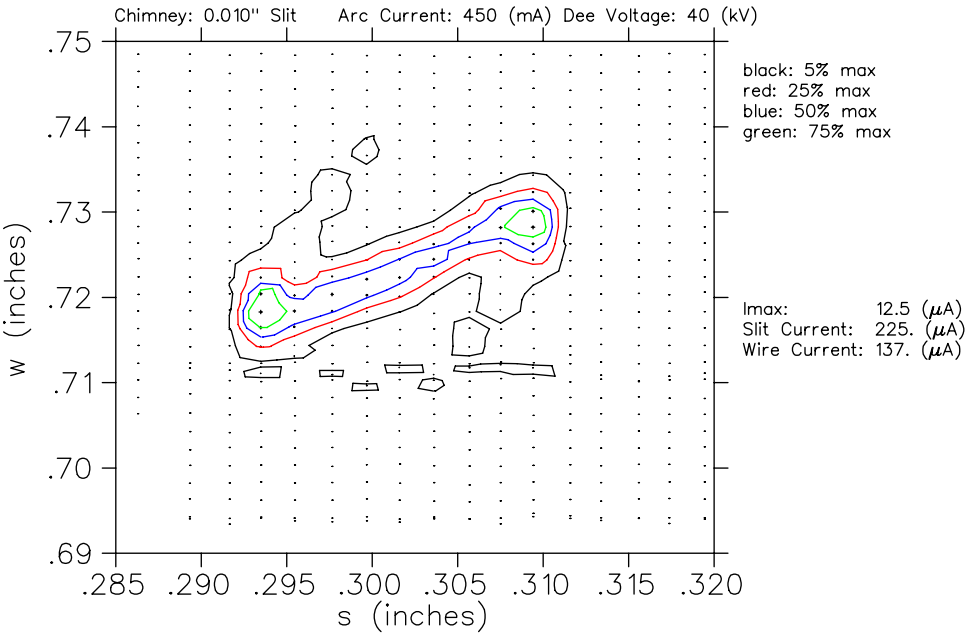

(a) (s, w) plot showing the slit and wire probe positions along with the current measured at each grid point.

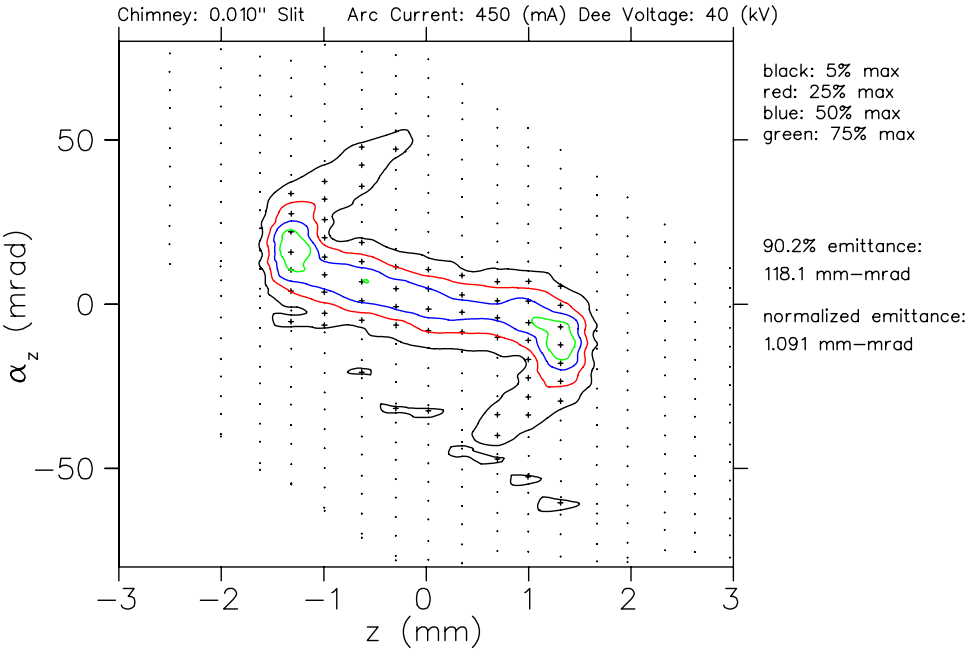

(b) The same data plotted in (z, α_z) space.

Figure 3.6: Converting Axial Slit and Wire Probe Position Data to z and α_z

s and w from a typical axial emittance run. The bottom plot shows the same data plotted versus the emittance variables z and α_z.

The grid and contours used in the axial emittance graphs have the same meaning as they do in the radial emittance graphs. The area enclosed by the + symbols is the 90% emittance of the beam. (The focusing tails observed at the top and bottom of the axial emittance area are similar to those observed by Mallory [6, p69] and are produced by the focusing electric field at the ends of the source slit.)

3.2 Experimental Results

3.2.1 Slit Chimney Measurements

One of the key factors determining the performance of an ion source is the shape and size of the output slit in the chimney. All data for this section (3.2.1) were collected with two slit chimneys which were made at the MSU physics department machine shop. (Similar chimneys made by ACCEL Instruments GmbH of Bergisch-Gladbach Germany for the 250 MeV proton cyclotron were tested later and are not included in this dissertation.)

Each chimney is made of molybdenum tubing, having outer diameter 0.250" (6.35 mm) and wall thickness 0.020" (0.51 mm). Both chimneys have a 0.196" (5.0 mm) tall chamfered slit. The difference between the two chimneys is the width of the slit; one chimney has an 0.010" (0.25 mm) wide slit while the other has an 0.020" (0.51 mm) wide slit. Perspective views of the two slits are shown in figure 3.7.

The puller geometry used in these tests was an original design for the ion source test stand (figure 3.8) with a 0.195" (5.0 mm) chimney–puller gap intended to hold 50 kV.

To directly compare the two slit chimneys we look at their performance at an arc

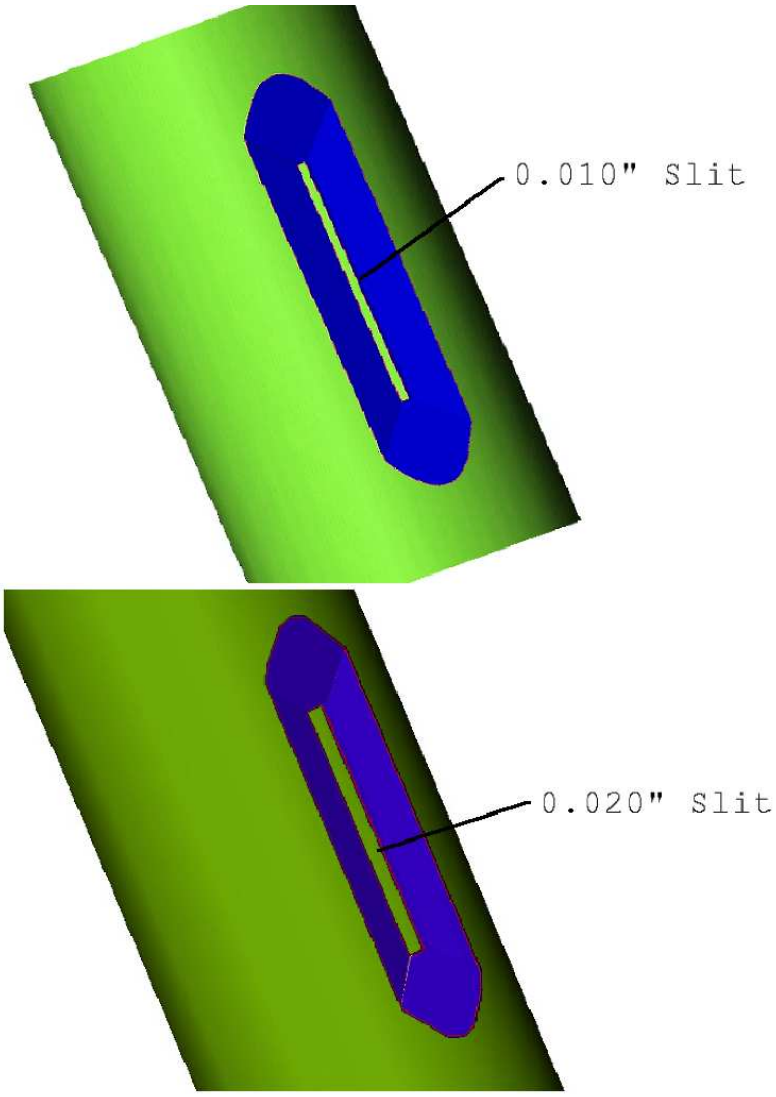

Figure 3.7: The two slit chimneys that were used are shown. One chimney has a 0.010" (0.254 mm) slit. The other has a 0.020" (0.508 mm) slit. Both have a 10° chamfer.

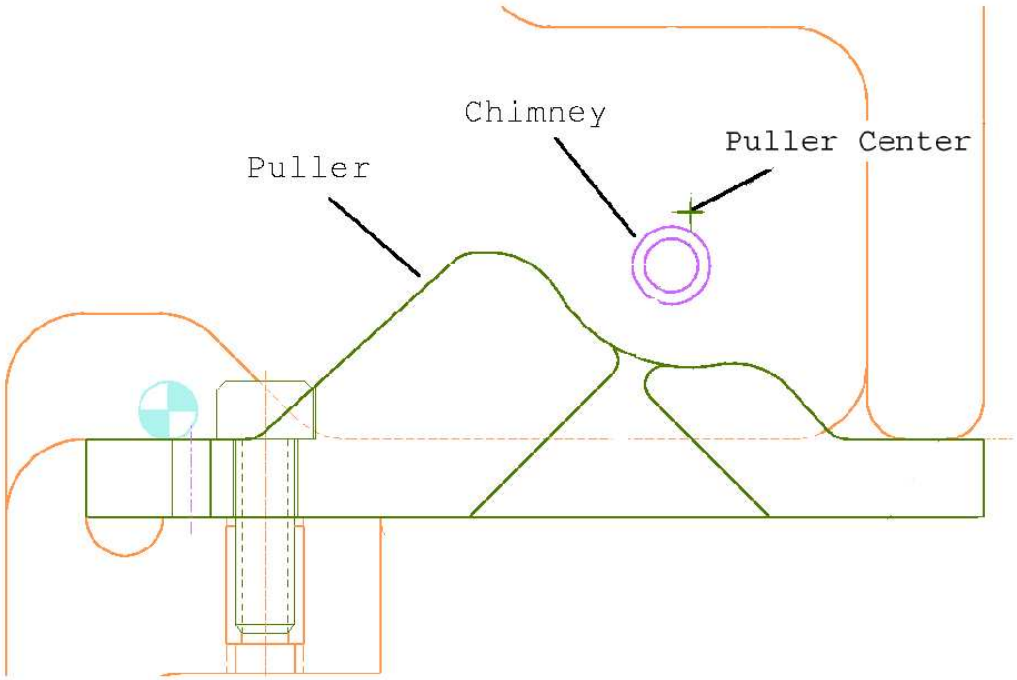

Figure 3.8: This puller was designed for the ion source test stand to hold 50 kV. The puller has a radius of curvature of 0.500" (12.7 mm) and is centered behind the chimney. The minimum source to puller gap is 0.196" (5.0 mm).

Chimney	90% Current (μA)	Radial Emittance (mm-mrad)	Axial Emittance (mm-mrad)	Luminosity ($\frac{A}{cm^2-sr}$)
0.010" Slit	44	27	112	1.5
0.020" Slit	203	47	191	2.3

Table 3.1: The chimney with the larger slit produces a beam with a larger emittance. However, the beam is also of higher intensity. The net effect is a higher luminosity for the chimney with the 0.020" (0.50 mm) slit. (Data sets in the table are taken with an arc current of 50 mA, gas flow of 3.0 cc/min and puller voltage of approximately 40 kV.)

current of 50 mA. (This low arc current would not typically be used during actual beam production, but is used here as the only arc current common to the data sets of the two chimneys.) The performance of the ion source with the 0.010" slit chimney at arc current settings ranging from 50 to 450 mA is discussed in section 3.2.3 and a summary of all data that have been collected is given in section 3.2.5.

Keeping all other source parameters constant emittance measurements were made with both chimneys. Figures 3.9 and 3.10 show emittance plots for the two chimneys. Table 3.1 lists the emittance and luminosity for the two chimneys. The chimney with a 0.020" (0.51 mm) slit has a larger emittance than the chimney with the 0.010" (.25 mm) slit, but it also produces a higher beam current. As discussed in sec 1.2, luminosity is defined as accelerated current divided by radial and axial emittance of the beam. The chimney with the 0.020" (0.51 mm) slit has a higher luminosity at this arc current.

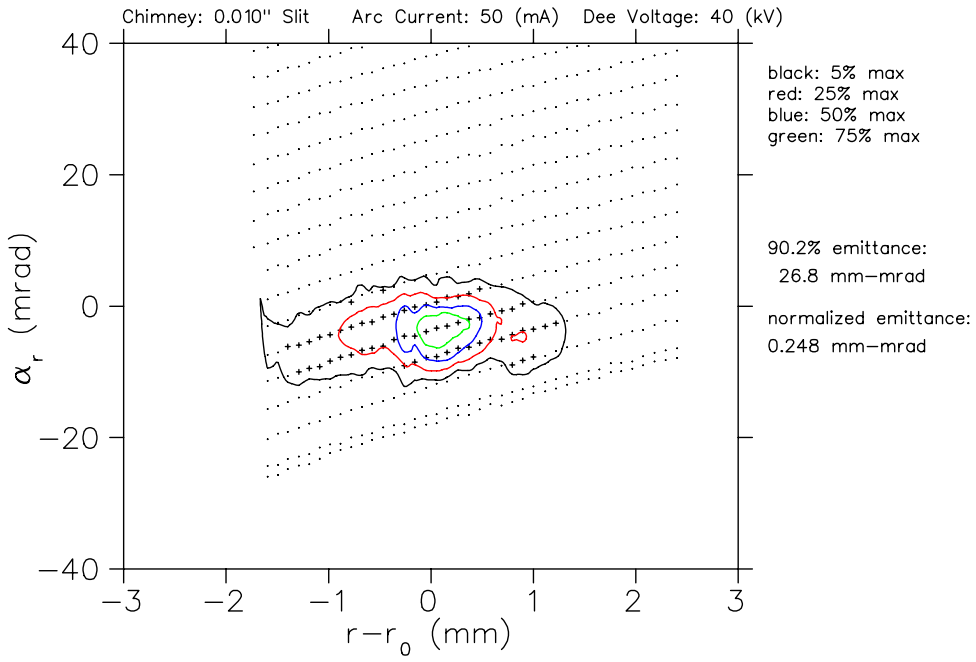

(a) 0.010” Slit Chimney Radial Emittance

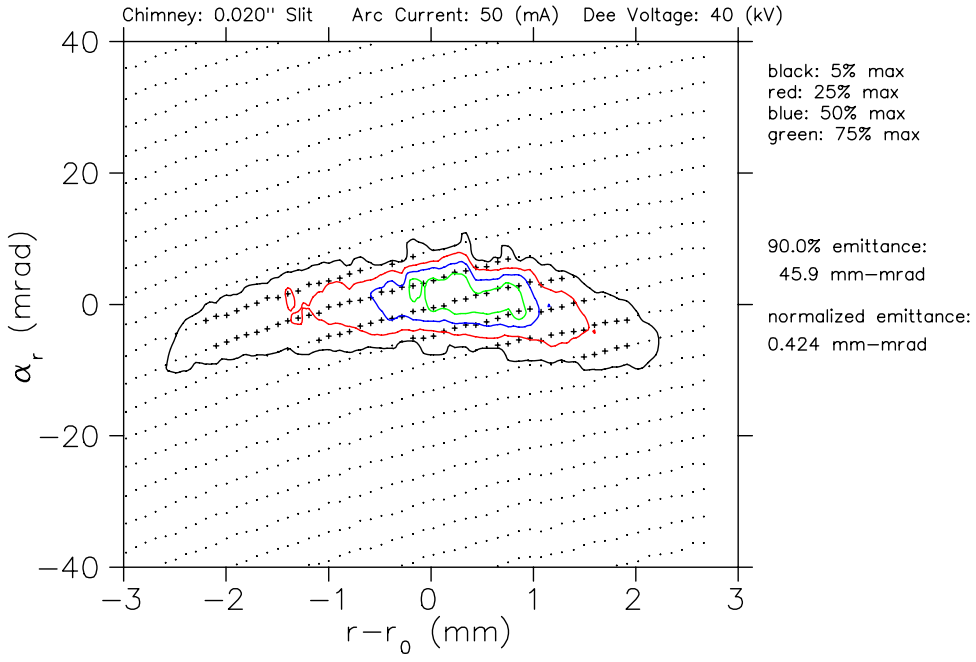

(b) 0.020” Slit Chimney Radial Emittance

Figure 3.9: The larger chimney slit produces a beam with a larger emittance in r.

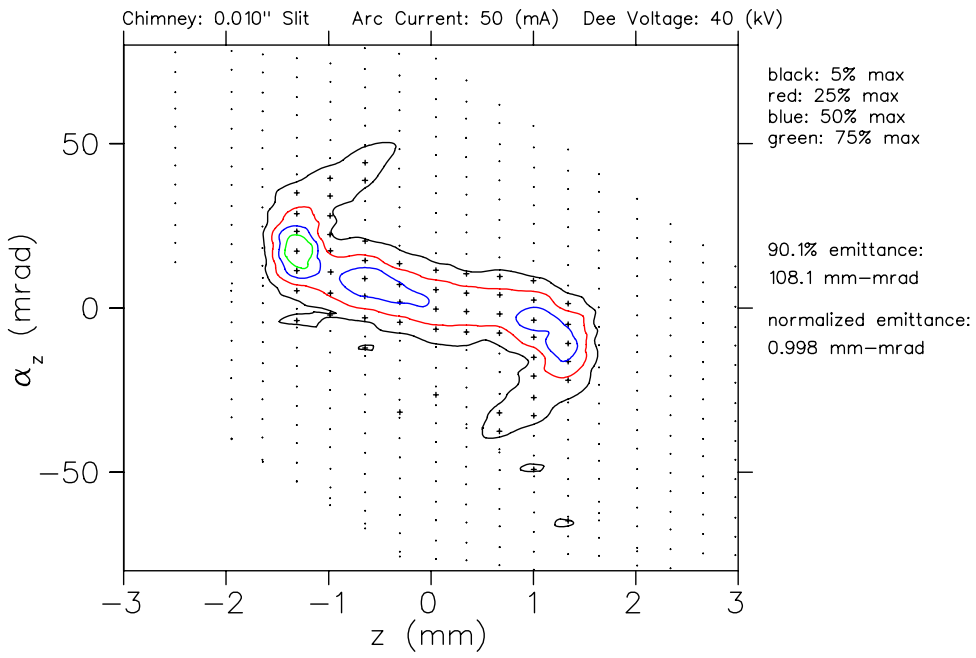

(a) 0.010” Chimney Axial Emittance

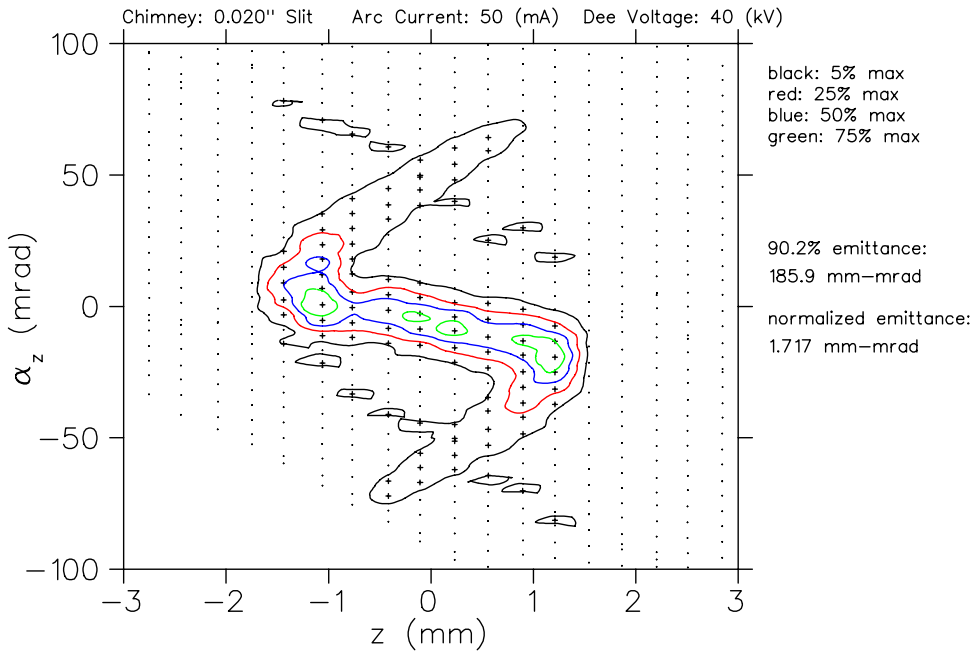

(b) 0.020” Chimney Axial Emittance

Figure 3.10: The larger chimney slit produces a beam with a larger emittance in z.

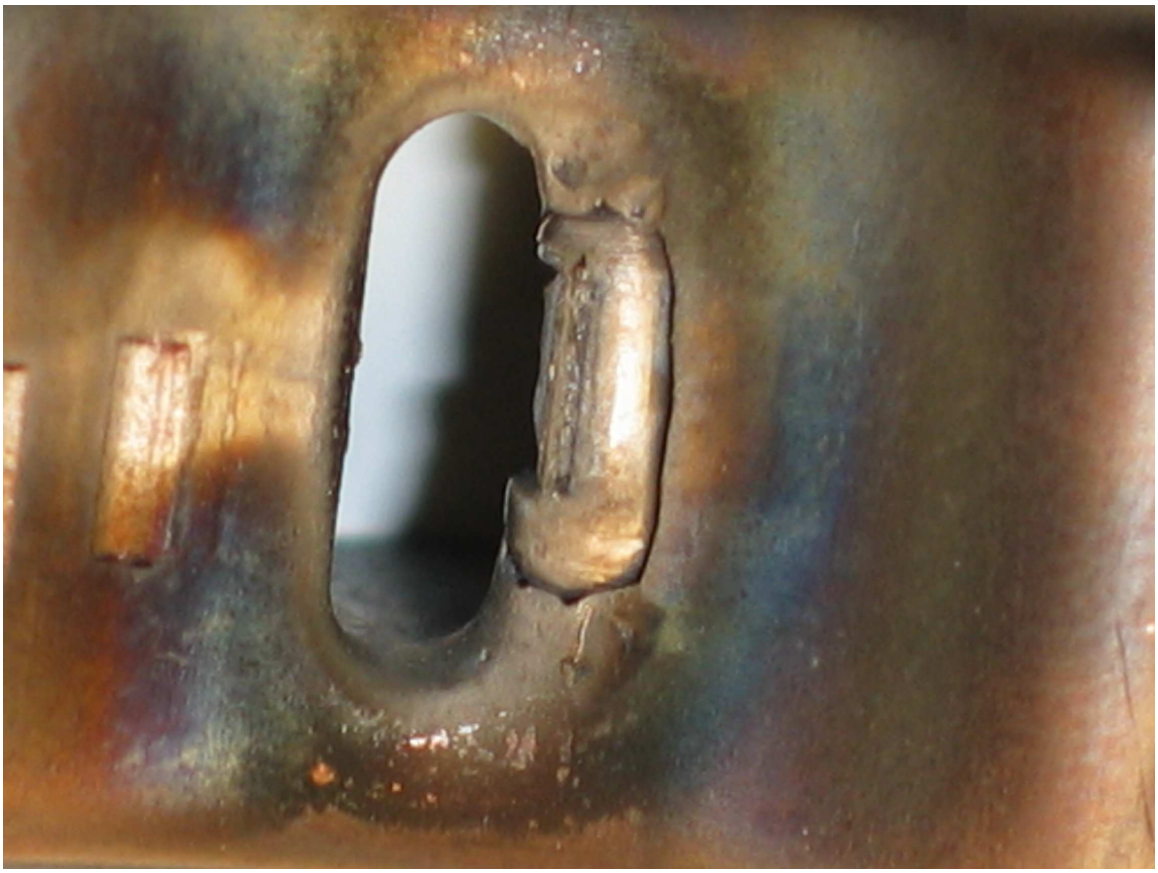

Figure 3.11: Puller Markings

Puller Markings

In Spring of 2004 the ion source was run in the test stand continuously for several months in order to test the lifetime of the cathodes (which did not quit working during that test). The ion beam which was aimed slightly to the right in the puller opening cut away at the tungsten insert in the puller (figure 3.11). The cut tells us a couple of things about the beam. First, the height of the cut is about 0.15" (3.7 mm) which is consistant with the height of the beam measured at the slit probe inside the dee and noticeably smaller than the 0.196" (5.0 mm) height of the source opening. Second, the notches at the top and bottom of the cut indicate that the top and bottom of the beam are wider than the center of the beam. This is likely the result of the interaction of the beam with the non-linear electric fields near the top

and bottom of the source opening.

3.2.2 Hole Source Measurements

A second set of experiments was performed with a chimney and puller region modeled after the central region of the Harper Medical Cyclotron in Detroit MI. Because the K100 uses a deuteron beam the emittance measurements for the "hole" chimney were taken with deuterons accelerated to a nominal dee voltage of 20 kV (as opposed to protons at a nominal dee voltage of 40 kV for the slit chimneys).

As seen in figure 3.12, the opening in the chimney has a 0.047" (1.19 mm) hole with a chamfer that is machined by using a center hole drill to create a sharp edge at the base of the hole. The puller is shown in figure 3.13.

The beam extracted from the hole chimney is significantly different from the beams extracted from the slit chimneys. The radial emittance shows significant curvature (figure 3.14a) and the axial emittance (figure 3.14b) shows that the beam is diverging by the time it reaches the slit probe (in contrast with the beam from the slit chimneys which is converging when it reaches the slit probe) with particles above the center of the beam moving up, and particles below the center of the beam moving down. (Our probes were not able to measure the full height of the beam.) The emittance of the beam from the hole chimney was larger than the emittance from either of the slit chimneys. Because, the ions extracted from the hole chimney were only accelerated to 20 keV (as compared to 40 keV for the ions from the slit sources) it is appropriate to compare the normalized emittances. The radial normalized emittance (0.66 mm-mrad) was about 50% larger than that of the slit chimney (.44 mm-mrad) and the axial emittance was larger than could be measured. More than half of the beam which came through the puller was not measured by the wire probe. It is likely that the beam grew in z until part of the beam was blocked by the top and bottom of the dee.

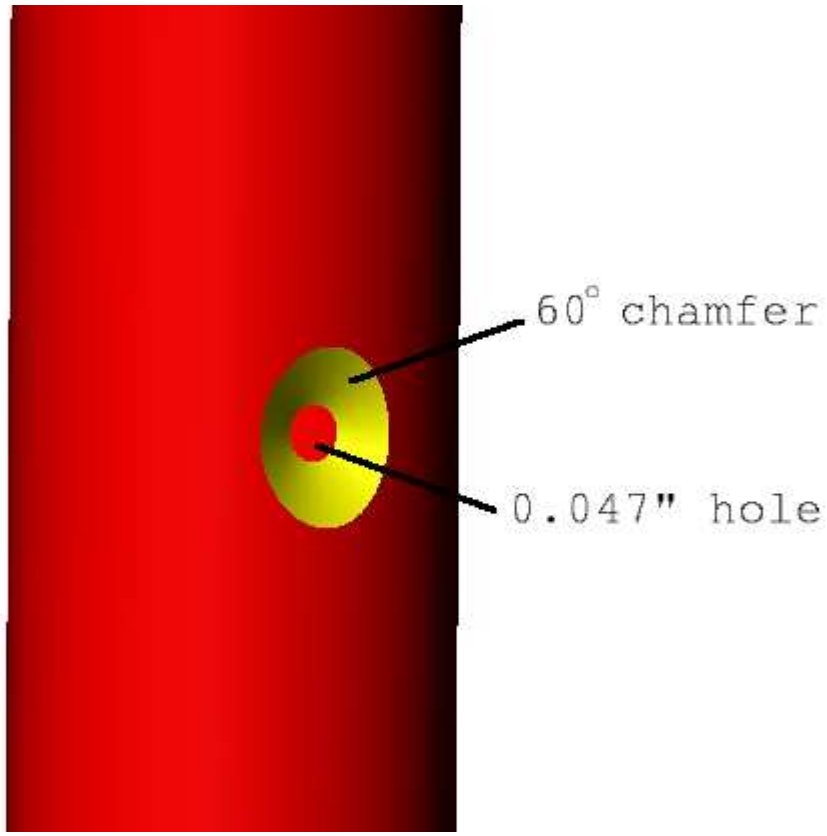

Figure 3.12: The hole in the chimney is 0.047" (1.19 mm) with a sixty degree chamfer.

At 50 mA of arc current, the normalized luminosity of the beam which made it to the wire probe was 129 $\frac{A}{mm^2-sr}$, about half of that for the slit chimney with the same arc current (264 $\frac{A}{mm^2-sr}$). It is relevant to note that with its internal target the Harper Medical Cyclotron's performance is not presently limited by beam quality or beam current, so there is no pressing need to improve the luminosity in the cyclotron's ion source. Also, with a 250 mA arc current, the hole chimney has higher luminosity than the 0.010" slit chimney at the same arc current (the 0.020" slit chimney was not run at arc currents above 150 mA).

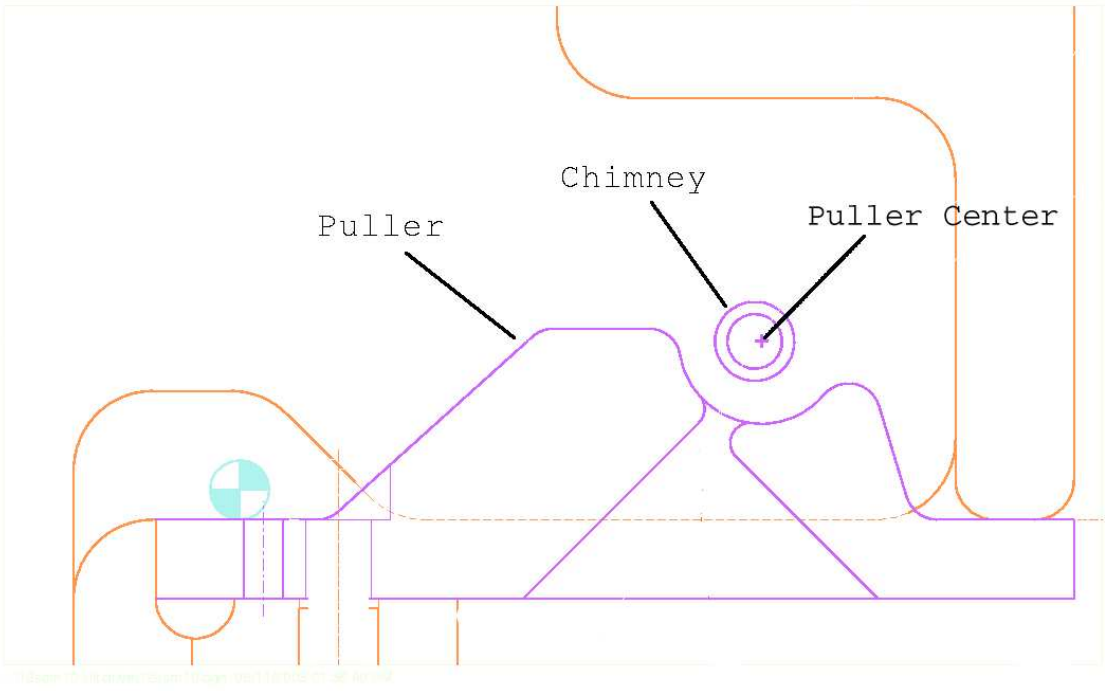

Figure 3.13: This puller was designed for the ion source test stand and has the same geometry as the puller in the K100 medical cyclotron. The chimney is not centered in the puller. (The chimney is centered at (0.000,0.000) and the puller is centered at (0.021,0.000).) The minimum gap between the chimney and the puller is 2.9 mm while the gap at the source opening is 3.0 mm, meaning that the beam does not see the peak electric field. This is not optimal for extracting the maximum beam current, but the layout has worked well in the K100 cyclotron. This puller will hold about 25 kV in the ion source test stand.

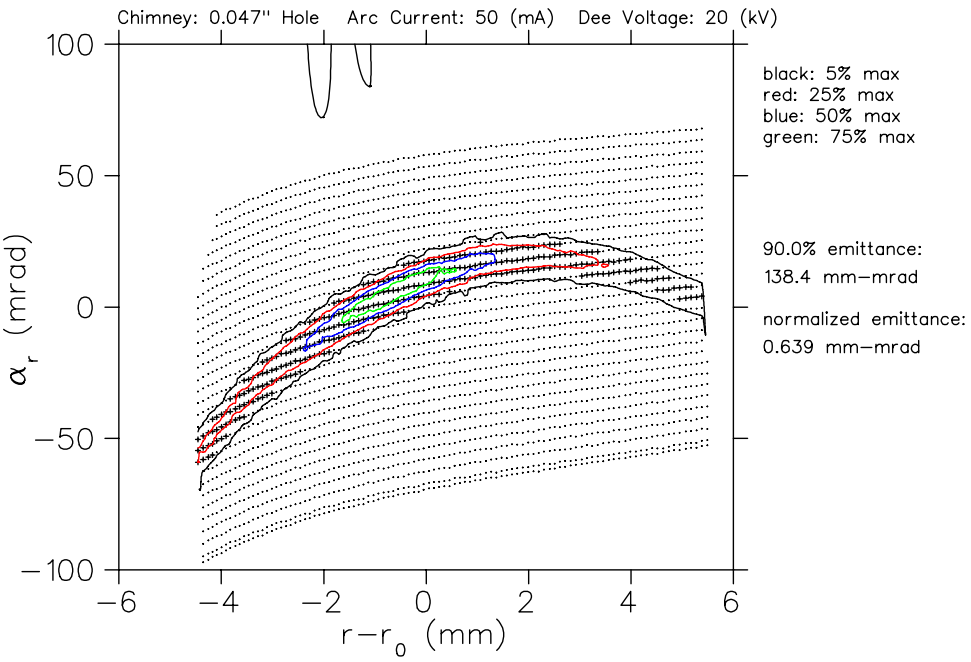

(a) Radial Emittance

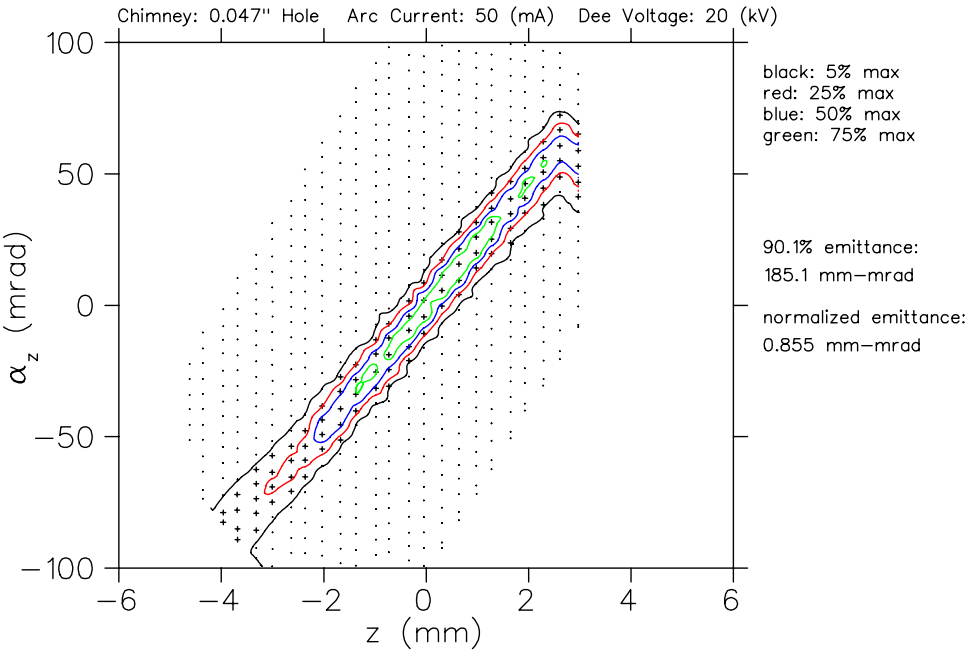

(b) Axial Emittance

Figure 3.14: Emittance Plots with the Hole Chimney

3.2.3 Effect of Arc Current

Experience with PIG ion sources has shown that a larger arc current can produce a more intense beam. This was verified using the slit chimneys. Measurements were taken with arc currents ranging from 50 mA to 450 mA for the 0.010" slit and from 50 mA to 150 mA for the 0.020" slit. (Higher arc currents were not used for the 0.020" slit chimney due to concerns about damaging the slit probe with higher beam currents i.e. above 600 μA.) The hydrogen gas flow was 3.0 cc/min for all runs. Table 3.2 and 3.3 show the general trend of increasing arc current producing increased beam current as expected. For the 0.010" slit, there was no noticeable change in the emittance of the beam for different currents, and it does not appear that space charge (the mutual repulsion experienced by the positive ions in the beam) was a significant factor at beam currents below 230 μA. For the 0.020" slit, both the radial and axial emittance grow with increasing current. The growth in emittance could be an indication that the shape of the plasma boundary changes with arc current or that increasing space charge forces are causing emittance growth.

Arc Current (mA)	Beam Current (μA)	Beam Current / Arc Current ($\times 10^{-3}$)	Radial Emitt. (mm-mrad)	Axial Emitt. (mm-mrad)	Luminosity ($\frac{A}{cm^2-sr}$)
50	52	1.0	27.2	112	1.7
250	165	0.66	25.5	141	4.6
350	195	0.56	23.5	121	6.9
450	227	0.50	25.0	127	7.1

Table 3.2: Results from four measurements of radial and axial emittance with the 0.010 inch slit chimney. The puller voltage was 40kV. All parameters were kept constant except the arc current.

Arc Current (mA)	Beam Current (μA)	Beam Current / Arc Current ($\times 10^{-3}$)	Radial Emitt. (mm-mrad)	Axial Emitt. (mm-mrad)	Luminosity ($\frac{A}{cm^2-sr}$)
50	230	4.6	47.1	191	2.6
100	401	4.0	57.9	206	3.4
150	590	3.9	64.9	239	3.8

Table 3.3: Results from three measurements of radial and axial emittance with the 0.020 inch slit chimney. The puller voltage was 40kV. All parameters were kept constant except the arc current.

3.2.4 Atomic Hydrogen Ions

Livingston and Jones report [5, Fig 9] that for a filament ion source, production of the atomic ions H_2^+ and H_3^+ was dependant on ion source arc current with atomic ion production decreasing with increasing arc current. A possible error in the results reported in this dissertation then arises from the possibility that atomic ions might contribute to the currents measured in the NSCL test system. Figure 3.15, for example, shows calculated orbits in the ion source test stand for protons and H_2^+ ions along with the setup used to observe protons and H_2^+ ions simultaneously. The slit probe did not have the range to cover the whole proton beam and H_2^+ beam at the same time, so we were unable to make quantitative measurement of the ratio of protons to H_2^+ ions.

Under normal ion source opperating conditions, (arc currents ranging from 50 to 350 mA, arc voltages less than 3 kV i.e. the power supply was current limited, and hydrogen gas flow rates greater than 2.0 cc/min) no H_2^+ ions were observed. We were able to observe H_2^+ ions by lowering the gas supply to 0.5 cc/min. At this setting, the arc shifted to the 3.5 kV limited mode of the arc power supply and the arc current dropped to 90 mA in a fast step. Since none of the results reported here used such a low gas flow, we conclude that the proton beam results given in this dissertation do not include atomic ion effects.

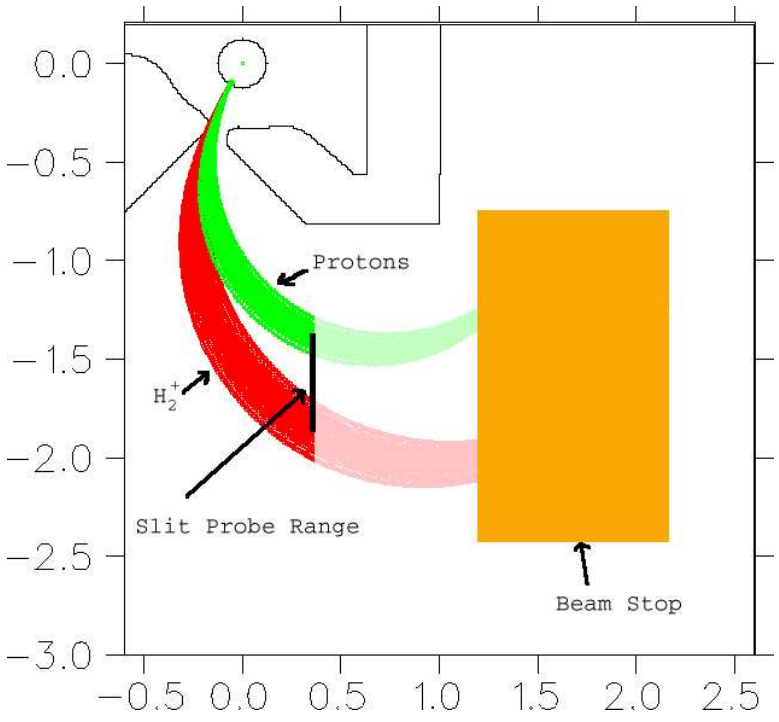

Figure 3.15: Plot shows calculated trajectories for protons and atomic hydrogen ions. Parts of each of these beams pass through the range of slit positions selectable in the Ion Source Test Stand. Using this setup, we were able to determine that atomic hydrogen ions were not produced from the cold cathode PIG ion source under normal operating conditions.

3.2.5 Data Summary

The following runs were made with results as listed. (See figures 3.16, 3.17, ... 3.24.)

Chimney	Dee Voltage (kV)	Arc Current (mA)	Gas Flow (cc/min)	Beam Current (μA)	Rad. Emit. (Normalized) (mm-mrad)	Axial Emit. (Normalized) (mm-mrad)	Luminosity (Normalized) $(\frac{A}{cm^2-sr})/(\frac{A}{mm^2-sr})$
Slit 0.010"	40	50	3.0	52	27.2 (0.252)	112 (1.03)	1.7 (170)
(MSU)	40	250	3.0	165	25.5 (0.235)	141 (1.30)	4.6 (380)
	40	350	3.0	195	23.5 (0.217)	121 (1.12)	6.9 (518)
	40	450	3.0	227	25.0 (0.231)	127 (1.17)	7.1 (525)
Slit 0.020"	40	50	3.0	230	47.1 (.435)	191 (1.77)	2.6 (236)
(MSU)	40	100	3.0	401	57.9 (.535)	206 (1.90)	3.4 (325)
	40	150	3.0	590	64.9 (.599)	239 (2.21)	3.8 (323)
Hole 0.047"	20	50	1.5	260	$>$ 143 (.662)	$>$ 195 (0.900)	n/a
	20	250	2.5	720	$>$ 115 (.534)	$>$ 213 (0.983)	n/a

Table 3.4: Data Summary

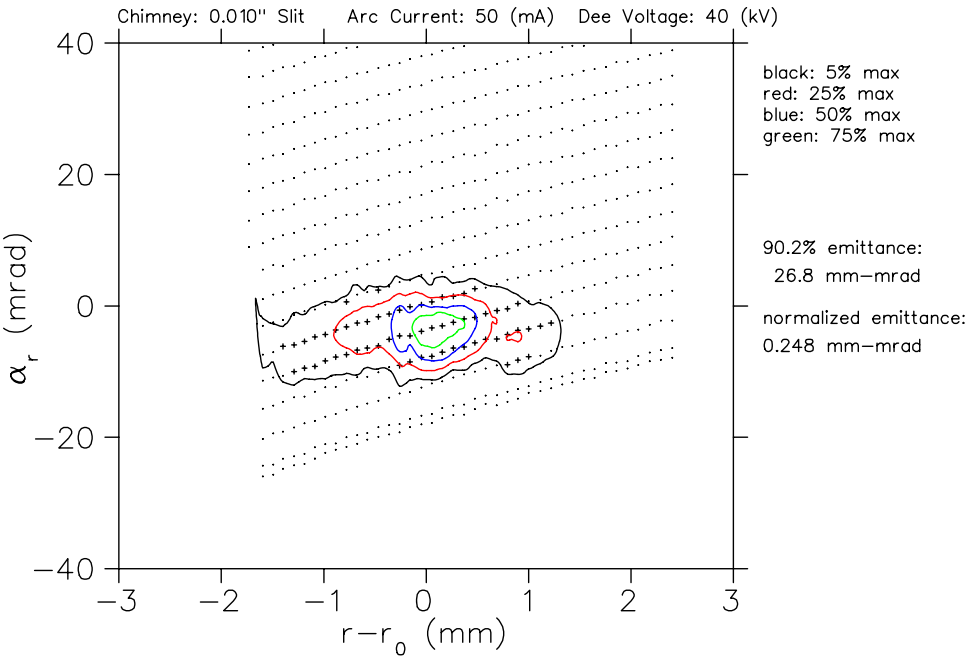

(a) Radial Emittance

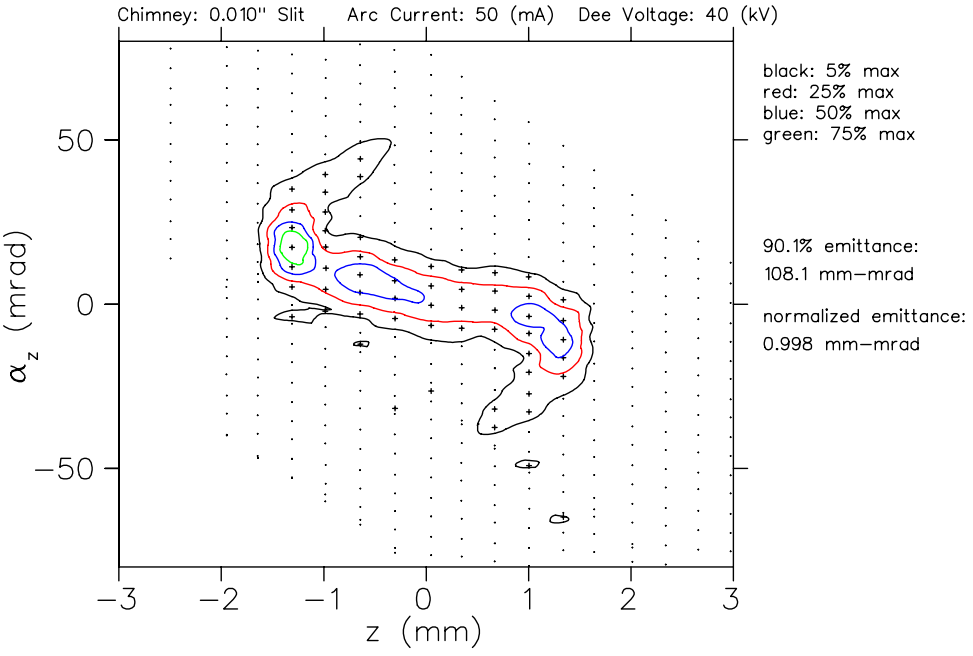

(b) Axial Emittance

Figure 3.16: Emittance Plots for 0.010" Slit Chimney with 50 mA Arc Current (Shown previously in figures 3.9 and 3.10.)

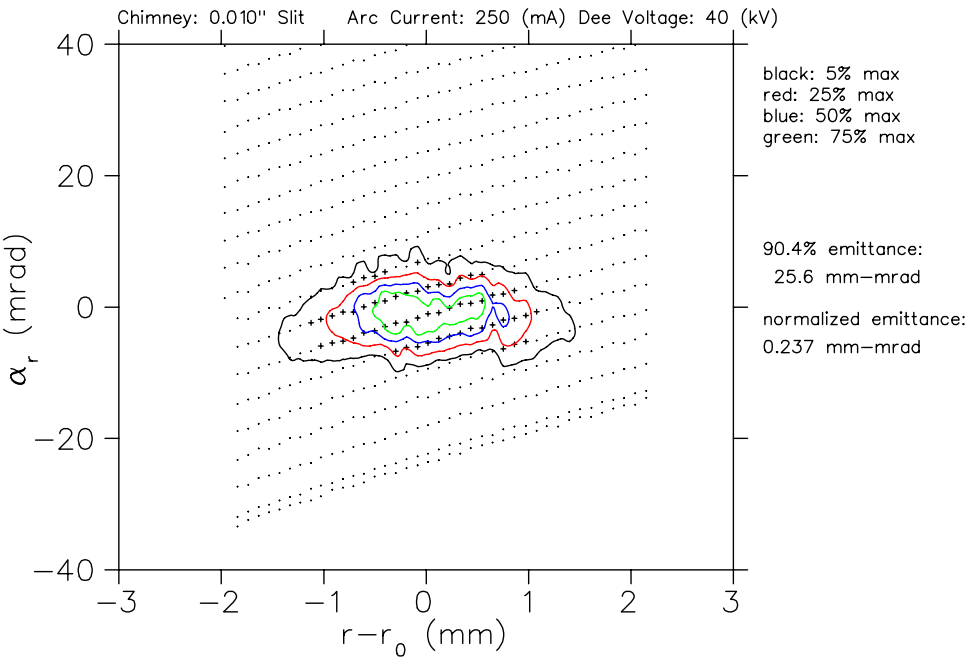

(a) Radial Emittance

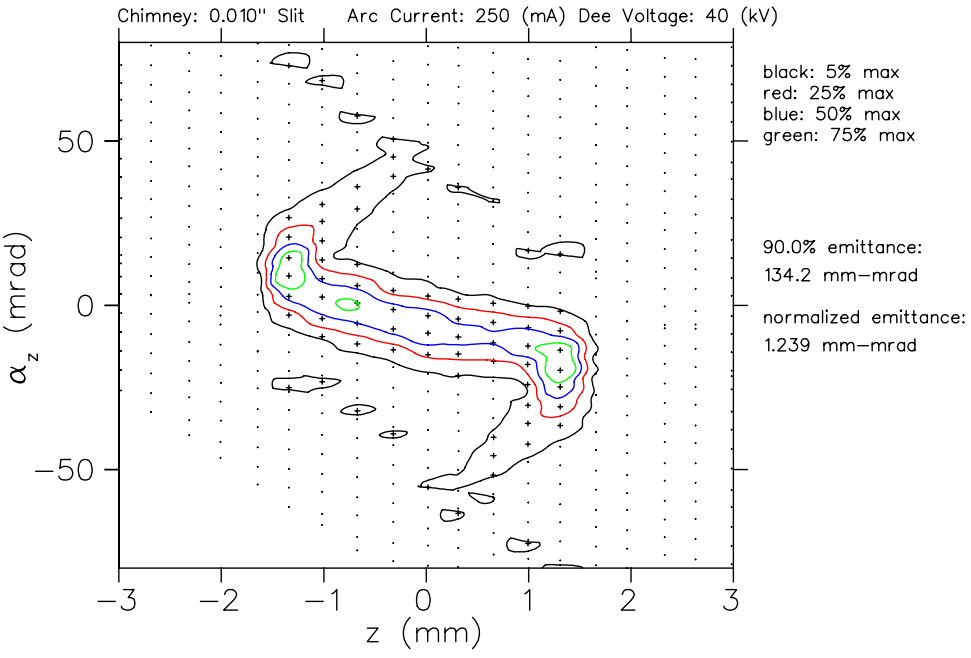

(b) Axial Emittance

Figure 3.17: Emittance Plots for 0.010” Slit Chimney with 250 mA Arc Current

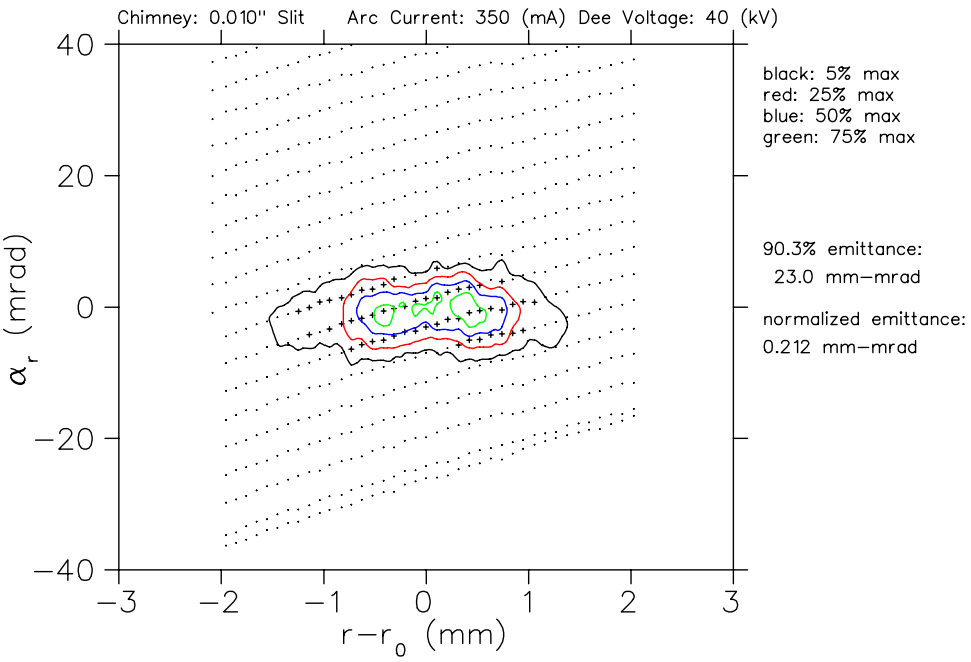

(a) Radial Emittance

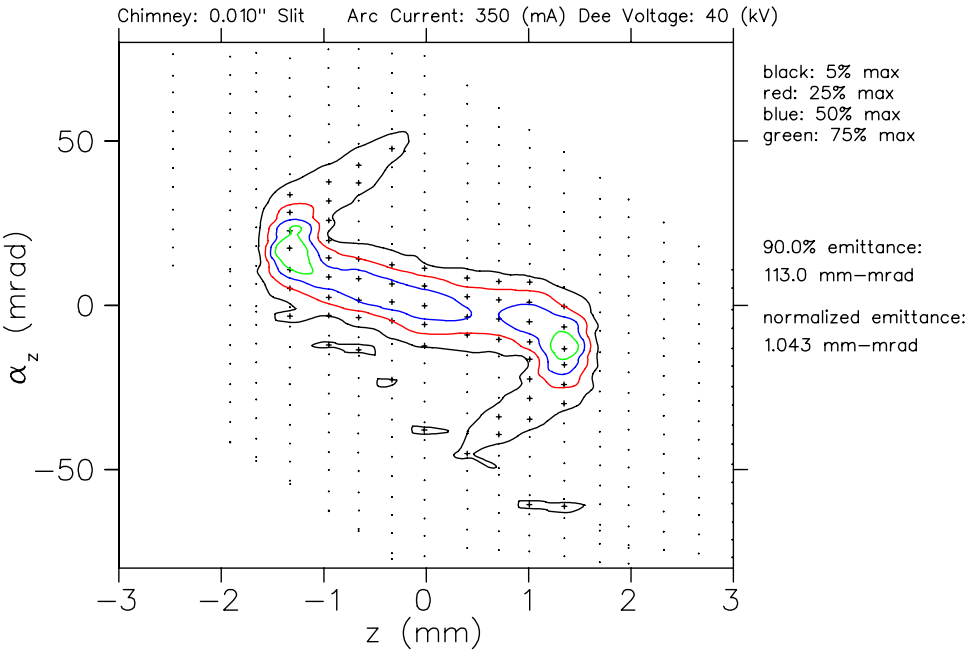

(b) Axial Emittance

Figure 3.18: Emittance Plots for 0.010” Slit Chimney with 350 mA Arc Current

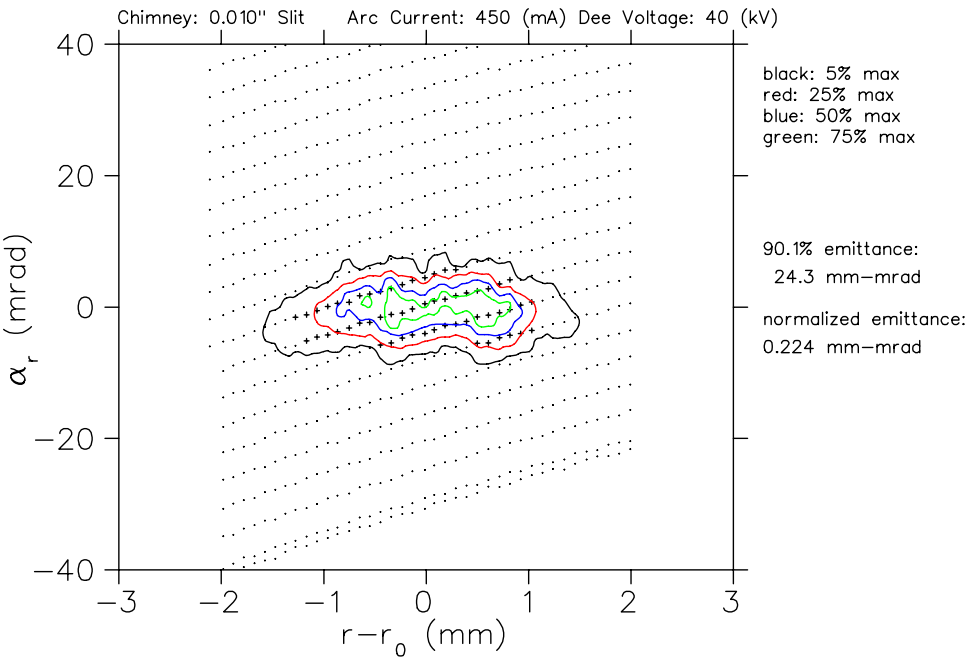

(a) Radial Emittance

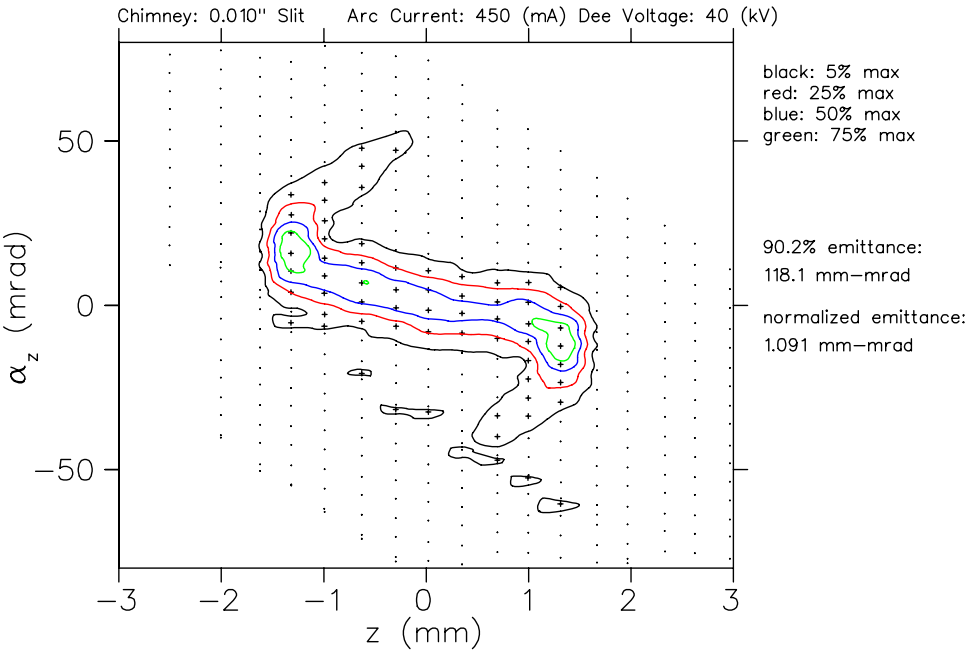

(b) Axial Emittance

Figure 3.19: Emittance Plots for 0.010” Slit Chimney with 450 mA Arc Current

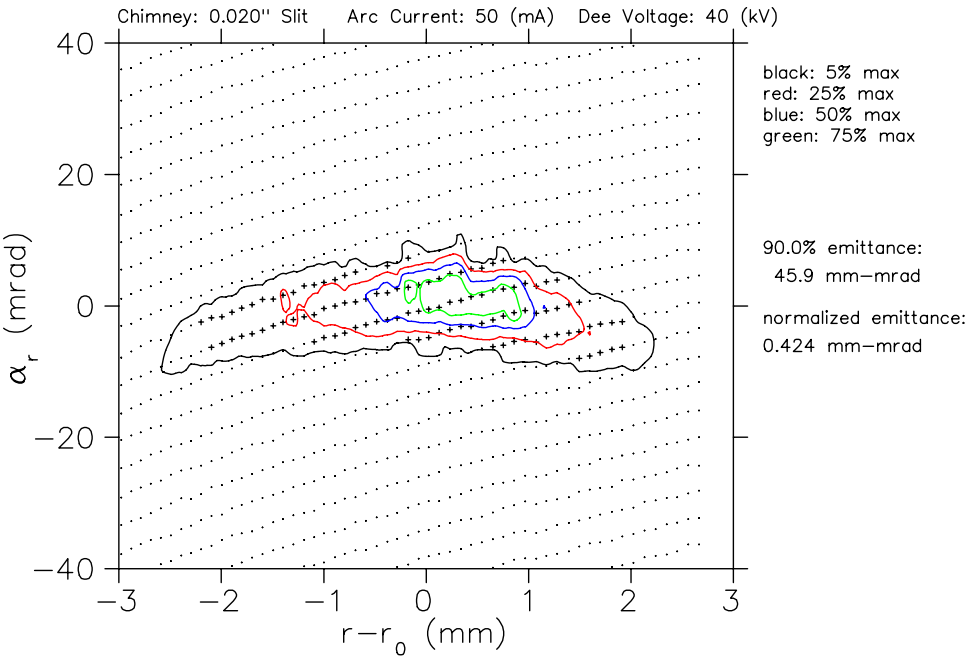

(a) Radial Emittance

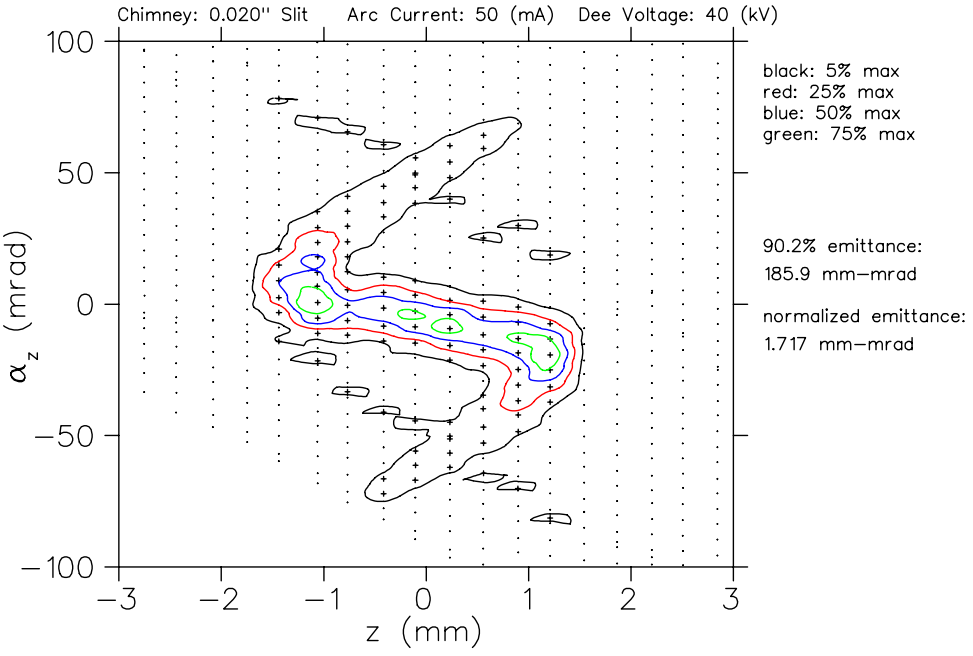

(b) Axial Emittance

Figure 3.20: Emittance Plots for 0.020" Slit Chimney with 50 mA Arc Current (Shown previously in figures 3.9 and 3.10.)

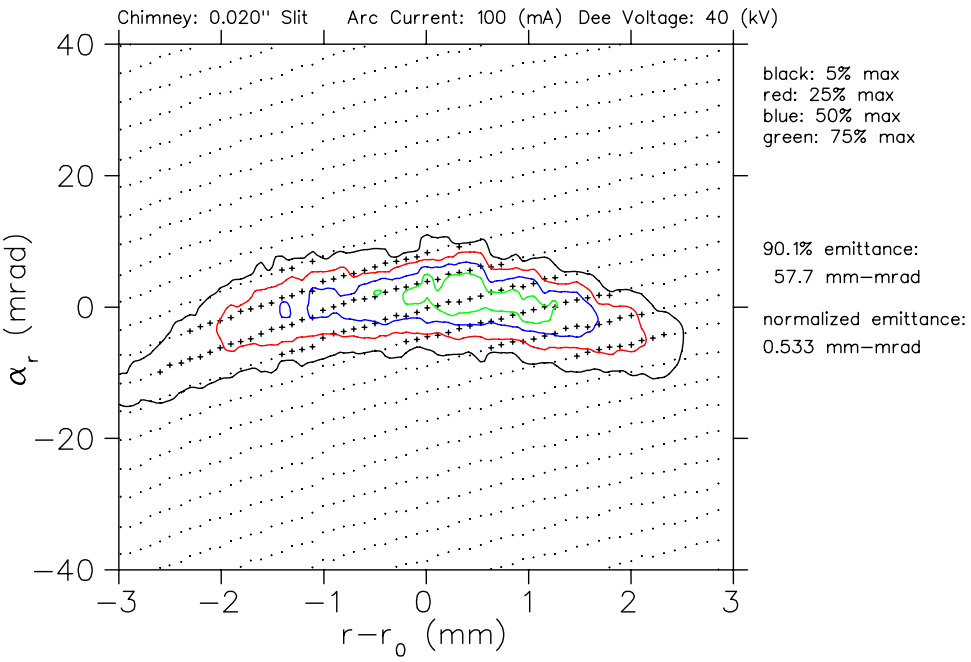

(a) Radial Emittance

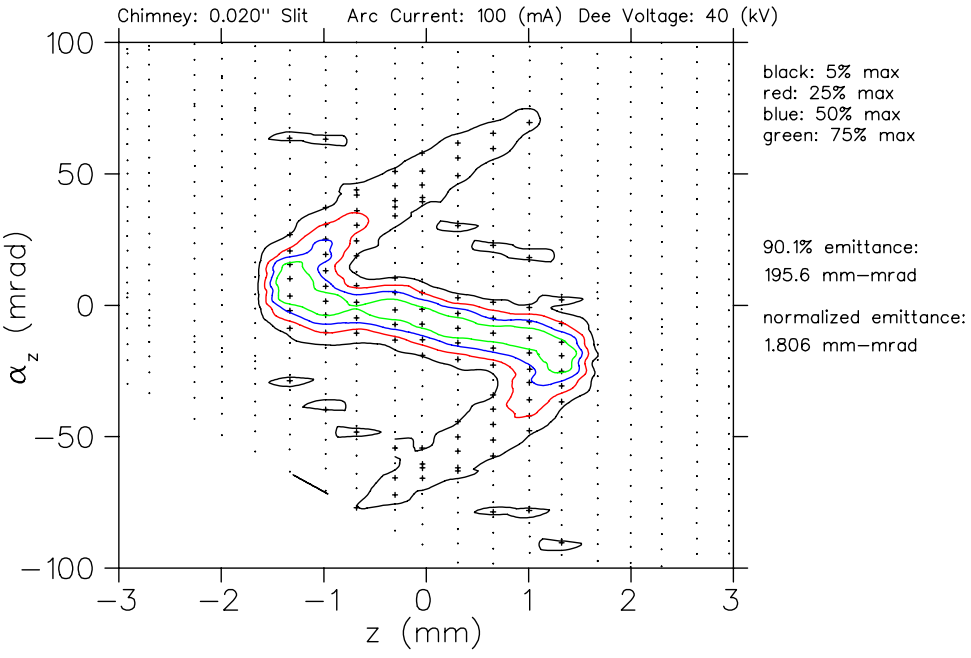

(b) Axial Emittance

Figure 3.21: Emittance Plots for 0.020" Slit Chimney with 100 mA Arc Current

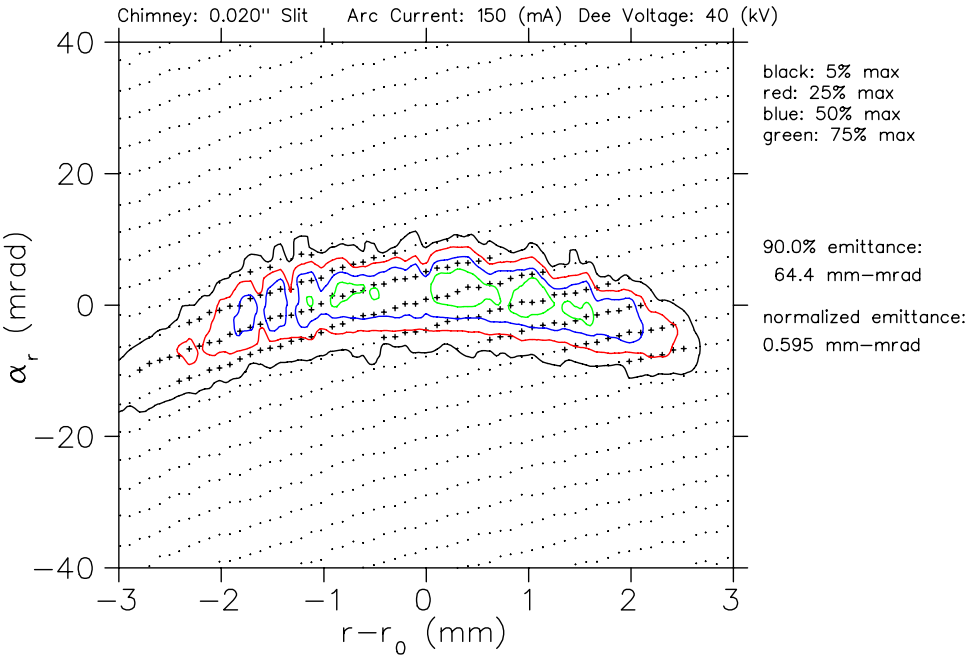

(a) Radial Emittance

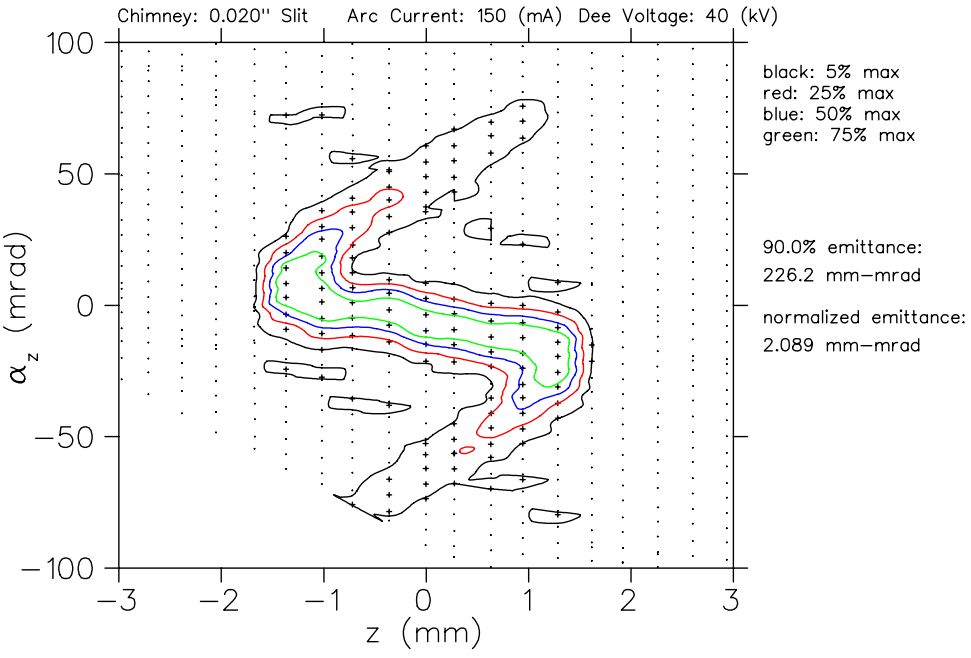

(b) Axial Emittance

Figure 3.22: Emittance Plots for 0.020” Slit Chimney with 150 mA Arc Current

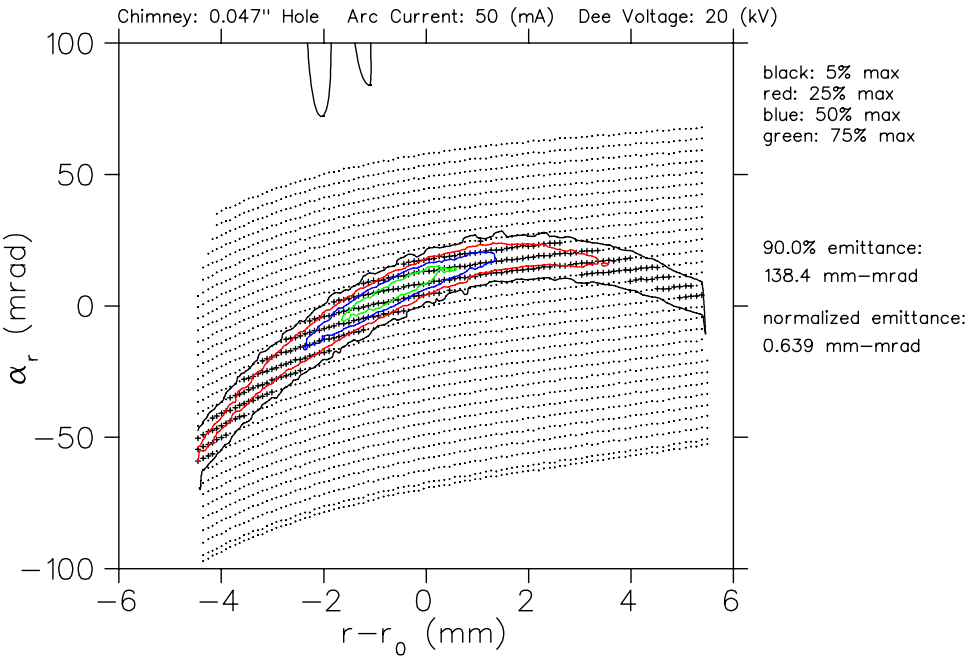

(a) Radial Emittance

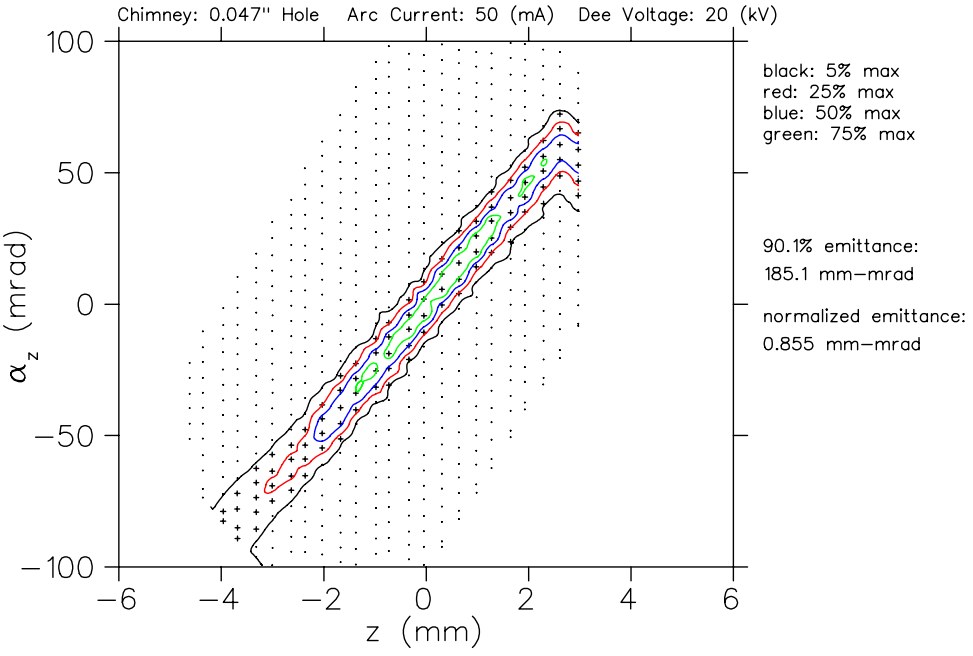

(b) Axial Emittance

Figure 3.23: Emittance Plots for Hole Chimney with 50 mA Arc Current (Shown previously in figures 3.14.)

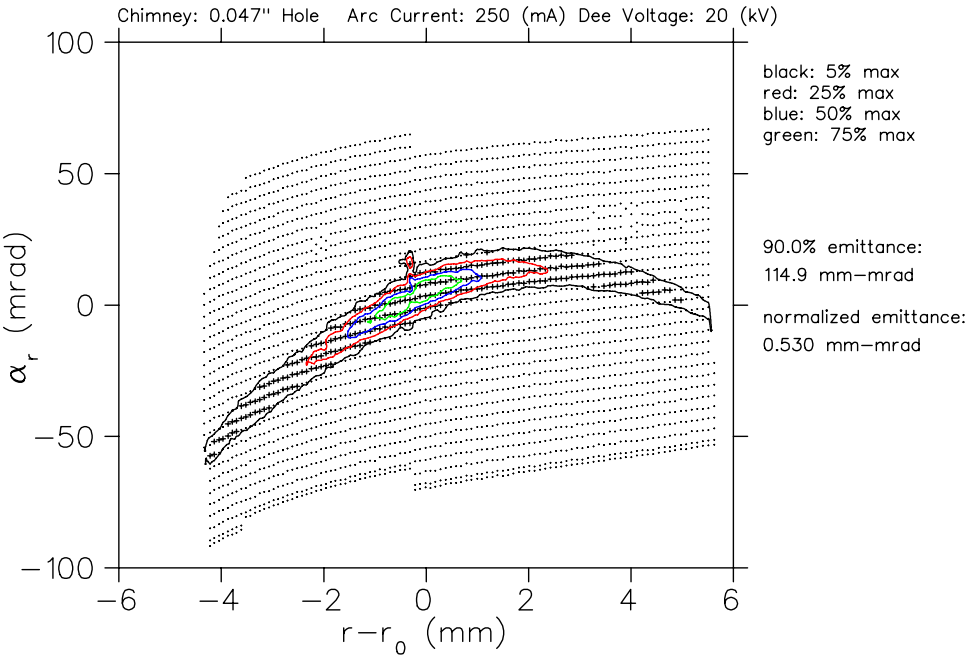

(a) Radial Emittance

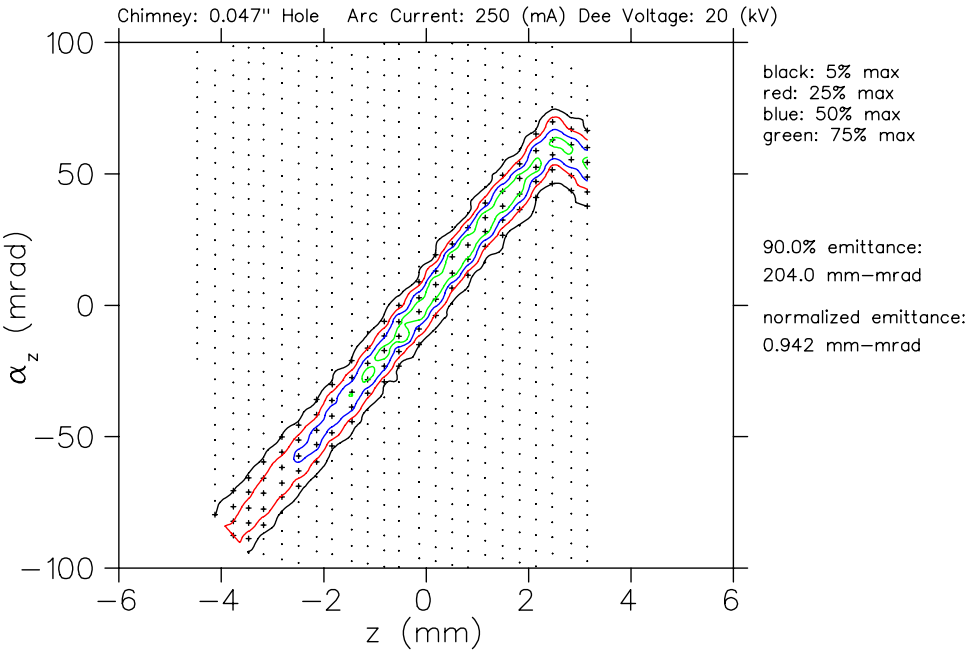

(b) Axial Emittance

Figure 3.24: Emittance Plots for Hole Chimney with 250 mA Arc Current

3.3 Matching Ensembles of Computed Orbits to the Experimental Beams

For all comparisons between computed orbits and experimental data, graphs will show the experimental data as contours on top of a grid of black + signs and computed data as a collection of blue dots.

3.3.1 Slit Sources

Trajectories of 394,940 rays were computed for each calculation presented in this section (3.3.1). There are, first of all, 403 different starting positions for the ions on the zero potential surface across the chimney opening (13 across the width of the opening and 31 vertically). 49 different starting angles were tracked from each starting position 7 angles in the median plane (covering 103 degrees), 7 different starting angles vertically (covering 103 degrees). For each combination of starting position and starting angle 20 different rays were tracked, namely: five different starting energies representing a plasma temperature of 35000 K (resulting in a maximum starting energy of 11.7 eV) and 4 different accelerating potentials (36.5±0.060 kV for the 0.020" slit and 37.25±0.060 kV for the 0.010" slit) [2]. Orbits which came into contact with the chimney before exiting the chimney opening were dropped as were orbits which hit the puller.

[2]Experimentally, the accelerating potential is read with an analog gauge which is accurate to ± 0.5 kV. The accelerating potential used in the calculations, which are sensitive to changes as small as 0.02 kV, is the one which produces the best fit to the experimental data and is always within the uncertainty in the experimental accelerating potential.

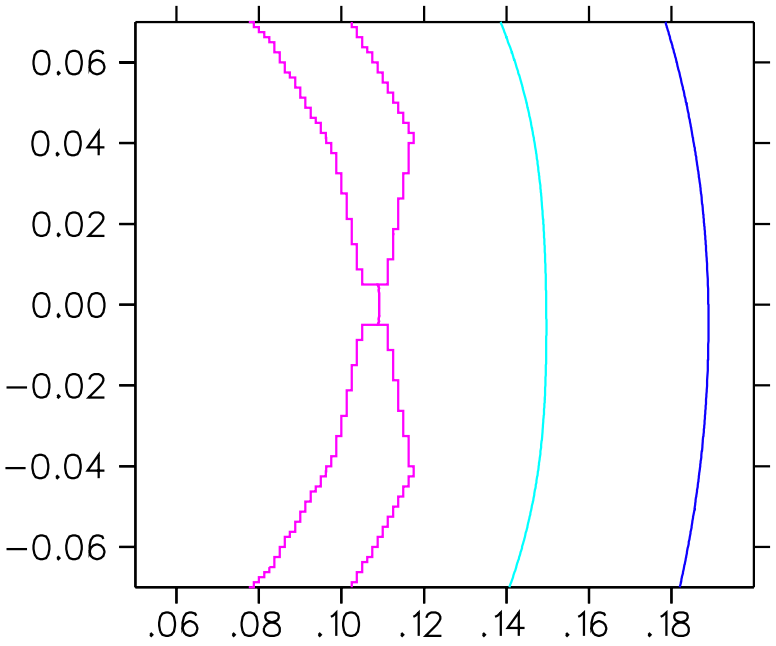

Figure 3.25: Plasma Boundary Shape (with an Image Electrode Voltage of 20 kV) Which Best Matches the Beam Produced by the 0.010" Slit Chimney.

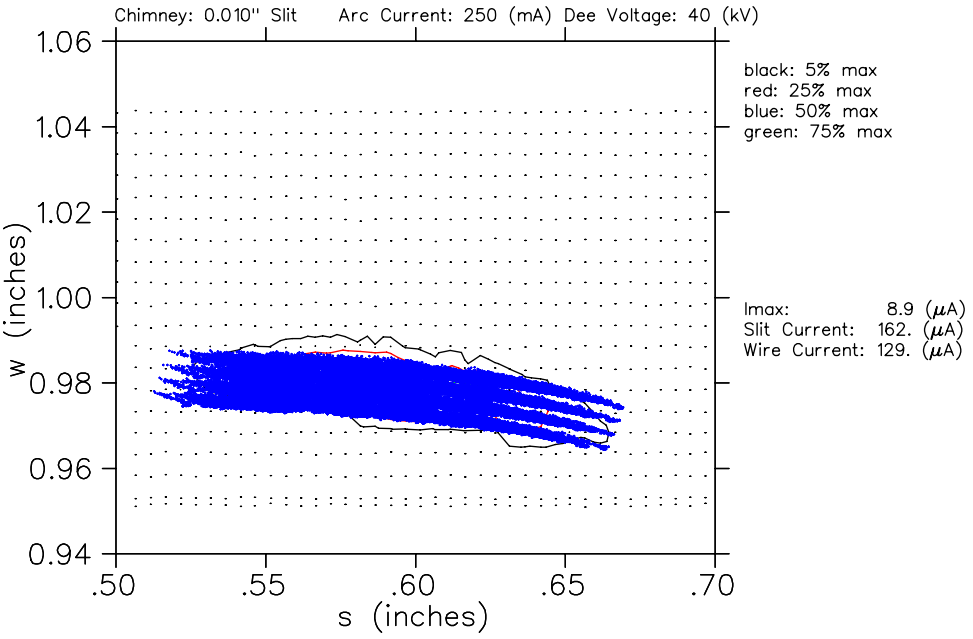

(a) Radial (s, w) Match

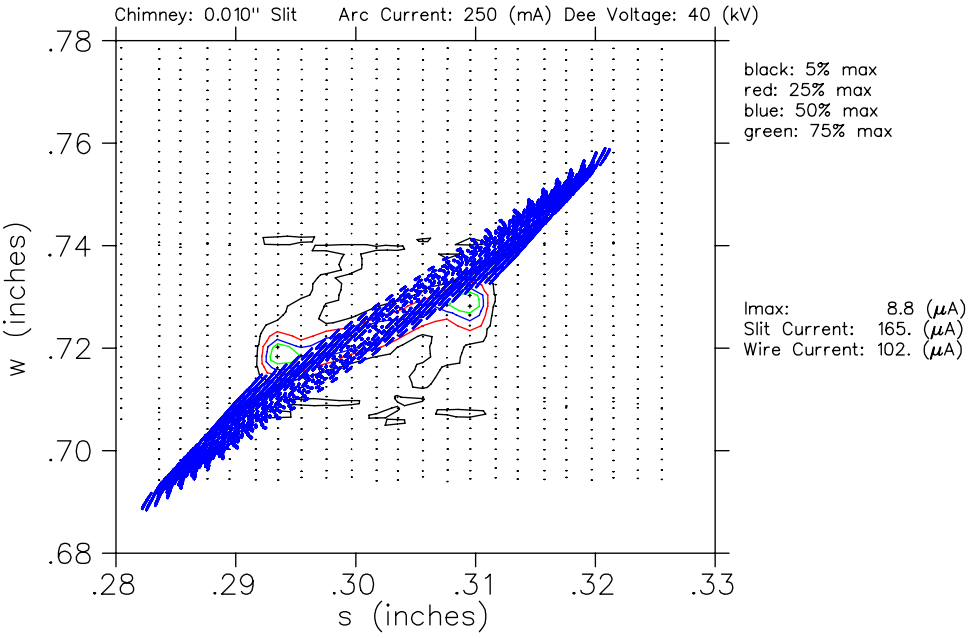

(b) Axial (s, w) Match

Figure 3.26: Tracked Orbits Which Best Match the 0.010" Slit Chimney

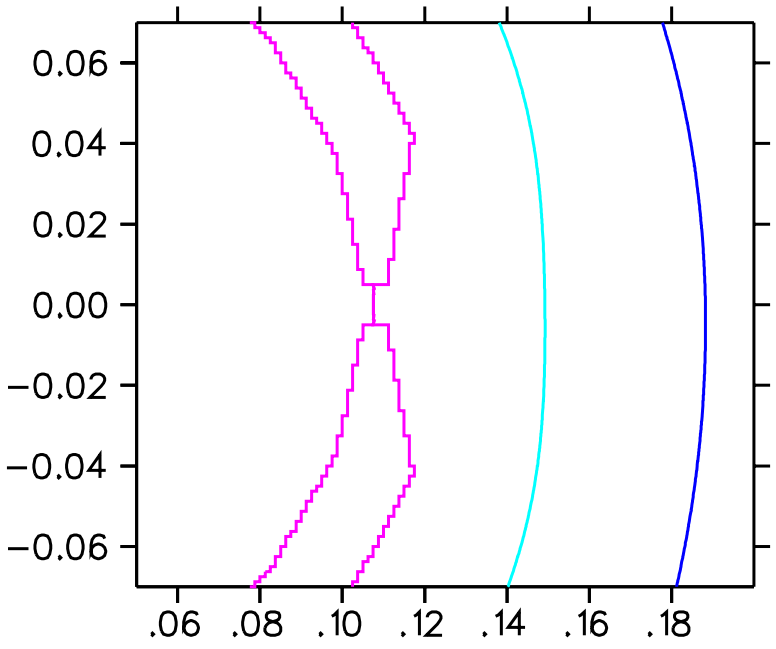

(a) More Concave Plasma Boundary: Image Electrode 8 kV

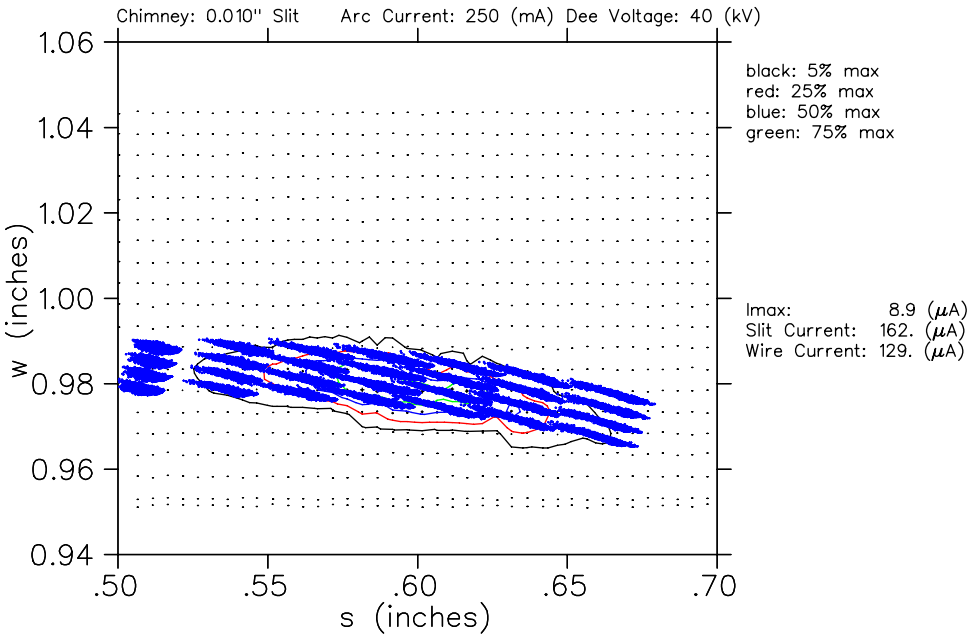

(b) More Concave Radial Plot: Image Electrode 8 kV

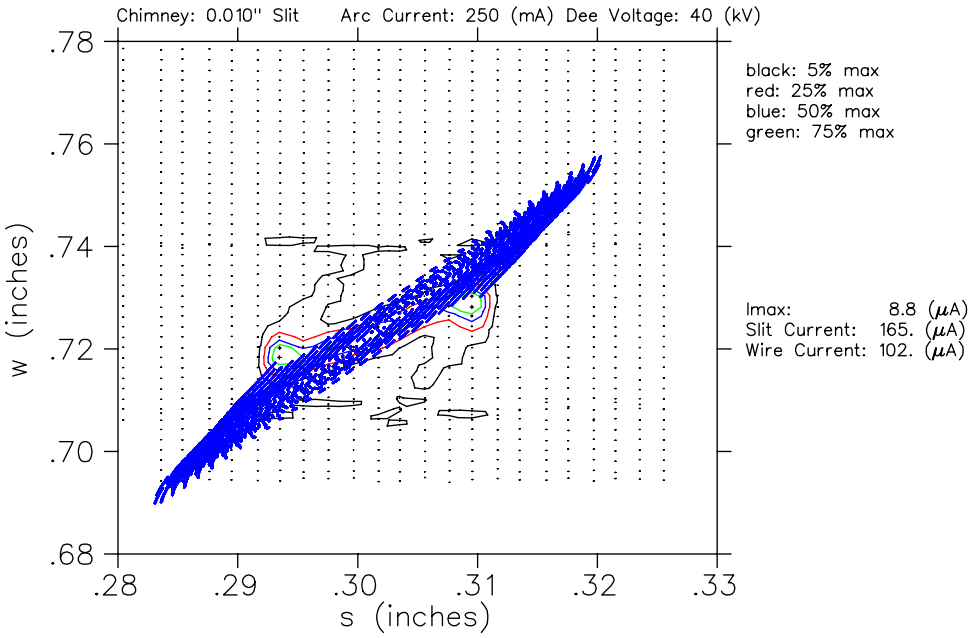

(c) More Concave Axial Plot: Image Electrode 8 kV

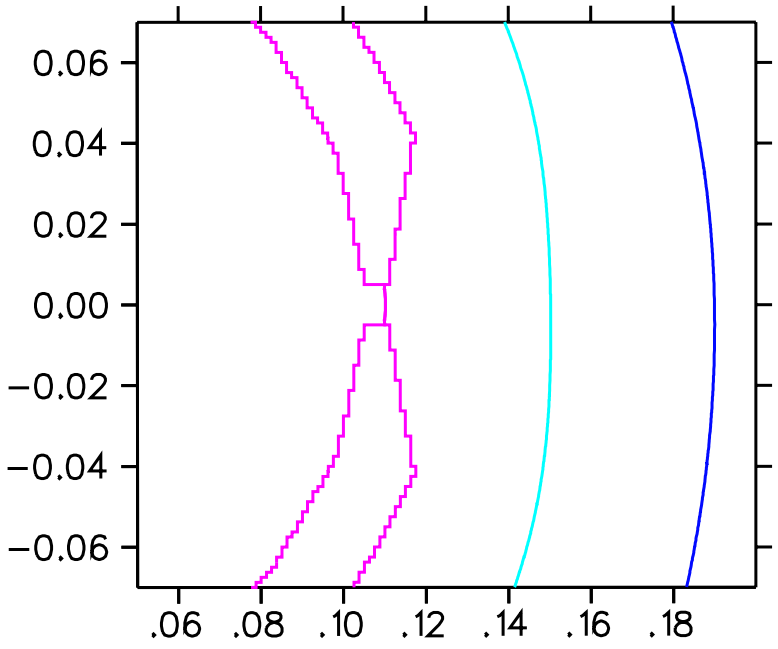

(d) More Convex Plasma Boundary: Image Electrode 36 kV

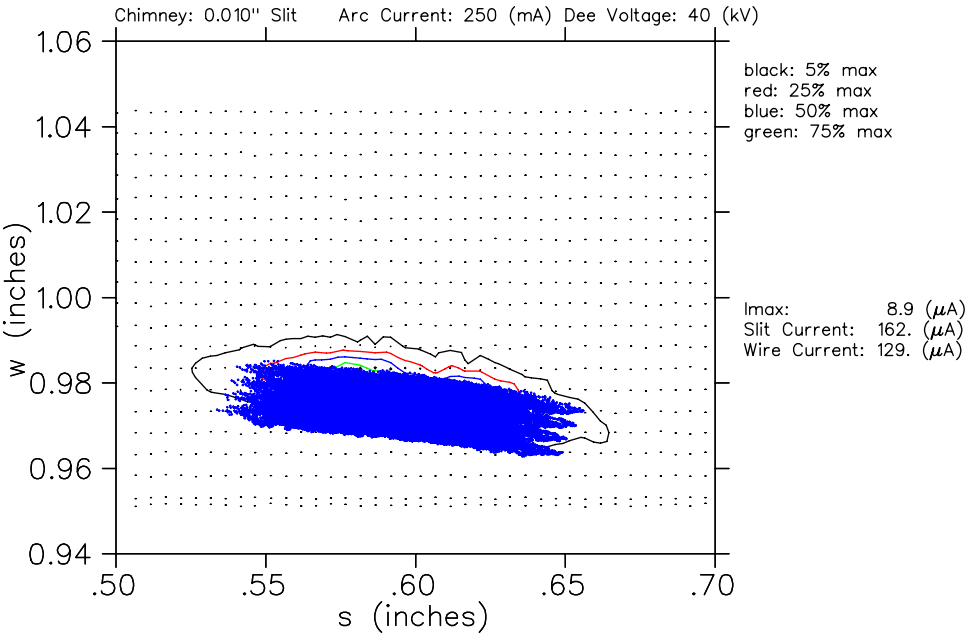

(e) More Convex Radial Plot: Image Electrode 36 kV

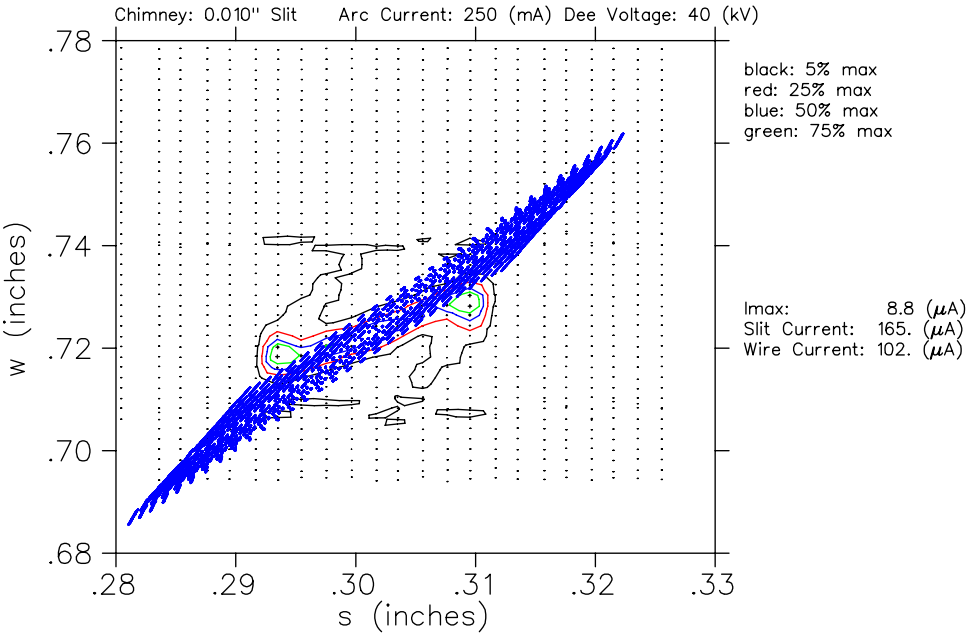

(f) More Convex Axial Plot: Image Electrode 36 kV

Figure 3.27: Different Plasma Boundaries for the 0.010" Slit Chimney Match

Figure 3.25 show the plasma boundary that produced the best match between calculations and experimental data for the 0.010" (0.25 mm) slit chimney with figure 3.26 showing the relevant (s, w) plots. The fit was produced with a flat plasma (image electrode voltage of 20.0 kV). The computed orbits give an excellent fit to the radial (s, w) plot of the experimental beam (figure 3.26a), namely they produce a plot with the same size in s and w, the same curvature, and the same orientation.

The computed orbits match the axial (s, w) plot of the experimental beam to a lesser extent in that they produce a plot with the same area in (s, w) space (and therefore also with the same emittance), however, the shape of the beam in axial (s, w) space does not match. Immediately obvious is the fact that the computed beam has approximately two times the range of values of s and w meaning that the computed beam is twice as tall in z at the slit and wire probe positions. Also, the focusing "tails" at the ends of the beam are suppressed and the slope of the computed beam is steeper than the experimental beam.

Figure 3.27 shows the effect of changing the image electrode voltage. A more concave plasma boundary (image electrode of 8 kV) produces a beam that is too large in the radial s parameter and has little effect on the z plot (improving the fit only slightly). A more convex plasma boundary (image electrode 36 kV) produces a beam that is too small in the radial s parameter and increases the size of the z plot slightly so that it is less of a match for the experimental beam.

Figure 3.28 shows the plasma boundary that produced the best match between calculations and experimental data for the 0.020" (0.50 mm) slit chimney with figure 3.29 showing the relevant (s, w) plots. Again, this fit was produced with a flat plasma (image electrode voltage of 10.0 kV).

The computed orbits match the radial (s, w) plot of the experimental beam in that they produce a plot with the same size in s and w, and the same curvature.

However, the calculated orbits are rotated with respect to the experimental beam. This rotation has to do with the location of the "crossover" of the beam (see figure 3.30). If the crossover is after the wire probe, parts of the beam with larger s values will also have larger w values producing a positive slope in the (s, w) plots. If the crossover is before the wire probe, parts of the beam with larger s values will have smaller w values producing a negative slope in the (s, w) plots. If the crossover is right at the wire, the (s, w) plot will be symmetric. The experimental data shows evidence that the beam has crossed over before reaching the wire probe. The location of the crossover of the calculated trajectories can be adjusted by changing the plasma boundary, but no change in the plasma boundary moved the crossover enough to match the experimental beam.

Similar to the 0.010" slit case, the computed orbits for the 0.020" slit do not match the axial (s, w) plots as well as they do the radial (s, w) plots.

Figure 3.31 shows the effect of choosing different plasma temperatures. 10,000 K (3.35 eV maximum starting energy) appears to be too low a temperature to provide a reasonable match for the experimental beam while 55,000 K (18.4 eV maximum starting energy) appears to be too large.

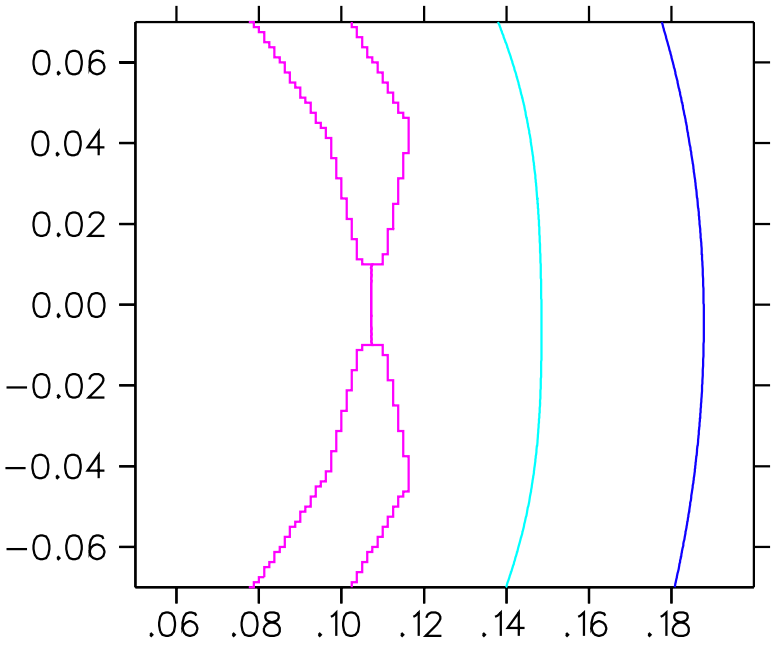

Figure 3.28: Plasma Boundary Shape (with an Image Electrode Voltage of 10 kV) Which Best Matches the Beam Produced by the 0.020" Slit Chimney.

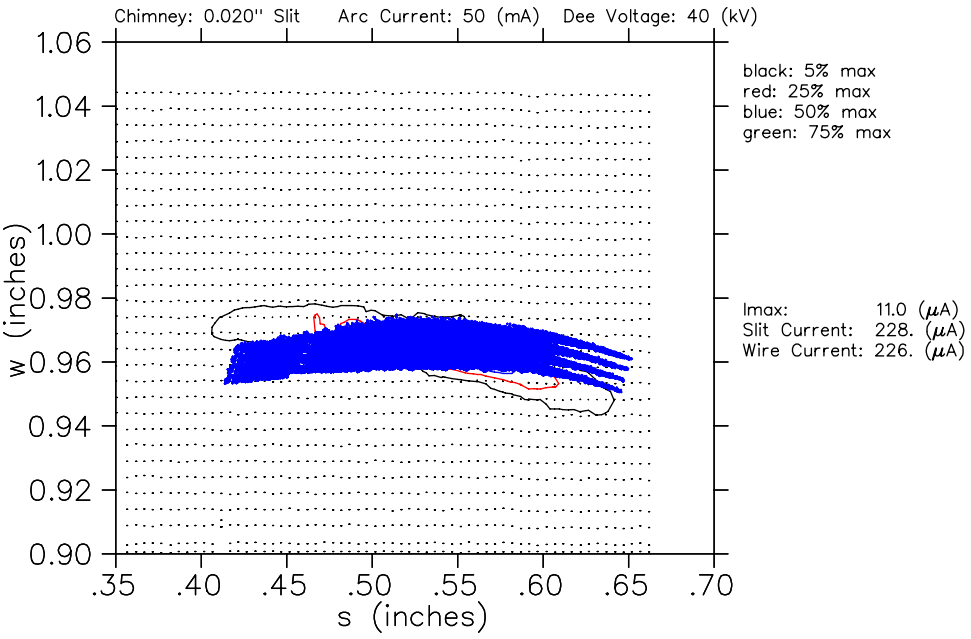

(a) Radial (s, w) Match

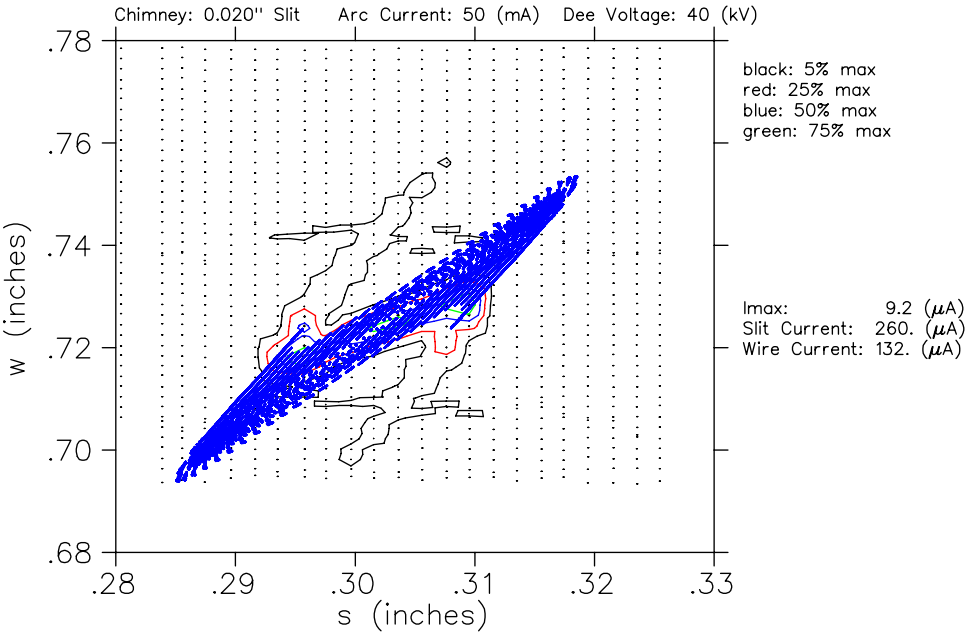

(b) Axial (s, w) Match

Figure 3.29: Tracked Orbits Which Best Match the 0.020" Slit Chimneys

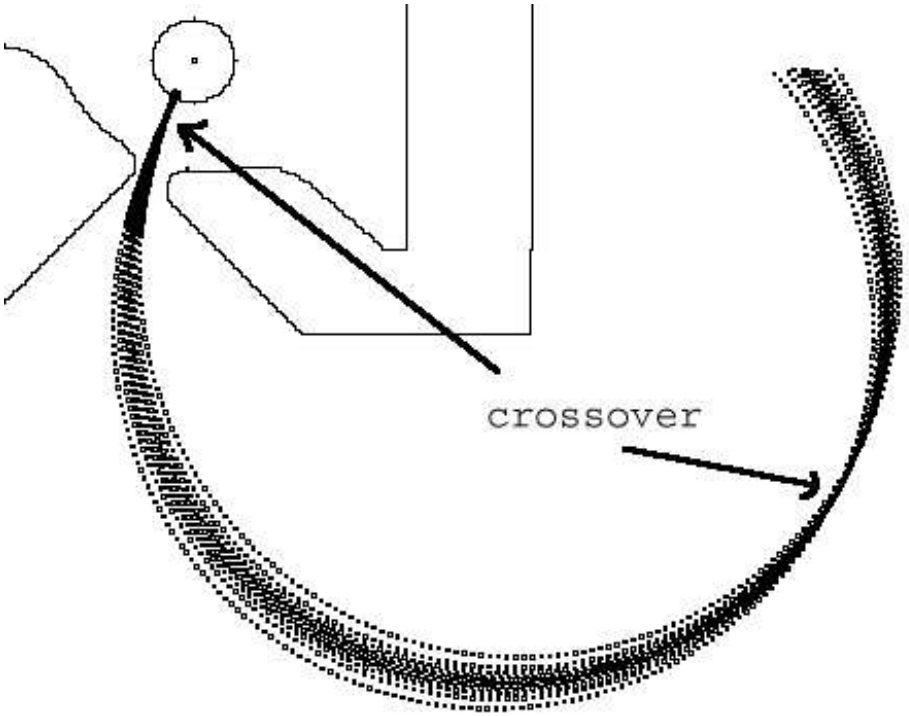

Figure 3.30: The beam crosses over itself twice, once just after exiting the chimney and again approximately 180 degrees downstream.

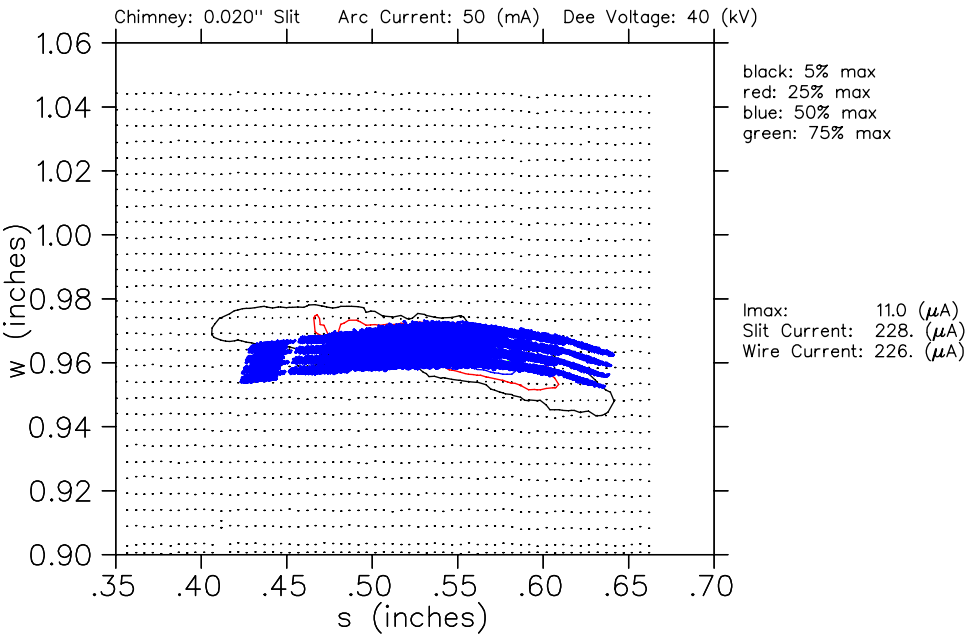

(a) Radial (s, w) plot with 10,000 K

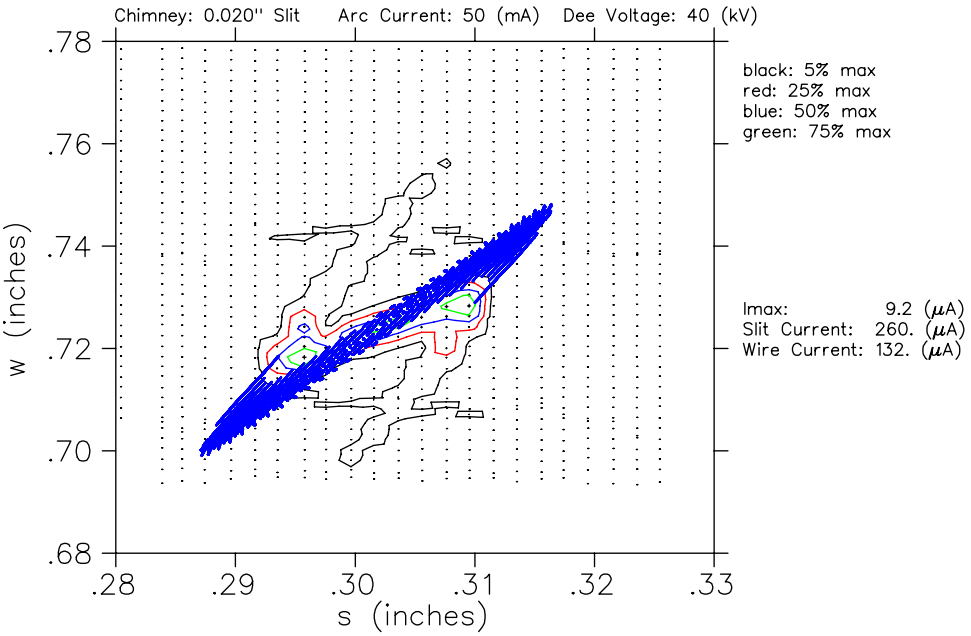

(b) Axial (s, w) plot with 10,000 K

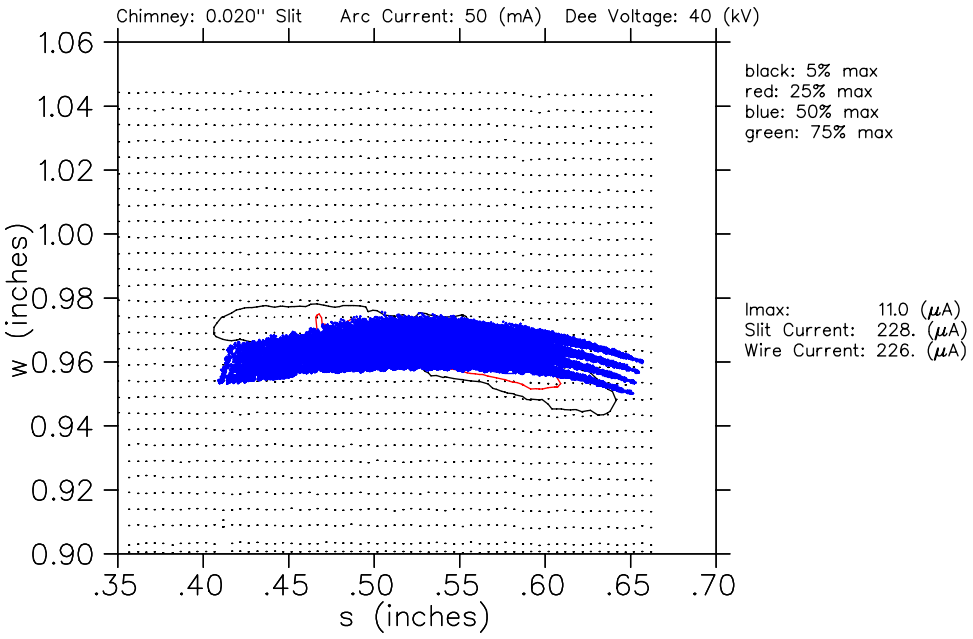

(c) Radial (s, w) plot with 55,000 K

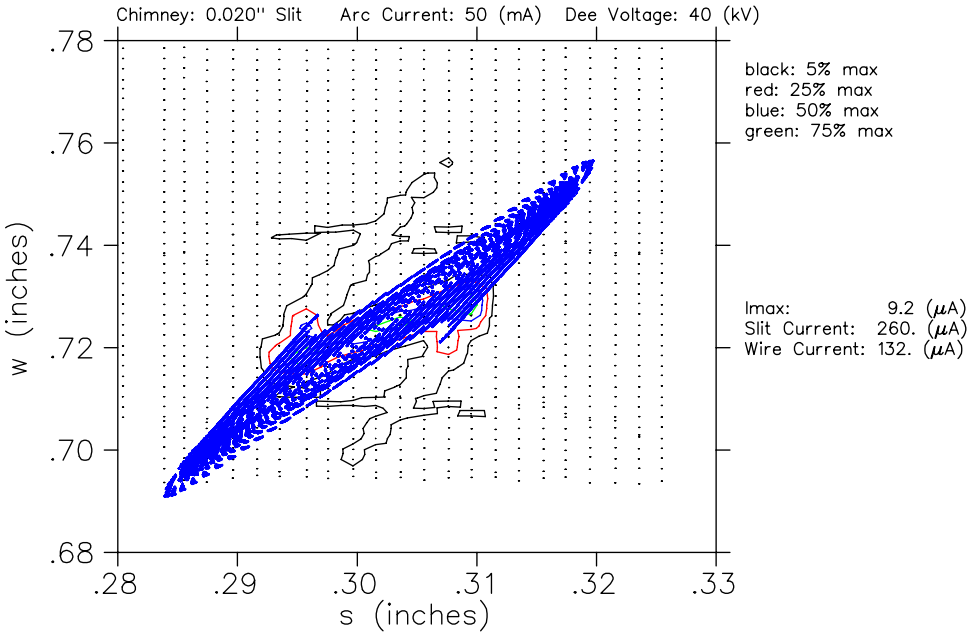

(d) Axial (s, w) plot with 55,000 K

Figure 3.31: Different Plasma Temperatures for the 0.020" Slit Chimney Match

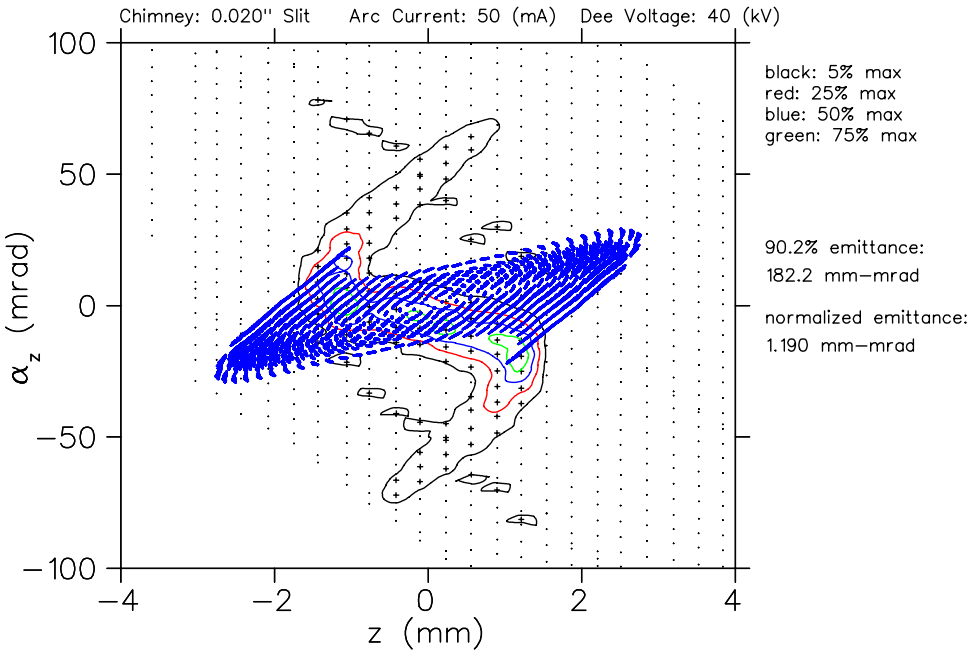

Figure 3.32: Axial Emittance Plot Comparing Calculations to Experiment for the 0.020" Slit Chimneys

Axial Focusing in the Source-Puller Region

For a better understanding of the mismatch in z between the calculated orbits and the experimental beam, it is helpful to look at a z emittance plot. Figure 3.32 shows the same data as figure 3.29b but now plotted with α_z versus z (as explained in section 3.1.4). We see that the experimental data (contours) have a general negative slope such that rays that cross the slit with positive z tend to have a negative angle α_z and rays that cross the slit with negative z tend to have positive angles. This represents a converging, or focused beam. The computational data (blue dots) have the opposite behavior showing a general defocusing trend. Also, the "tails" at the ends of the beam which are a result of the focusing electric field at the top and bottom of the source slit are less pronounced in the computed data. Overall, the experimental beam is more strongly focused than the computed trajectories.

Figure 3.33 shows tracked orbits starting on the plasma boundary with z and p_z

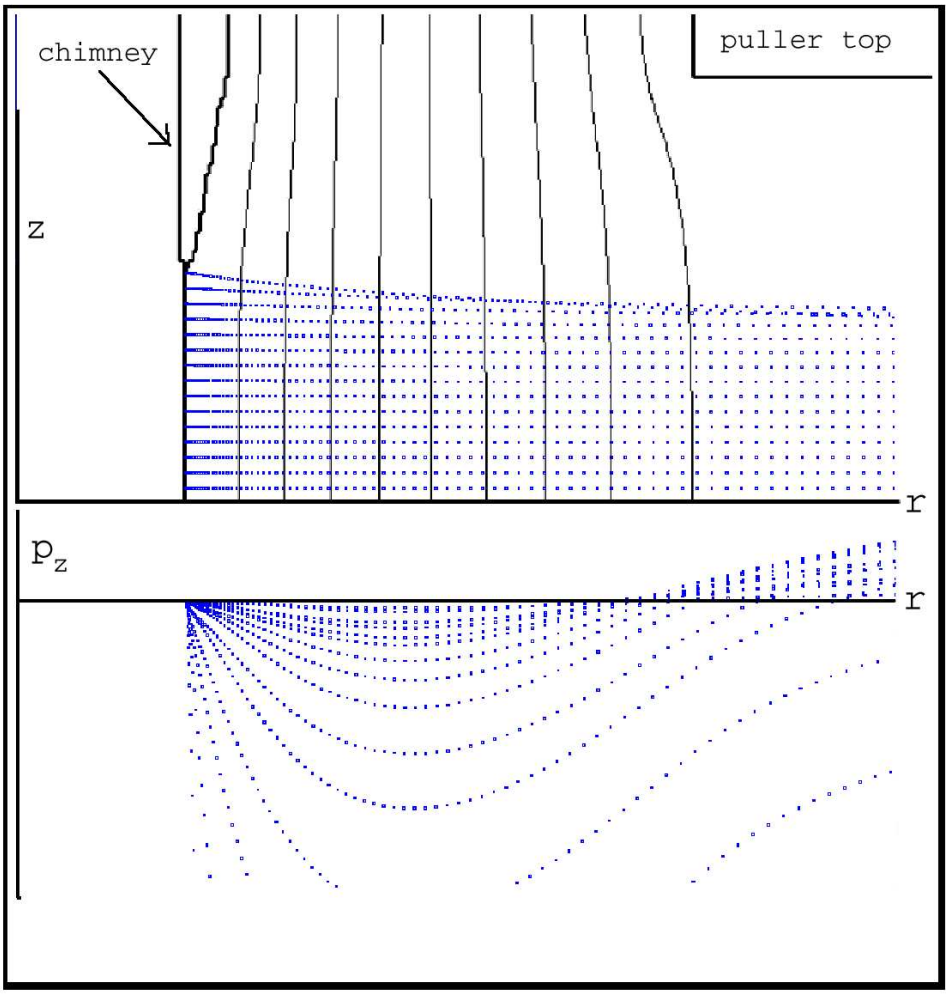

Figure 3.33: z and p_z in the Source-Puller Region

graphed with respect to r [3]. (15 orbits, each above the median plane, are shown.) The z vs. r plot show the overall behavior, the top few rays are initially focused before returning to a roughly horizontal trajectory. The central rays appear to travel horizontally through the source to puller region with little focusing or defocusing. The p_z vs. r plot is more sensitive to small deviations from a horizontal path showing that all the rays, even those close to the median plane, move toward negative p_z values while exiting the chimney. Since the rays are above the median plane, negative p_z denotes a focused beam, and in the region close to the chimney, the beam is becoming increasingly focused. About half way between the chimney and the puller, the focusing effect of the electric field reverses and the p_z values move back toward zero i.e. the trajectories are returning toward horizontal. By the time the beam enters the puller, most of the rays have reached positive p_z indicating that they are now diverging or defocused. For the majority of the beam (11 out of 15 rays shown) the defocusing effect from the puller is stronger than the focusing from the chimney resulting in a positive p_z.

The above analysis holds for the computed orbits, but we know from the experimental data that the real beam is converging (focused) by the time it reaches the slit probe. The computational model either underestimates the focusing of the beam near the chimney or overestimates the defocusing of the beam as it enters the puller. It is not clear at this point why this discrepancy exists.

3.3.2 Hole Source

For the hole chimney calculations a total of 528,220 rays were tracked. There are 961 possible different starting positions for the ions inside the chimney opening (31x31 in

[3]Here r refers to the distance from the center of the chimney, not the center of the orbit as in section 3.1.3.

a 0.047" square grid) of which 539 lie within the 0.047" (1.19 mm) diameter source opening. 49 different starting angles were tracked from each starting position 7 angles in the median plane (covering 103 degrees), 7 different starting angles vertically (covering 103 degrees). 20 different rays were tracked for each combination of starting position and starting angle; five different starting energies representing a plasma temperature of 35,000 K and 4 different accelerating voltages (17.3±0.03 kV in equal steps). Orbits which came into contact with the chimney before exiting the chimney opening were dropped as were orbits which hit the puller.

Figure 3.34 shows the plasma boundary which produced the best fit between computed orbits and experimental measurement for the Harper style chimney with figure 3.35 showing the relevant (s, w) plots. The best match between computed orbits and experimental data was achieved by using a highly concave plasma boundary; an image electrode voltage of 600 V was used. This plasma boundary produced strong over focusing between the chimney and the puller.

The computed rays match the experimental data well for the radial plots. The shape of the beam when plotted in (s, w) space is the same for experimental and computed data. Similar to the case with the 0.020" slit chimney, the experimental and calculated plots differ by a rotation indicating the the crossover point is for the calculated rays is not the same as the experimental beam.

The experimental and calculated axial plots are both a straight line with wire parameter w increasing linearly with slit parameter s. The slope of the beam in (s, w) space is not identical indicating that the calculated orbits are diverging faster than the experimental beam.

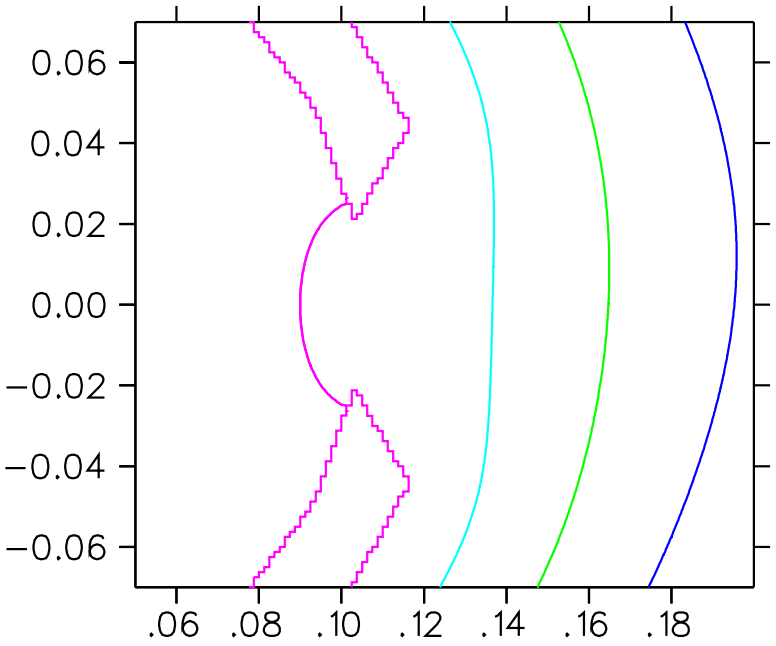

Figure 3.34: Plasma Boundary Shape (with an Image Electrode Voltage of 0.6 kV) Which Best Matches the Beam Produced by the 0.047" Hole Chimney.

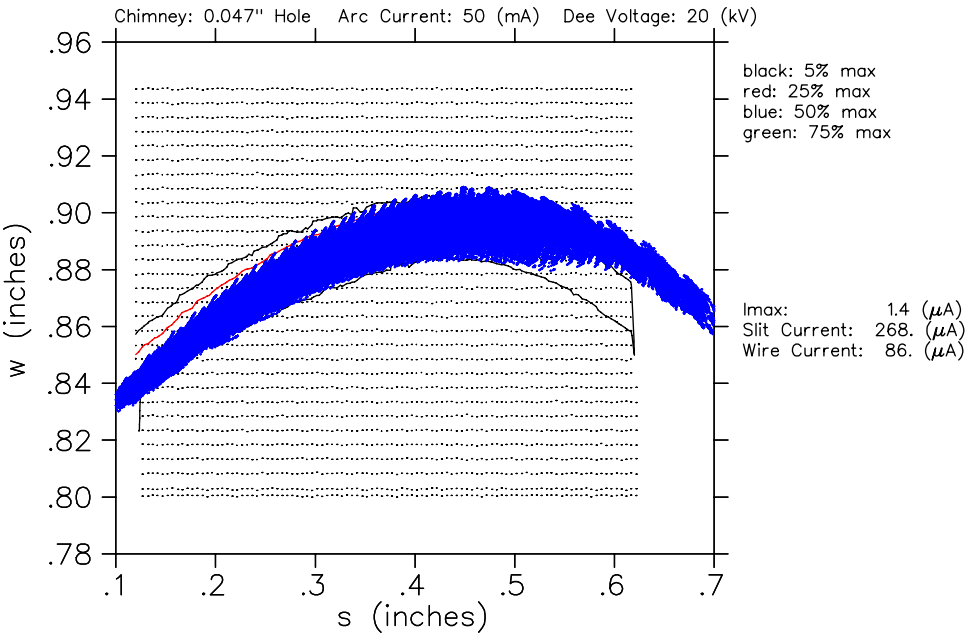

(a) Radial (s, w) Data

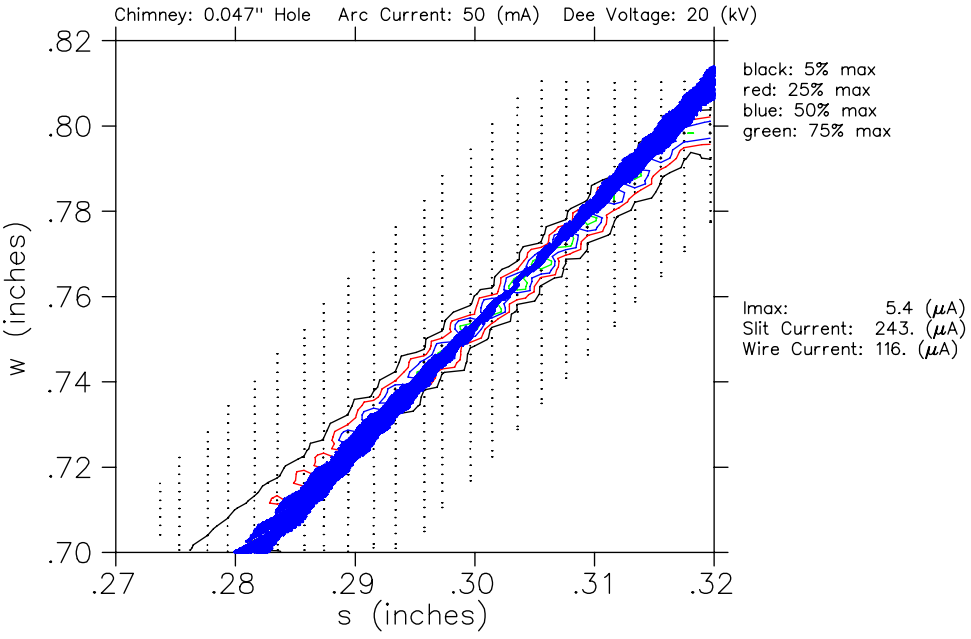

(b) Axial (s, w) Data

Figure 3.35: Tracked Orbits Which Match the Hole Chimney

Chapter 4

Conclusion

Characterizing the Cold Cathode PIG Ion Source

The construction of the Ion Source Test Stand at the NSCL has allowed us to measure the radial and axial emittance and luminosity of a cold cathode PIG internal ion source under dc extraction. To the best of our knowledge, these are the first such measurements made on a cold cathode ion source. (Measurements for filament style internal ion sources were reported by Mallory in 1966.)

The slit chimneys produced a beam that was nearly horizontal (in z) and was, on average 70% as tall as the chimney opening after passing through the puller. The hole chimney produced a beam that (in the absence of strong focusing) diverged in z.

A general trend of increasing accelerated current (and luminosity) with increasing arc current was observed. The maximum measured luminosity of 7.1 $\frac{A}{cm^2-sr}$ was obtained with the 0.010" (0.25 mm) slit chimney running at an arc current of 450 mA and a gas flow rate of 3.0 cc/min (at STP). Higher luminosities would likely have been possible with the 0.020" slit chimney had we been able to run it at similar arc currents, but the accelerated current of 590 μA with a 40 kV puller voltage

and 150 mA arc current were considered to be near the cooling limit of the test stand apparatus. The 0.047" "hole" chimney (the style used in the Harper Medical Cyclotron) produced a deuteron beam of over 700 μA with a puller voltage of 20 kV and arc current of 250 mA.

For the 0.010" slit chimney producing currents ranging from 52 to 227 μA, the emittance of the beam did not change significantly as the arc current (and hence the beam current) was increased. For the 0.020" slit chimney producing currents ranging from 230 to 590 μA increasing the beam current by 160% increased the radial emittance by 38% and the axial emittance by 25%. The emittance growth is evidence that either the shape of the plasma boundary changes with increasing current, or that increased space charge forces are causing the emittance of the beam to grow,

Matching Experimental Beams With "Single Particle" Orbit Tracking

With appropriate initial conditions, the orbit tracking code Z3CYCLONE is able to predict to good accuracy the beam produced by the cold cathode PIG ion source. Starting orbit tracking on the so called "plasma boundary," (the zero volt equipotential that crosses the opening in the chimney) we were able to produce sets of calculated orbits which matched the radial emittance of the experimental beam very well, while somewhat underestimating the axial focusing of the beam between the source and the puller. Designing a cyclotron with an aperture adequate to accept the calculated beam therefore represents a conservative approach.

In each case presented in this study, a plasma temperature of approximately 35,000 K (resulting in a maximum energies for calculated trajectories of about 12 eV) provided the best agreement with experimental beams.

No general rule was found for choosing an image electrode voltage (i.e. plasma

boundary shape) which would best match the experimental beam for all chimneys. For the slit chimneys, an approximately flat plasma provided the best match for the radial emittance of the experimental beam while somewhat over estimating the size of the beam in z, and for the chimney with a 0.047" diameter hole a highly concave plasma was found to provide the best match. (The beam produced by an internal ion source clearly depends strongly on the shape of the opening in the chimney; and the appropriate starting conditions for each new chimney design will need to be determined experimentally.)

Future Work

Because the beam extracted from the ion source is strongly dependant on the shape and size of the opening in the chimney, it may be possible to observe significant gains in luminosity by optimizing this shape. In particular, gains in luminosity were seen when moving from a 0.010" (0.25 mm) slit to a 0.020" (0.50 mm) slit, a natural choice would be to try even wider slits. The depth and angle of the chamfer can also be further optimized. The chamfer in both of the slit chimneys tested was 10° (a value which was used based on the results of the 0°, 10° and 20° used in Mallory's studies with a filament source), however further optimization of this angle for cold cathode ion sources may be possible and should be explored. Finally, the chamfer for both chimneys was 0.010" deep (out of a 0.020" thick chimney wall) leaving a 0.010" deep "tunnel" which may not be optimal, especially for the more narrow 0.010" slit. Increasing the depth of the chamfer may allow higher beam currents from the source.

When a plasma is confined in a magnetic field it may be appropriate to model the plasma as having two different temperatures $T_{\parallel}$ and $T_{\perp}$ representing two different Maxwellian distributions for the components of velocity parallel and perpendicular to the magnetic field.[22]. This dual temperature modeling of the plasma may allow

for a better match between the experimental beam and calculated orbits.

The fact that increasing the beam current resulted in an increase in emittance of the beam produced by the 0.020" (0.50 mm) wide slit chimney indicates that space charge may have an effect on the beam in the region between the chimney and the puller. While the results presented in this dissertation indicate that single particle codes are sufficient for cyclotron design studies, higher quality matches between calculated and experimental beams may be possible with an orbit tracking code which takes space charge into effect. Development of such a code or adaptation of existing space charge codes to orbit tracking in the central region of a cyclotron would test this hypothesis.

Appendix A

Ion Source Test Stand Operation Manual

Updated July 2004

A.1 Safety Procedures

A.1.1 High Voltage Operating Procedure

1. Introduction

   This document describes a procedure to be followed by personnel accessing exposed high voltage equipment inside the safety cage in the N1 vault.

2. Authorized Personnel

   No one should access the inside of a high voltage cage who is not authorized to work on the system. Authorized personnel include Ted Forringer Henry Blosser and Malay Dey. Please contact one of these if you need access to this high voltage cage.

3. Steps to Activate High Voltage System:

   (a) Close the cage door, and insert the key into the interlock device.

   (b) Check that the cage is secure.

   (c) Turn on the high voltage supply.

   (d) Set high voltage as needed.

4. Steps to Turn OFF the High Voltage System:

   (a) "Dial down" high voltage supply so that the set point is O K V.

   (b) Turn off high voltage supply.

   (c) Open cage, tripping safety interlock switch.

   (d) Before contacting any surface, use the shorting hook to discharge any possible high voltages, noting the result as follows: Touch the tip of the grounded hook to all major metal surfaces, including the high voltage feed connection. If a spark is noticed while doing this, there is a safety problem that must be repaired. If a spark is noticed each time the hook touches a surface beyond the first time, the high voltage may still be on!

   MAKE SURE OTHER MEANS ARE USED TO REMOVE HIGH VOLTAGE FROM THE APPARATUS BEFORE CONTACTING ANY SURFACE!

   Leave the shorting hook connected to the apparatus if possible.

   (e) The system is now safe.

A.1.2 Raising the Cap

Authorized personnel only may raise this magnet cap or work inside this magnet. If access to inside of magnet is needed, contact Ted Forringer, Henry Blosser, Malay Dey or Gunter Stork.

1. Open the high voltage cage.

   (a) Follow the procedure for opening cage.

   (b) Maintain visual control of cage to ensure HV will remain off while working inside the magnet.

2. Vent the magnet (follow the procedure in section A.3).

3. Ensure magnet power supply is off.

4. Undo magnet current and interlock connectors (between top and bottom).

5. Disconnect water and arc supply from top half of the source.

6. Disconnect arc supply from the bottom half of the source.

7. Remove upper source tray.

8. Crank first three turns by hand.

A.1.3 Working on top of the Magnet

Authorized personnel only may work on top of this magnet. If access to top of magnet is needed, contact Ted Forringer, Henry Blosser, Malay Dey, or Gunter Stork.

1. Open the high voltage cage.
   (a) Follow procedure for opening cage.
   (b) Maintain visual control of cage to ensure HV will remain off while working on top of magnet.
2. Remove all loose items (tools etc.) from top of magnet when work is finished.

A.2 Running a Beam

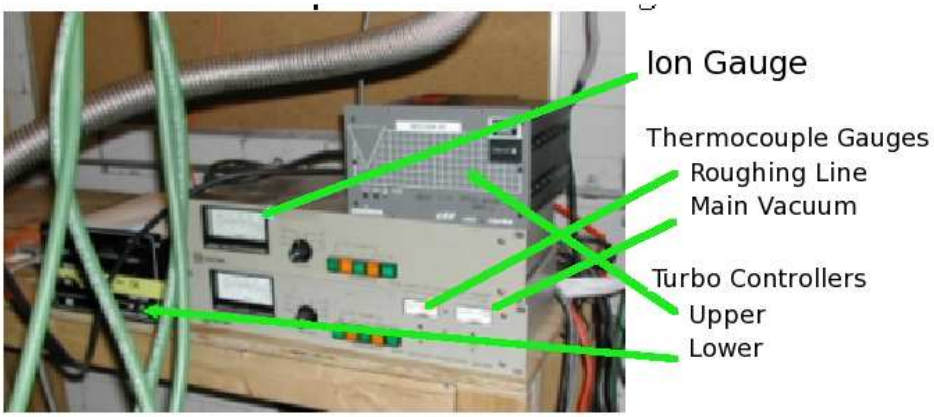

A.2.1 Pump down the vacuum

1. Close the magnet and all valves.
2. Open the hydrogen/deuterium gas supply valve on the lower source.
3. Turn on the flow meter and set to less than 0.1 cc/min.
4. Start rough pumping, by plugging in the roughing pump.
5. Turn on the thermocouple gauges. Wait until both TC gauges read between 100 and 300 mTorr before turning on turbo-pumps.
6. Turn on both turbo pumps.
7. When both TC gauges read "zero" pressure (pegged to left of scale) turn on the Ion Gauge. Vacuum should reach better than $2x10^{-5}$ with 1.0 cc/min gas flow, or $8x10^{-6}$ with gas valve closed. Expect 4 to 6 hours of pumping for a good vacuum.

Turn on the magnet

1. Check that the orange cable and the interlock cable connecting the upper and lower magnet coils are attached.
2. The magnet power supply is the approximately 3 x 3 x 2 foot black and tan crate in the North East corner of the vault. Ensure that the circuit breaker is in the "on" position.
3. The power supply is named SRCTSTMAG and can be accessed from the PLCApp or ArcNet MDI 32.

Turn on the high voltage

1. Follow the procedure listed in the safety section.
2. The dee voltage power supply is the Spellman 100KV supply on the electronics rack on the north side of the vault.
3. The voltage is controlled with a hand held "battery box." The switch on the box should be set to (-) "negative."
4. If the deuteron puller is being used, set the puller voltage to 20 KV.
5. If the proton puller is being used, set the puller voltage to 40 KV.
6. Wait for sparking to stop before turning on source. This should take less than one minute if the test stand has been run recently.

Turn on the source

1. The power supply is the tan Glassman 3KV supply in the electronics rack.
2. Follow this checklist before turning on the source.
   (a) Double check vacuum is below $7X10^{-6}$ Torr.
   (b) Double check that all five water lines are connected; two sets for each source, plus one going into the high voltage cage.
   (c) Double check that the magnet is on.
   (d) Double check that the gas (hydrogen or deuterium) is flowing at 0.5 to 6.0 cc/min.
   (e) Double check that the dee voltage is on and has stopped sparking.
3. Set the current limit for the arc before turning the supply on.
   (a) 50 mA - gives a very stable "low current" beam.
   (b) 250 mA - the standard testing mode - higher current.

(c) 450 mA - maximum current mode (may overheat dee if run for long periods of time).

4. Press the green "on" button.

5. The dee will start sparking again. Wait until these sparks are less frequent than about 10per minute. Less sparks will result in better data.

6. The source is working correctly, and the beam is being accelerated if:

   (a) The current read on the arc power supply is equal to the set point.

   (b) The voltage read on the arc power supply is between 1.0 and 2.7 KV.

   (c) The red light above the current set knob is on.

   (d) The red light above the voltage set knob is off.

   (e) There is a purple/red glow coming from the chimney.

7. Common problems:

   (a) Voltage reads 3KV and current reads zero. "Open Circuit." Check that both arc supply leads are plugged into the sources.

   (b) Voltage reads 3KV and current reads below set point. "Arc not struck."

      i. Increase gas flow.

      ii. Decrease cathode/anode gap.

      iii. Replace cathode.

   (c) Current reads at set point, voltage is unusually low, no glow from chimney. Short circuit: clean anode, possibly replace cathode.

   (d) The red light above the voltage knob is on and the red light above the current knob is off. "Bad arc." Current is probably being "pulsed." This is not desirable, but it is still possible to take data. Try increasing gas supply or decreasing cathode/puller gap.

A.2.2 Probes, BCM and Software

There are five devices associated with this experiment that can be accessed from the computers.

1. SRCTSTMAG - the airport magnet power supply. Read only.
2. N1PRBE and N1PRBW the motor controls for the probes. E (east) is the wire probe. W (west) is the slit probe. These can be set and read.
3. N1BCME and N1BCMW the beam current monitors. E is the wire and W is the slit. Read only.

Programs for accessing these devices:

1. ArcNet MDI 32 (anetmd32.exe): This program can read and set devices. It is useful for moving the probes or reading the magnet current.
2. Chart Recorded 32 (bcmchart.chr): This program plots the output of any device as a function of time. This is useful for monitoring the progress of a run.
3. BCM program (N1BCM.mt2). This program is used to talk to the beam current monitor. At the very least it must be used to turn on (init) each channel. If the beam current suddenly goes to zero during a run, you will need to INIT both channels again.
4. Sequencer: This program is the main control program for taking data. It reads an input file and sets the desired position for the probes. It then writes an output file with the probe position and current readings.

A.2.3 Steps for taking data once the source is on.

1. Check that BCM is turned on. A green flashing light on the back of the box tells you that it is working. Also, the Ethernet to fiber (small box) should be on.
2. Go back to you computer. Open the BCM program and initialize both channels. Channel one is the wire; channel two is the slit.
3. Open the chart recorder and set the ranges to appropriate values.
4. Open the Sequencer program
   (a) Choose an input file this file will have a list of commands telling the sequencer where to place the probes.
   (b) Choose an output file Sequencer will write the data to this file.
   (c) Press start.
   (d) Watch the chart recorder to make sure everything is going correctly. You should be able to monitor the motion of the probes, the total current hitting the slit, and the current hitting the wire. Slit current should be relatively constant, while the wire current will show intermittent peeks.

A.3 Shutting Down

1. If you are going to stop taking measurements for several hours, but will be back the same day:

   (a) Turn off the arc supply. The cathodes have a limited lifetime. Turning off the arc current will prevent the cathode from being wasted.

   (b) Turn off the dee voltage battery box (the box that sets the voltage level). There is no need to waste the battery, and there it is safer to turn off the high voltage when not in use.

2. If you are leaving for the day, but expect to continue taking data tomorrow: Do everything above plus:

   (a) Turn down the gas flow until the flow meter reads negative. This will stop the gas from flowing.

   (b) If you do not need the magnetic field to remain constant, it is a good idea to turn off the magnet. If you are going to use the same magnetic field in your data tomorrow, it is OK to leave the magnet power supply on overnight.

3. If you are done taking data for several days: Do everything above plus:

   (a) Disconnect the power from the gas flow meter.

   (b) Close the valve on the gas bottle.

   (c) Turn off both turbo pumps. There is no need to turn off the roughing pump unless you are venting the magnet.

4. If you need to do maintenance inside the magnet or are shutting down for an extended period of time:

   Do everything above plus:

   Vent the magnet.

   The important thing here is not to damage the turbo pumps. Venting too quickly or causing a high pressure on the back of the turbo can damage the pump. Do not open any valves quickly or stop the roughing pump until both turbos have stopped spinning.

   (a) Turn off the turbo pumps.

   (b) There is a valve on each half of the ion source.

   (c) Open the valve slowly until you see the pressure on the TC gauge start to rise, and then close the valve again.

   (d) Wait 3 to 5 minutes for the turbos to pump out all the air you just allowed into the vacuum chamber. This pumping will slow the turbos down.

(e) Repeat steps 2, 3 and 4 several times until the turbo pumps have stopped spinning. You can tell they have stopped by placing you hand on the pump, if you do not feel any vibration the turbo pump has stopped spinning.

(f) You can now close the valve for the roughing pump and open the vent valve to let air back into the magnet.

A.4 Maintenance Procedures

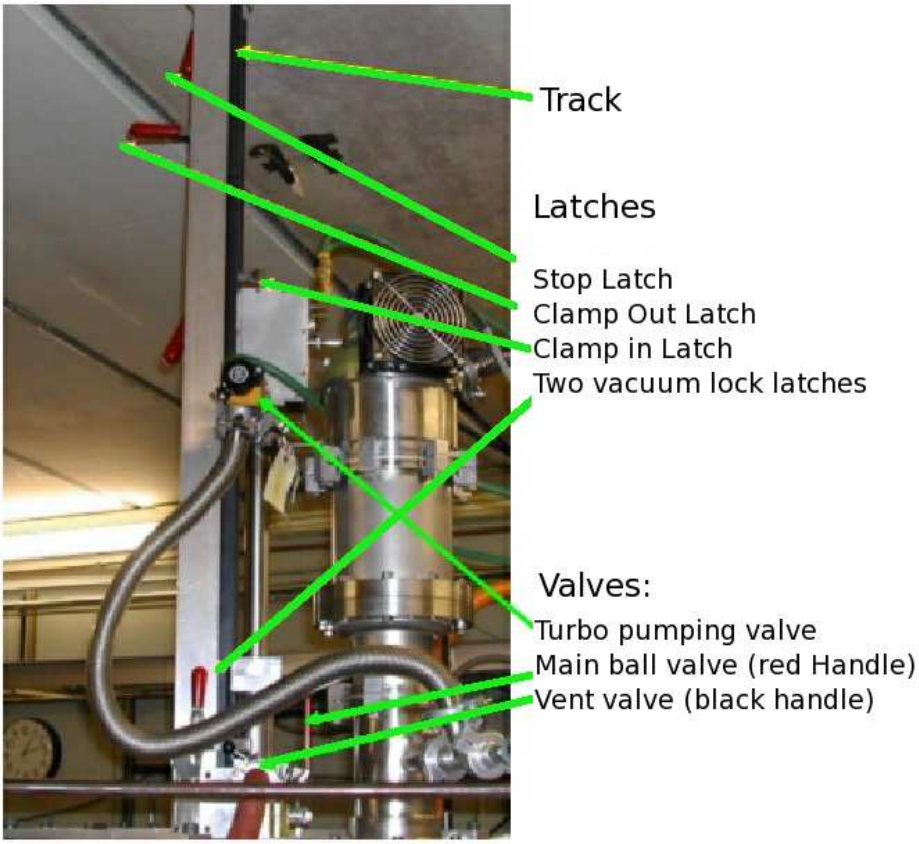

A.4.1 Removing a source without venting the magnet

The most important thing to keep in mind when removing a source is that we need to protect the turbo pumps from any sudden rush of air. A quick increase in pressure in the vacuum chamber can break the turbo pumps. Therefore, it is important to keep in mind whether or not there is air in the source, and whether or not the source is completely isolated from the rest of the vacuum chamber.

1. Turn off arc and puller voltages.
2. If the track has been removed, reinstall it before removing the source.
3. Disconnect the water and power from the source.

4. Close the turbo pumping valve.
5. Release the clamp in latch.
6. Slide the source out of the magnet until it reaches the stop latch.
7. Clamp the source into the out position with the clamp out latch.
8. Close the main ball valve Now the source is completely isolated from the rest of the vacuum, and, importantly, the turbo pumps.
9. Open the vent valve to allow air to come into the source.
10. Disconnect the turbo pumping valve from the source.
11. Release the two vacuum lock latches.
12. Slide the vacuum lock away from the magnet and release the source.

A.4.2 Replacing a cathode.

1. Remove the source, if you do not want to break vacuum, be sure to correctly follow the preceding procedure.
2. Unscrew the four screws that hold the anode to the end of the source.
3. Use needle nose pliers to unscrew the cathode from the source.
4. If the cathode can be reused at a different angle, add or remove .005 inch copper washers so that the cathode will be realigned with a clean spot below the hole in the anode. If the cathode cannot be reused, get a new one.
5. Screw the cathode back on as tightly as possible. If the cathode is not rotated to the position you want when it is tight, add or remove washers, do not settle for a loose cathode.
6. The cathode anode gap should be between .5 and 2 mm

A.4.3 Retuning the source without breaking vacuum.

1. Place the source on the track, and latch it in the out position.
2. Slide the vacuum lock against the main ball valve and latch it in place.
3. Attach the turbo pump valve to the source, but DO NOT OPEN IT.
4. There is air in the source, we do not want this air to get into the main vacuum, so we must pump it out. Attach a small pump to the vent valve and pump all the air out of ion source. If you are replacing the lower source, the gas flow should be ON at this point. The flow should be 0.1 cc/min or less.

5. Using one of the thermal couple gauges, wait until the pressure in the source is less than 20 mTorr.
6. Close the vent valve (removing the small pump from the system) and then open the main ball valve (opening the source to the main magnet).
7. Open the turbo pump valve.
8. Slide the source into the in position.
9. Clamp the source in.
10. Connect water and power.
11. You may have to wait 30 minutes or so for the vacuum to recover before running the source.

A.5 Contacts

- For any problems you can contact Ted Forringer.

  TedForringer@letu.edu

  (903) 233-3959 work

  (903) 553-9641 home

- For problems with the beam current monitor and the probe drive motors or controllers, contact Kelly Davidson or John Priller
- For problems with the Sequencer program (or other software) contact Mark Davis.
- For problems with the magnet power supply contact Dan Scott or John Brandon
- For mechanical problems with dee, water cooling etc, contact Gunter Stork.
- For questions about using the vacuum systems, contact Dave Sanderson or Andy Thulin
- For problems with the source (maintenance etc.) contact Emmanuel Blosser at Harper Hospital

  (313) 745-2313 work

  1-888-442-1334 voice pager

Appendix B

Approximating a Maxwell-Boltzmann Distribution of Starting Energies

The fraction of particles (F) whose kinetic energy falls in the range E_1 to E_2 is given by the Maxwell-Boltzmann distribution [21, p 707]:

$$F = A \int_{E_1}^{E_2} E e^{-E/kT} dE \tag{B.1}$$

where A is a normalization constant, k is the Boltzmann constant (8.617×10^{-5} eV/K), and T is the temperature in kelvin. Expressing kinetic energy in units of kT, $\epsilon = E/kT$, the equation can be re-written:

$$F = \int_{\epsilon_1}^{\epsilon_2} \epsilon \, e^{-\epsilon} \, d\epsilon \tag{B.2}$$

which is normalized such that $\int_0^\infty \epsilon \, e^{-\epsilon} \, d\epsilon = 1$. To approximate this distribution with discrete energy levels, each energy level should represent an equal number of particles. Figure B.1 shows the energy density function divided into five equal areas (equal fractions of particles) with the value of ϵ that best represents each area marked with an 'X.'

For the general case, with N energy levels ϵ_n ($n = 1, 2, ...N$):

$$\int_0^{\epsilon_n} \epsilon \, e^{-\epsilon} \, d\epsilon = \frac{2n-1}{2N} \tag{B.3}$$

Integration by parts leads to

$$(\epsilon_n + 1) \, e^{-\epsilon_n} = 1 - \frac{2n-1}{2N} \tag{B.4}$$

which is a transcendental equation that does not have an obvious general solution for ϵ_n, however, solutions for various values of N and n are given in table B.1. For the comparisons between calculated trajectories and experimental data in section 3.3 we use five energy levels to represent the energy distribution.

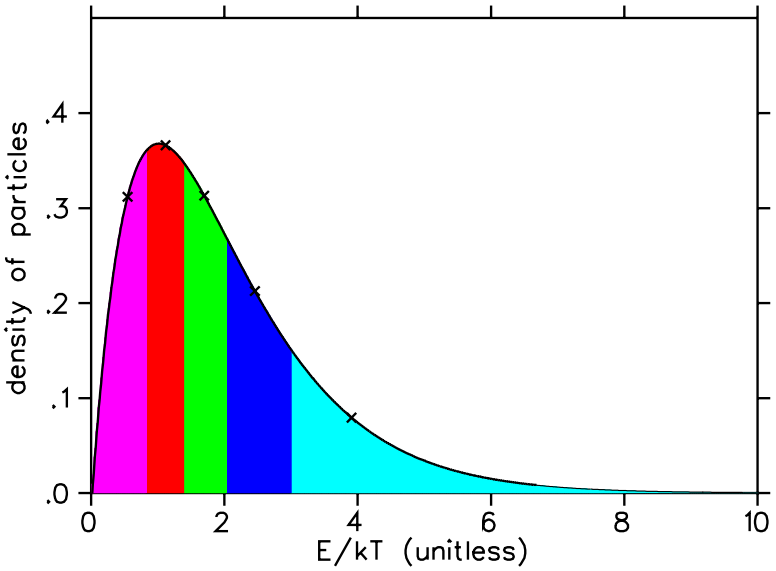

Figure B.1: Maxwell-Boltzmann Distribution of Particle Energies

n =	1	2	3	4	5	6	7
N=3	0.73	1.68	3.24	x	x	x	x
N=4	0.61	1.31	2.12	3.61	x	x	x
N=5	0.53	1.10	1.68	2.44	3.89	x	x
N=6	0.48	0.96	1.42	1.96	2.69	4.12	x
N=7	0.44	0.86	1.25	1.68	2.19	2.90	4.31

Table B.1: Discrete Energies (in units of kT) to Represent a Maxwell-Boltzmann Distribution.

LIST OF REFERENCES

[1] Gammino, S. *et al.*. 'Effects of Frequency and Magnetic Field Scaling on the Superconducting Electron Cyclotron Ion Source at MSU-NSCL' Rev. Sci. Instrum. 67(12) Dec. 1996. p4109

[2] Zavodszky, P *et al.* 'Emittance Studies of the ARTEMIS ERC Ion Source' Proc. of the XVI Int. Conf. on the Applications of Accelerators in Research and Industry Denton, 2000. Conf. Proc. p619.

[3] Jongen, Y. 'The Cyclone 30, a 30 MeV, High Intensity H^- Cyclotron for Radioisotope production.' 7th Conference on Applied Accelerators, St. Petersburg, USSR, 1992.

[4] Bennett, J. R. J. 'Review of PIG Sources for Multiply Charged Heavy Ions.' IEEE Nuc. Sci. NS-19. #2, (1972) p48

[5] Livingston, Robert S. and Royce J. Jones. 'High Intensity Ion Source for Cyclotrons.' Rev. Sci. Inst. 25, 6, (1953)

[6] Mallory, Merrit Lee *Phase Space Density Studies on Cyclotron Ion Sources*, Ph.D. Thesis, Michigan State University, 1966.

[7] Antaya, T. A. *et al.*. 'Operating Experience with an Ion Source in a Superconducting Cyclotron.' IEEE Nuc. Sci. NS-30. #4, (1983) 2716

[8] Blosser, H. G. *et al.*. Compact Superconduction Cyclotron for Neutron Therapy, IEEE Transaction on Nuclear Scienc, NS-32, No. 5 3287 (1985).

[9] Schillo, M. *et al.* Compact Superconducting 250 MeV Proton Cyclotron for the PSI PROSCAN Proton Therapy Project. Cyclotrons and Their Applications 2001 pp 37-39.

[10] `http://p-therapie.web.psi.ch/proscan.html`

[11] Schubert, Jeffery R. *Extending the Feasibility Boundary of the Isochronous Cyclotron*, Ph.D. Thesis, Michigan State University, 1997.

[12] Goldstein, Poole and Safko *Classical Mechanics 3rd ed.* Addison Wesley, San Francisco CA. 2002.

[13] http://www.triumf.ca/compserv/relax3d.html

[14] Lynn, Y. *Ernest Lawrence's Cyclotron: Invention for the Ages.*

[15] Blosser, H. G. *Physics 961 Lecture Notes*, (1971).

[16] Stockli, Martin P. *et al.* 'Accurate Estimation of the RMS Emittance from Single Current Amplifier Data' *Spallation Neutron Source Conf. AP 80*, (2002)

[17] Pozdeyev, Eduard. 'A New Code for Simulation of Space Charge Effects in Isochrounous Cyclotrons', *National Superconducting Cyclotron Laboratory.* 1999.

[18] Edwards, D. A. and M. J. Syphers *An Introduction to the Physics of High Energy Accelerators* John Wiley & Sons, Inc. 1993. pp 78-83

[19] TOSCA, Vector FIelds Inc., England.

[20] Gruber, Peter 'Normalized Emittance in the Case of Large Momentum Spreads' J. Phys. G: Nucl. Part. Phys. 29 (August 2003) 1693-1695.

[21] Young, H. and R. Freedman *University Physics 11th ed.* Addison Wesley, San Fransisco, CA. 2004.

[22] Chen, Francis F. *Plasma Physics and Controlled Fusion, 2nd ed.* Planum Press, New York, NY. 1985.